POLITECNICO DI TORINO
GRENOBLE-INP PHELMA
EPFL

Master's Degree in Nanotechnologies for ICTs

Master's Degree Thesis

Non-volatile reconfigurable integrated photonics enabled by phase change materials

Supervisors

Prof. Niels QUACK

Dr. Hernan FURCI

Prof. Fabrizio GIORGIS

Candidate

Francesco BERTOT

13/09/2021

Summary

Silicon Integrated Photonics is today an effervescent field which, during the past 20 years, has enabled the implementation of increasingly complex on-chip optical circuits. Among the vast range of optical devices recently analyzed, the development of reconfigurable components has attracted larger and larger interest: the possibility to finely tune their properties enables an efficient and fully integrated manipulation of the circuit, providing many different additional features within the same area and computational cost. In particular, in recent years great effort has been concentrated on developing reconfigurable optics able to retain their properties unaltered after the actuation, without the need to maintain it ON. This quality is called non-volatility, fundamental in low-power applications.
One of the most promising methods to obtain non-volatile components is the integration of phase change materials (PCM), semiconductor alloys with extremely different optical properties in crystalline or amorphous solid states. Their state transition can be achieved with nanosecond-duration heat pulses.
In this project, the integration of two commonly employed PCMs, GeTe and $Ge_2Sb_2Te_5$, has been analyzed both from the fabrication and from the design and simulation point of view. First, a fully integrated process based on DUV lithography has been developed, while today most of the studies employ E-beam to pattern these materials. This choice allows a faster processing of the wafer, enabling a large-scale production. After the preliminary characterization of the involved PCMs, smaller loop experiments have been performed on two alternative techniques selected to pattern them, i.e. lift-off and etching, optimizing their process parameters and performing a conclusive comparison.
In parallel, the design of different optical components has been carried out through a combination of Comsol Multiphysics®, for their physical simulation, and MATLAB®, for the successive data analysis, in particular for the geometrical optimization of Si-PCM hybrid adiabatic couplers, and hybrid phase shifters. Finally, both these elements have been employed to generate the layout of different optical devices, respectively a switch matrix and a Mach-Zehnder Interferometer (MZI). The latter will be later included in a dedicated photolithography reticle, used to perform the complete process flow previously created.

Acknowledgements

I would like to thank, above all, my supervisor, Hernan Furci, for having chosen me for the project, for having believed in me during the semester and for all the support provided, together with Professor Niels Quack, for having welcomed me in its research group and for the excellent suggestions given during the period.
In the same way, I would like to thank Professor Fabrizio Giorgis, for the constant feedback provided during the semester.
Then, a special thanks goes to the other members of the Q-LAB, who helped me with their experience, my colleagues, who accompanied me in this exciting endeavour, and my family and friends, who supported me throughout this journey.

Table of Contents

List of Tables

List of Figures

Acronyms

AFM
Atomic Force Microscopy

ALD
Atomic Layer Deposition

BARC
Back Anti-Reflecting Coating

CD
Critical Dimension

CMI
Center of MicroNanoTechnology, at EPFL

CMOS
Complementary Metal-Oxide Semiconductor

CVD
Chemical Vapor Deposition

DC
Directional Coupler

DC(2)
Direct Current

DL
Device Layer

DUV

Deep Ultra Violet

EBL

Electron Beam Lithography

EM

Electromagnetic

FPGAs

Field-Programmable Gate Arrays

FEM

Finite Element Method

FOM

Figure Of Merit

FTE

Full Thickness Etch

GND

Ground, refers to a low voltage

GST

$Ge_2Sb_2Te_5$, one of the analyzed PCMs

IBE

Ion Beam Etching

IC

Integrated Circuits

ICP

Inductively Coupled Plasma

IL

Insertion Losses

IR

Infrared

IT

Information Technology

MEMS

Micro-Electro-Mechanical Systems

MMI

Multi-Mode Interferometer

MOSFET

Metal-Oxide Semiconductor Field Effect Transistor

MZI

Mach Zehnder Interferometers

O-PCM

Optical Phase Change Materials

PCM

Phase Change Materials

PIC

Photonics Integrated Circuits

PLD

Pulsed Laser Deposition

PR

Photoresist

PS

Phase Shift, Phase Shifter

PTE

Partial Thickness Etch

CVD

Physical Vapor Deposition

RF

Radio-Frequency

SEM

Scanning Electron Microscopy

SOI

Silicon-On-Insulator

TE

Transverse Electric

TM

Transverse Magnetic

WG

Waveguide

Chapter 1

Introduction

The continuously-increasing request for innovation and performances improvements in telecommunication networks is nowadays leading to a change in perspectives with respect to the past few decades. Indeed, during the last 60 years, the field of information technology (IT) mainly relied on the electronic industry, whose advancement towards better efficiency and the production of more and more performing devices have followed the so-called - and well known - Moore's Law [1]. It is practically a model that, since its formulation in the sixties, has correctly predicted a doubling of performances and functionalities for digital electronics with the same cost, chip area and power consumption every 2 years of research and development. However, this trend is coming to an end.
The most critical problem is constituted by the fact that the continuous research for higher data processing rate, lower power consumption and greater functionality has pushed the features scaling in CMOS technology down to dimensions in the order of few nanometers, therefore, close to the physical atomic limit [2]. From the nineties, different issues have arisen, such as the growing number of interconnections, with a consequent greater presence of parasitic power consumption, or the increase of leakages even for transistors in their OFF state. In consequence, alternative solutions have been searched, starting from the employment of different materials both for the interconnections, like copper instead of aluminum [3], and as a gate, as high-k dielectrics or polysilicon [4].
However, during the past twenty years, the most promising advancements have been made thanks to the integration in the same chip of different technologies developed in parallel to the CMOS one, leading to a new so-called "more than Moore" trend. Some examples are the combination of both Si and III-V semiconductors, or the integration of MEMS (Micro-Electro-Mechanical Systems), components that can be fabricated together with the same processes, and provide many additional functionalities like actuation, sensing and signal-processing [5].

Among this large amount of new technological boosts, one of the major contribution to the current request for larger and larger data transmission, with relatively low losses and wide bandwidth, is the introduction of optical interconnections, which today are replacing the classical electronic ones. This process is justified by many reasons [6]: it is proven that signals in optical fibers propagate much faster, since in electrical lines limitations are imposed by the overall resistance and capacitance of the circuit, but moreover, the higher frequency of light with respect to electrons (up to 500 THz versus 10 MHz - 10 GHz respectively) and the higher photons energy provide different advantages, such as the absence of losses, distortion and frequency dependence of the signal at high frequency. During the past few years, all these aspects have gradually led to the development of a whole new set of optical components that, today, are attempting to replace the electrical ones even in integrated circuits (IC).
In particular, as presented in [7], after years of accurate inspection of the electro-optical properties of silicon, it became the leading material for the production of optical waveguides to confine and guide light signals, filters and modulators to manipulate them, couplers, lasers, detectors, and all the required optical components today employed in the so-called Photonic Integrated Circuits (PIC). All these innovations and improvements have, therefore, outlined that silicon photonics can provide numerous benefits both in long- and short-range information transfer, from optical transmission through distances in the order of tens of kilometers, to inter- and intrachip communication. The latter, in particular, has been favoured by already mature fabrication processes, mostly readapted from the ones employed for years for the creation of microelectronic components.
However, silicon alone still presents optical properties that can vary in a modest range, a factor that obviously limits the capabilities of the circuit as, for example, doesn't allow the fabrication of all-Si optical switches. As a consequence, larger and larger interest is being invested in hybrid devices, which combine the good structural quality of Si and its well-known fabrication methods to more tunable optical properties provided by different materials, like Germanium [8], electro-optic polymers [9], two-dimensional materials [10] and optical phase change materials (O-PCM) [11]. In particular, the latter are today object of a careful analysis, since, due to their large change in optical properties, they present a promising chance to realize devices with a relatively small footprint and large broadband, together with a large compatibility with the standard silicon fabrication processes.

The purpose of this report is to present the obtained results of the investigation of a new processing flow to integrate the PCMs, different with respect to what is present today in literature, and an innovative mechanism to actuate them, with the idea to obtain an efficient switch between their states and, therefore, an efficient way to process signals in electro-optic hybrid chips.

1.1 PCM in silicon integrated photonics

During the last few years, many important progresses have been made in the field of PIC, given that Si photonics have shown its potentiality to obtain a high computational speed with a relatively low power consumption and reduced footprint. However, despite the great effort already made, integrated photonics still remains a domain in large expansion, since, if compared to the advancement of the electronic market, its progression is 20 - 30 years behind [12]. Therefore, new applications and possibilities are constantly emerging, and the excitement over every new step forward is pushing this field towards an expected larger and larger success.
One of the aspects that today is drawing greater interest is, in particular, the possibility to create reconfigurable optical circuits, whose properties can be finely tuned to achieve larger amount of data processing within the same dimensions of the chip: circuits, in practice, comparable to the usual field-programmable gate arrays (FPGAs) employed in electronics, but which rely on changes in the optical properties of its components, i.e. their refractive index n and extinction coefficient k. In consequence, reconfigurable switches, phase shifters, interferometers and ring resonators have been produced and optimized with the idea of realizing larger optical networks for signal transmission or logic gates for signal processing.

Currently used reconfigurable components mostly rely on two principle mechanisms: free-carrier dispersion or thermo-optic effects [13]. In both cases, the idea is to obtain the optical switch by applying an electric field through the Si structure, causing, respectively, a change in the free carrier distribution of the semiconductor and the material heating. However, these approaches present different issues: on one side, the effect on n is usually quite weak, with typical changes of $\Delta n < 0.01$, and this results in larger devices and higher power consumption to obtain a sufficient modulation; on the other, these variations are volatile and, therefore, a state change can be only maintained as long as the power supply is active.
All these aspects have led the research to more efficient alternatives, and one of the most promising one is the integration of PCMs in the same devices previously produced in silicon alone. Indeed, they present unique characteristics [14]: their atomic structure comes in two alternative configurations, amorphous and crystalline, which have quite different optical properties (with variation of $\Delta n > 1$) and electrical conductivity, and which, what matters most, are non-volatile even for periods up to years. So, no additional power consumption is required to maintain a certain state, while the state transition is fast and reversible, achieved by heating the material with nanosecond energy pulses.
As a consequence of all these advantages, integration of PCMs in reconfigurable devices can potentially lead to limited footprint, low power consumption, non-volatility and fast transition time, with different available actuation mechanisms.

Unfortunately, on the other side, a great disadvantage is constituted by the quite elevated absorptive loss associated to the high extinction coefficient present in almost all PCMs. Indeed, values of the insertion losses (IL) in typical devices of this kind can also reach values of some dB, and therefore limit their performance in terms of signal transmission. In consequence, the main idea in every design is to maintain the PCM dimensions as small as possible, in order to obtain a significant optical modulation while keeping the total losses low.

This design choice has, obviously, important consequences on the practical fabrication of this type of devices. Indeed, the need for small features, usually in the order of few hundreds of nanometers, greatly restricts the number of available techniques. This is the main reason why, in most of the cases, the PCM patterning has been performed through electron beam lithography (EBL), a technique that employs a collimated electronic beam to obtain even features in the order of tens of nanometers. Two examples of already fabricated devices, respectively a directional coupler (DC) [15] and a multi-mode interferometer (MMI) [16], both relevant for the scope of this report, are presented in Fig. 1.1 and 1.2.

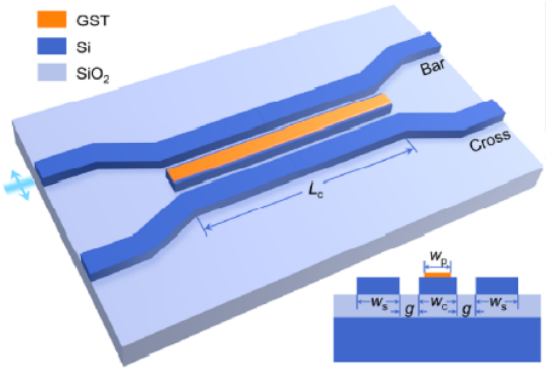

Figure 1.1: Design schematic of a 2 x 2 DC switch employing a PCM layer in the central portion, taken from [15].

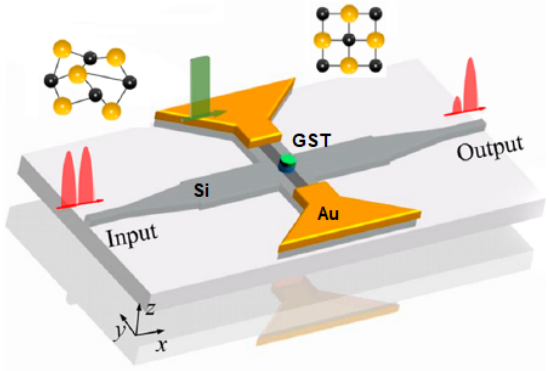

Figure 1.2: Schematic of a PCM-gated MMI with lateral metallic contacts, taken and readapted from [16].

In particular, in Fig. 1.1 it can be noticed that the coupler is built using three strip silicon waveguides (WG), with a PCM layer (in this case $Ge_2Sb_2Te_5$, also referred to as GST-225 or simply GST) deposited on top of the central one. The device is designed to obtain a good coupling condition when the PCM is in the amorphous state, with signal crossing the structure and exiting through the Cross port, while it remains in the input WG in the case of a crystalline form, proceeding through the Bar port.
On the other hand, Fig. 1.2 presents a silicon MMI with a circular portion of GST

on top of the central region, and lateral gold electrodes, used for actuation the PCM state transition. When the latter is amorphous, the signal flows through the structure, while it is highly attenuated when a crystalline form is present, thanks to its quite high extinction coefficient. In this way, an ON/OFF switch can be obtained without moving portions, and a consequent highly compact structure.
Both the analyzed devices are designed to operate at a target wavelength of 1550 nm, one of the most employed in today's telecommunication applications.

One last important consideration concerns the actuation mechanisms currently used to change the PCM state. The amorphous structure is obtained by rapidly heating the material above its melting point, which is around 600 °C [17], while the crystallization process is performed by heating it in a slower way only above its crystallization temperature, which is between 100 °C and 150 °C. Although many techniques can be used to heat a material, the need for highly localized and controlled heating greatly reduces the available options, with the consequence that today only optical or electrical actuation is performed: in the first case, an external laser is focused onto the target portion of the PCM [15, 18], while in the second one the PCM is heated either by integrated micro-heaters [19], or by Joule effect, thanks to current flowing directly through the silicon structure [16].
The first solution surely has the advantage of an easier implementation, since no additional portion, dedicated to PCM actuation, needs to be integrated in the optical circuit, but this technique is not efficiently applicable on different components of the same chip. Moreover, the alignment of the external source becomes critical, with high risks of a non-uniform exposure of the whole target portion of PCM. On the other hand, the electrical actuation requires a more complex structure, especially in the case of micro-heaters, since the integration of a secondary circuit is surely needed. However, a careful design could enable a much more efficient actuation mechanism even at large scale, with the possibility to address many devices at once. This last option has become, therefore, the most promising one for the implementation of fully integrated circuits.

1.2 Purpose of the project

The aim of the project presented in this report is to study the integration of two different PCMs, GST and GeTe, in silicon PIC commonly employed in various applications, analyzing the possibility to create fully-integrated circuits in which the actuation of single elements can be rapidly and precisely accessed by means of electric contacts. In particular, the fundamental elements that characterize this work, and distinguish it from what is today present in literature, concern the type of analyzed devices, like optical phase shifters and switches, in combination with

the actuation mechanism, which will exploit Joule heating through the use of rib waveguides and fully-integrated electronic circuits, and the fabrication technique, which will, in principle, allow a large-scale production thanks to a faster process with respect to the currently employed methods, while maintaining the features dimensions small enough to guarantee miniaturization and scalability.

During the past few years, many different studies have been performed on reconfigurable optical components, but only few of them have explored the possibility to integrate both a PCM layer and an electric circuit to efficiently perform the actuation. Indeed, some of the most relevant examples of these kind of devices have been produced using strip waveguides, both in the case of optical phase shifters [20], and of switch matrices [21], respectively actuated by means of either optical lasers from the external or electric pulses through additional integrated conducting layers. The main idea to overcome these issues and obtain a more compact solution is, instead, the use of rib waveguides, in which the PCM is deposited on top of the central core, while the electrical contacts are obtained in the lateral wings: in this way, the current would flow perpendicularly to the WG and the PCM layer, heating the structure at a temperature high enough to obtain the phase transition, but much lower than the melting point of silicon (above 1400°C), so that the WG properties are not altered.

Another important aspect concerns fabrication. Until now, many studies have been carried out patterning the involved PCM through EBL, a technique that allows to obtain small features with a high precision, but requires additional manual work from the operator, and can process only one wafer (or even only few chips) at a time. Therefore, the quality of the produced structures can be really high, but the process is more complex and not practical for a large-scale production. These are the main reasons why the idea followed in this project is to use, instead of EBL, deep ultra-violet (DUV) lithography, a technique that employs a laser source at small wavelength instead of an electron beam: the resolution is limited to around 150 nm, but the exposure is performed in a so-called "step and repeat" process which allows a much faster wafer processing, up to more than 100 wafers per hour. In consequence, although the design of the devices is limited by this fabrication choice, since the resolution is limited to around 150 nm, the treatment of a single chip is rapid, and the process can be in principle extended to larger fab productions. Moreover, this technique is today highly automatized, so that the risk of human errors is greatly reduced.

In conclusion, the purpose of the project is to analyze the integration of PCMs in silicon PICs, designing the optimal configurations for the devices in exam, while implementing an efficient fabrication process applicable in large-scale productions.

1.3 Thesis Outline

This dissertation is organized following the fundamental steps performed during the semester for the analysis of the integration of PCMs in newly implemented fabrication process flows, and for the design and simulation of optical components of PIC, a procedure finalised by the creation of multiple mask layouts for the future production of complete devices.
The content of the following chapters is now outlined, together with the main flow linking them.

- In **Chapter 2** a theoretical background provides an overview of the topics treated in this project. In particular, the most relevant optical components in PIC, with their main features and applications, are presented, together with the description of the structure and properties of the employed PCMs.
- **Chapter 3** is dedicated to the results of all the tests performed on PCMs from the characterization and fabrication point of view. All the work presented in this section has been completed within the cleanroom environment of the Center of MicroNanoTechnology (CMI) at EPFL. First, the properties of these materials and of the thin films produced through their deposition have been analyzed. A fabrication process flow for the implementation of complete optical devices has been then prepared, and its most critical steps concerning the PCMs patterning have been tested to extract the optimal processing parameters.
- The procedure for the design and simulation of different optical components is presented in **Chapter 4**. Following the specifications and limitations imposed by the selected fabrication techniques, this analysis has been performed through a combination of Comsol Multiphysics®, for the optical simulation, and MATLAB®, employed the successive optimization of the involved geometrical parameters.
- In **Chapter 5** a series of proposed layouts of complete optical devices, obtained starting from the geometries designed in the previous chapter, are outlined. These structures will be later employed in the physical fabrication of the analyzed components. The layouts has been performed combining MATLAB, for the generation of the main geometries, and L-Edit®, used to finalise the procedure by combining those geometries in complete optical structures.
- The summary of the completed work is provided in **Chapter 6**, together with some considerations about the future continuance of the project.

Chapter 2

Overview of PICs and PCM

2.1 Silicon and silicon oxide as optical materials

As presented in Chapter 1, silicon photonics is nowadays an effervescent field in large expansion, with many promising results obtained during the past few decades, a lot of different applications already explored, and various possible future improvements. In addition to all the details previously discussed, it must be observed that this important outcome is founded on a fundamental key pillar, silicon itself, and its excellent properties both from the physical and structural point of view, which allowed great improvements also concerning the fabrication processes.
Indeed, besides being the second most abundant element on earth (after oxygen), silicon is a semiconductor which can be easily doped to manipulate its electrical properties, with a simple cubic crystal structure, a high melting point (above 1400 °C) and a large thermal conductivity. These are all characteristics that during the past 50 years have constituted the starting point for the development of the semiconductor industry, especially the complementary metal-oxide semiconductor (CMOS) one, in which silicon can be employed both as a substrate, for wafers with potentially no defects and a high purity, and to create active portions of the electronic circuits. The maturity of its processing techniques allows an accurate manipulation of its structure, for a low-cost, large-volume, high-precision fabrication which enables the miniaturization and integration of many different devices.
Today, in addition, the optical properties of silicon are well known: it has a high refractive index of around 3.476 at a wavelength of 1550 nm, commonly used for telecommunications, and it is transparent to radiations in the infrared (IR) range above 1100 nm [22]. In this way, its absorption is negligible for the target wavelength and, therefore, very low losses are caused by silicon itself in an ideally fabricated structure. Indeed, as shown in Fig. 2.1, for wavelength around 1550 nm they are as low as 0.2 dB/km.

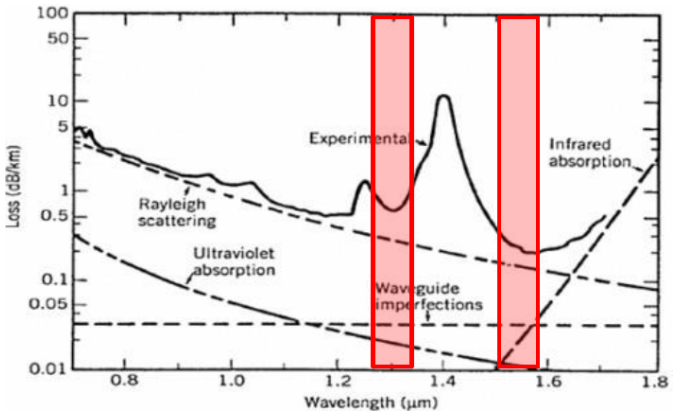

Figure 2.1: Theoretical and experimental dependence of losses in silicon on the operating wavelength. In red, the Original and Conventional Bands used for telecommunications, respectively at 1260-1360 nm and 1530-1565 nm, from [23]

Another important factor that represents an advantage for silicon with respect to other semiconductors, as Germanium, is the possibility to obtain a high-quality oxide, SiO_2, which is totally compatible with Si and, therefore, no particular treatment is needed to combine them in the same structure. Silicon oxide, or silica, is an insulator whose optical transparency in the telecommunication range and relatively low refractive index of around 1.45 at 1550 nm - a value that, moreover, can be tuned by doping the material - have made it the perfect candidate to enhance the optical properties of Si, to obtain a wide range of photonic components thanks to their high refractive index contrast.

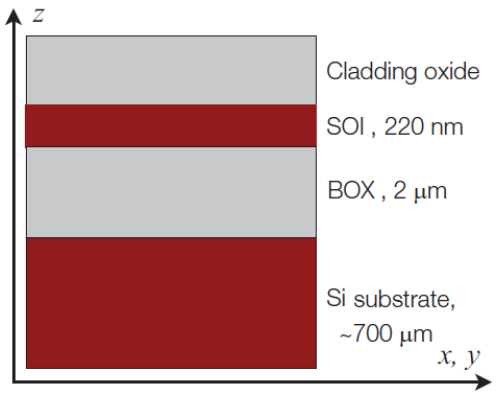

Figure 2.2: Schematic of the structure of an SOI wafer, readapted from [24].

As a consequence, today the most used type of wafer for Silicon Photonics presents a so-called silicon-on-insulator (SOI) structure, as shown in Fig. 2.2. As seen in the picture, this kind of structure is composed by a silicon substrate, usually with a thickness of around 700 μm, covered by a 2 μm thick buried oxide (BOX) made of silica, whose function is to isolate the top Si portion of 220 nm from the bulk. A final layer of SiO_2 is deposited on top to passivate the structure. The optical devices are produced in the SOI layer, enabling a high light confinement in this portion.

2.2 Silicon Photonics devices

The fundamental building blocks at the basis of conventional PICs can be generally classified depending on their working principle, namely their active or passive effect on the signal which is propagating inside the circuit. In particular, active components rely on external sources of energy (mainly electrical, photonic or thermal) for their operation and are used to either generate light (as in the case of lasers), manipulate it during its propagation through the circuit (for modulators or switches), or detect it at the end of the optical path (as for the so-called photodetectors). On the other hand, passive elements are those that manipulate light merely thanks on their structure and optical properties, as it is, for example, in the case of waveguides, used to confine and transmit the signal, bends or directional couplers, to deviate its path, interferometers to collect different signals, and so on. In more elaborate PICs, many of these elements are usually combined together, obtaining a more complex manipulation of the propagating light.

2.2.1 Waveguides

Waveguides are one of the most important building block of many PICs, as they allow to confine light and to direct it across other components in the circuit. The fundamental principle on which they rely is basically a refractive index contrast between the portion in which light is actually confined, called *core*, and its surroundings, called *cladding*. As a consequence, the field is confined inside the waveguide along the two directions perpendicular to the one in which it is elongated, along which, on the contrary, it propagates without undergoing modifications. Therefore, considering a WG disposed in the z direction, the dependence of the electric field **E** on z is simply a phase delay, so that it can be expressed in phasor form as

$$\mathbf{E}(x, y, z) = \mathbf{E}(x, y) \cdot e^{-j\beta z} \tag{2.1}$$

in which β is the propagation constant of the field along z.
In order now to understand which is the dependence of the field on x and y, the dimensions in which it is confined, an accurate demonstration could prove that, starting from Maxwell's equations, the wave equation obtained under the assumption of a non-constant refractive index (as in this case of a waveguide) can be expressed as

$$\nabla^2_{x,y}\mathbf{E} = (\beta^2 - k^2 n^2(x, y))\mathbf{E} \tag{2.2}$$

in which $\nabla^2_{x,y}$ is the Laplacian along the section of the waveguide, $n(x, y)$ is the refractive index (invariant along the propagation direction), and $k = \frac{\omega}{c} = \frac{2\pi}{\lambda}$ is the wavevector, with c = light speed and λ = wavelength. A totally equivalent

equation can be also derived for the magnetic field.
The obtained relation is, for all intents, in the same form of an eigenvalue problem. Its discretized solutions, namely the expression of $\mathbf{E}(x, y)$, are called *modes* of the waveguide, while the associated eigenvalues correspond to the propagation constant with which they propagate along the structure. This constant is perfectly real if the mode is guided without losses, while its imaginary part, if present, allows to estimate the mode's attenuation, generally due to materials absorption if they have a complex refractive index. Any field propagating in the waveguide can be expanded as a series of its modes and, in particular, depending on the initial conditions of the problem, only some of them are excited, and propagate with their propagation constant. Usually, the excitation of a single mode is targeted, designing the structure to have a real constant only for the so-called fundamental mode. This is called single-mode operation
The eigenvalue problem, that at this point remains multidimensional, can be solved assuming that the field distribution along one of the confinement directions is independent from the distribution along the other. In this way, these vectorial equations can be divided in two subsets of relations called transverse electric (TE) and transverse magnetic (TM), in which, respectively, the electric and magnetic field present a null component along the waveguide axis (along which propagate trough a phase delay), laying on its perpendicular section.

Main typologies

In current applications, these components are of two main types: *strip* and *rib* waveguides, which present different geometric structures, as shown in Fig. 2.3. As mentioned in 2.1, the most used platform is the SOI, since the high refractive index contrast between Si and SiO_2 enables a good light confinement in the device layer.

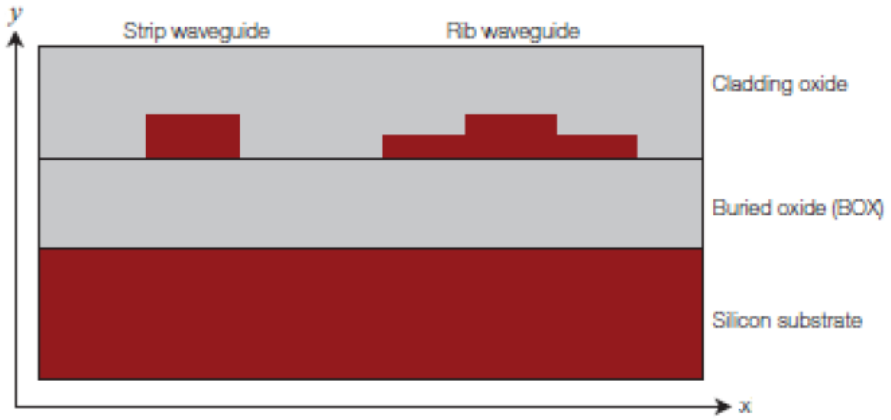

Figure 2.3: Cross-section view of different types of waveguides on SOI, from [24].

The strip waveguide has the advantage of a simpler geometry, which allows an easier fabrication with a single etching step to pattern it. Moreover, a curved waveguide of this type could have a tight bend radius, down to few microns, since losses due to the bend remain limited. While its height is fixed to 220 nm as that of the device layer in the SOI wafer, the width can vary depending on the requirement of the circuit - typical values for single-mode operation are around 500 nm. On the other hand, the rib waveguide presents a more complex geometry, with a central core and lateral wings: it requires an additional control over the fabrication process, and eventual bend radii are wider, typically of few tens of microns, but the lateral portions allow for doping and electrical contacts without requiring extra integrated structures. In addition, the thickness ratio between core and wings represents another degree of freedom, for a more flexible design: the most used combinations are 150 - 160 nm for the wings, and 70 - 60 nm for the core respectively. An example of the fundamental TE mode (the first excited mode) propagating in both types of waveguides is shown in Fig. 2.4.

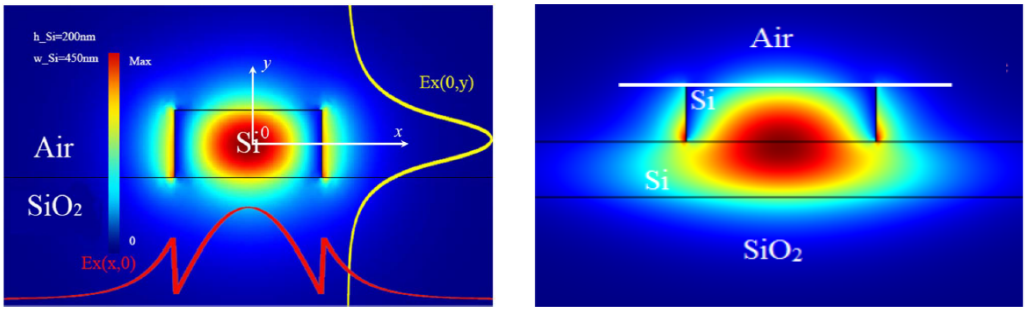

(a) *TE mode in strip WG* **(b)** *TE mode in rib WG*

Figure 2.4: TE fundamental mode in strip (left, from [25]) and rib (right, from [26]) Si WGs with SiO_2 and air cladding, obtained at $\lambda = 1550$ nm.

Losses

Another important parameter to be considered when designing a waveguide is the total loss caused by the structure. As seen in 2.1, in the telecommunication range losses caused by Si can be neglected, especially when the dimensions are those of PICs and, therefore, an integrated silicon waveguide should be ideally lossless. However, in real devices the fabrication outcome is never perfect, and therefore some other sources of losses are present [24]:

- Leakages to the substrate or to metallic interconnections: this effect is due to possible couplings of the modes exponential tails in the cladding with elements

too close to the device layer, causing the loss of a portion of the conduced power. For example, in a conventional strip WG, losses are estimated as around 1.8 dB/cm for a metal 600 nm far from the waveguide. This issue can be mitigated by correctly isolating the waveguide, using a thick BOX of at least 2 μm, and avoiding interconnects proximity.

- Surface-state absorption: on the surface of non-correctly passivated WGs some unwanted energy states may absorb portions of the guided power. Obviously, a solution to this problem is a correct passivation of the device.

- Sidewalls and top surface roughness: while modes are supposed to propagate along the waveguide with perfect reflections on its surfaces, in real devices the latter are never perfectly smooth, and the resulting roughness produces scattering and phase perturbations, for losses up to 2-3 dB/cm. Usually, this effect can be reduced on one side performing a chemical-mechanical polishing (CMP) of the top surface, on the other trying to smooth the sidewalls, with accurate post-etch treatments, or using wider waveguides. This last option has the benefit to reduce the overall effect of this lateral scattering, since the field has more margin to propagate, but the confinement is reduced, and additional modes can be excited.

In the choice between strip or rib waveguides, losses also play an important role. Indeed, despite the precautions just mentioned above, the main contribution to power dispersion remains the one caused by sidewalls roughness. In consequence, the modes distribution in the section of the waveguide becomes the most critical parameter. As shown in Fig. 2.4 the discontinuity of refractive index at the edges of the waveguide causes an increase of the value of the field right outside it, compensating for the medium change. It can be noticed that the portion of the field outside the core is much reduced in the case of a rib waveguide. Indeed, its sidewalls, on which the discontinuity is present, are only 60-70 nm thick, while for the strip structure the whole lateral edge of 220 nm contributes to propagation. In consequence, losses are higher for strip waveguides, with typical values greater that 2.4 dB/cm, while they are usually less than 0.3 dB/cm in rib WG.
For the purpose of this project, also because considerable losses are already introduced in the system by PCMs, rib waveguides have been employed, in order to reduce as much as possible the other sources of power dissipation.

2.2.2 Directional Couplers

The directional coupler (DC) is another fundamental passive component in modern PICs, used to manipulate the propagating light by either splitting, recombining or redirect it to different portions of the circuit. The basic structure consists

of two parallel waveguides separated only by a narrow gap. In such a situation, the waveguides cannot be analyzed singularly, since the eigenmodes of this more complex geometry cannot be in general associated to only one of them. These are the so-called *supermodes*.
The modes of the single waveguides must be, in consequence, expanded in the supermode bases: if we call $\varphi_1(x,y)$ and $\varphi_2(x,y)$ the fundamental modes of the two branches alone, as a rough approximation the two lowest order supermodes of the coupler, the symmetric and antisymmetric ones, can be respectively written as $\Psi_s(x,y) = a(\varphi_1 + \varphi_2)$ and $\Psi_a(x,y) = b(\varphi_1 - \varphi_2)$ (with a and b normalizing factors). The field distribution of these modes is shown in Fig. 2.5.

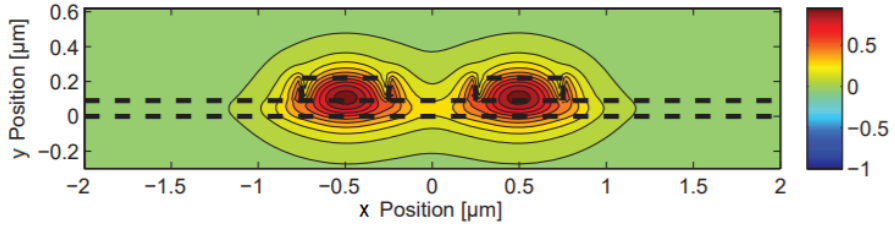

(a) *Real(E_x) for the symmetric supermode.*

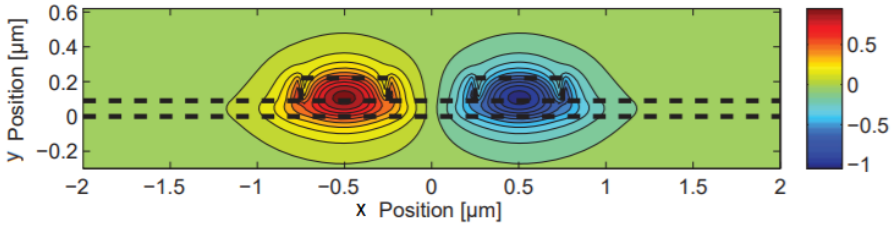

(b) *Real(E_x) for the antisymmetric supermode.*

Figure 2.5: Real part of the E_x component of the electric field for symmetric and antisymmetric supermodes of a directional coupler made of rib waveguides [27].

Since these modes are different, after their excitation they propagate with different speeds along the structure since their propagation constant is different. The result is an interference pattern between them, with a constructive or destructive effect depending on the relative phase shift. Indeed, from the expressions of the modes presented above, it can be demonstrated that, for an input power P_0, the values of the power in each of the two waveguides is obtained as

$$P_1 = P_0 \cos^2\left(\frac{\beta_s - \beta_a}{2} \cdot L\right) \quad \text{and} \quad P_2 = P_0 \sin^2\left(\frac{\beta_s - \beta_a}{2} \cdot L\right) \tag{2.3}$$

where $\beta_s = \frac{2\pi \cdot n_s}{\lambda_0}$ and $\beta_a = \frac{2\pi \cdot n_a}{\lambda}$ are the propagation constants of the symmetric and antisymmetric supermodes respectively, with n_s and n_a the associated effective

mode indices, while L is the position along the coupler. By adding the two equations, it can be easily seen that $P_1 + P_2 = P_0$ for $\forall L$ and, therefore, the device itself is lossless. As a consequence, while modes propagate along z, the total power transits from one waveguide to the other in a periodic way, without being dissipated. From Eq. 2.3, we can obtain the expression of the so-called coupling length, the required length for the total power to completely pass from one waveguide to the other: by imposing $P_1 = 0$ and $P_2 = P_0$, the coupling length is extracted as

$$\frac{\beta_s - \beta_a}{2} \cdot L_c = \frac{\pi}{2} \quad \Longrightarrow \quad L_c = \frac{\pi}{\beta_s - \beta_a} = \frac{\lambda}{2(n_s - n_a)} \tag{2.4}$$

This, besides the geometry of the single waveguides, is the most important parameter when performing the design of a directional coupler. Indeed, for a total power transfer its length is chosen exactly equal to L_c, so that the signal coming from one waveguide (the input port) is totally transferred to the second one before being deviated towards another portion of the circuit. Fig. 2.6 shows the schematic of an example of this kind of structure.

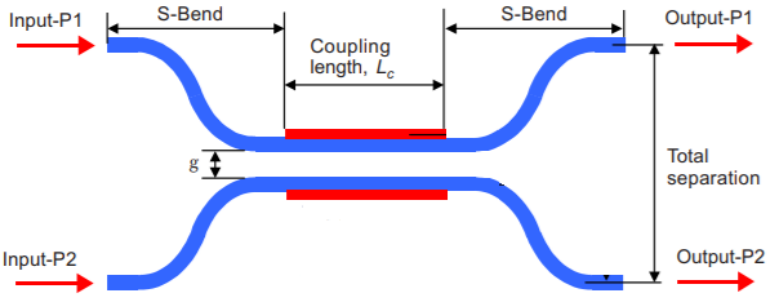

Figure 2.6: Schematic top view of a directional coupler, readapted from [28].

2.2.3 Adiabatic Couplers

While conventional directional couplers are a quite simple - from the working principle and fabrication point of view, since they only consist of parallel waveguides with fixed dimensions - and compact solution to redirect light inside a PIC, the main drawback they usually present is a limited bandwidth. Indeed, as shown in Fig. 2.7, the indices of the supermodes in this kind of component have a quite strong dependence on the operating wavelength and, consequently, the coupling length deviates with respect to the optimal one for which the device has been designed. The result is a non perfect transition of the signal from one waveguide to the other, with the consequent loss of a portion of the power.

One of the most common solutions to overcome this issue is the use of asymmetrical structures, since it has been proven, both theoretically and experimentally

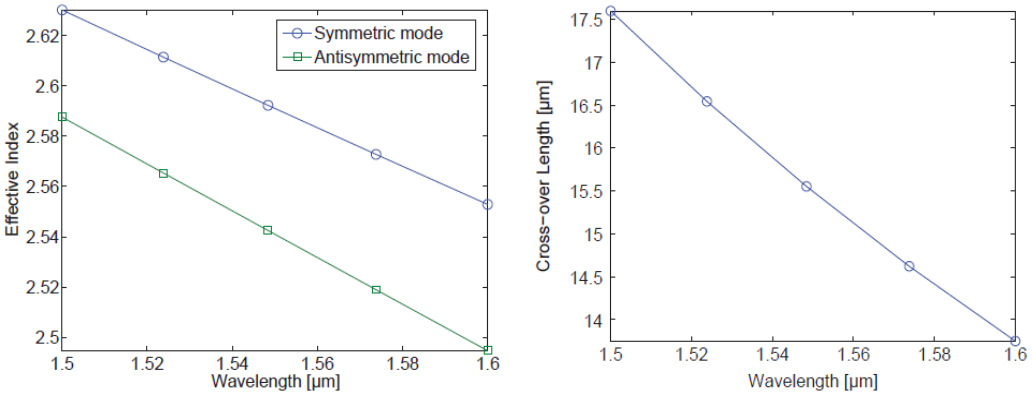

(a) *Effective index for the supermodes.* **(b)** *Coupling (Cross-over) length.*

Figure 2.7: Effective mode index and coupling length dependence on the wavelength for a directional coupler made of rib waveguides [27].

[29], that the wavelength response of these kind of geometries is much more stable. The main idea is to obtain a gradual power transition from the input waveguide, whose width is fixed, to the output one, that instead presents a tapered structure. In this way, the excitation of a single input mode causes the gradual (adiabatic) excitation of only one of the supermodes of the coupler. Today, many adiabatic couplers have been employed to obtain a 3 dB split of the incoming power, with particular geometries that allow this division by matching the waveguides at the end of the device [30]. For the purpose of this project, the aim is different: the coupling happens in the middle of the structure, while the matching condition between the waveguides is broken in the final portion by increasing even more the width of the output waveguide, with the consequence that, in principle, the transferred power cannot return back in the input one. Thanks to this gradual transition, this kind of device should present a reduced sensitivity over variation of wavelength, with a resulting larger bandwidth with respect to a symmetric coupler. A schematic of the geometry of the system is shown in Fig. 2.8.

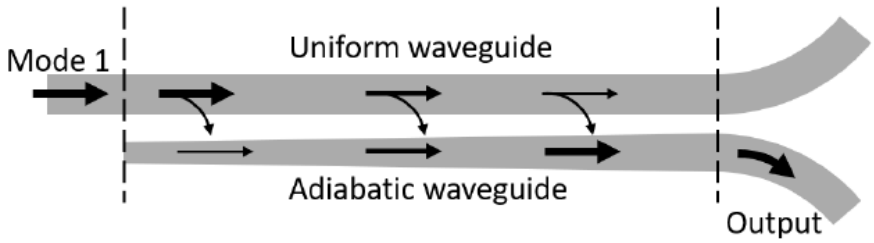

Figure 2.8: Schematic top view of an adiabatic coupler, readapted from [30].

2.2.4 Mach-Zehnder Interferometers and Phase Shifters

Another important building block of silicon PICs is the Mach-Zehnder interferometer, whose most simple structure is shown in Fig. 2.9.

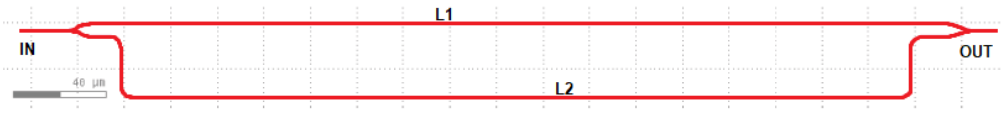

Figure 2.9: Schematic layout of a MZI, readapted from [27].

As presented in the picture, this component consists of an initial power splitter (a so-called Y-branch) that divides the signal in two equal components, which propagates along different parallel waveguides, L1 and L2, and then recombine thanks to a power combiner (a reversed Y-branch). At the end of the structure these two components are usually out of phase and, therefore, the output presents various interference patterns depending on the phase difference. It can be demonstrated (see [27], pp. 113-114) that the intensity after the recombination is computed as

$$I_o = \frac{I_i}{2}[1 + \cos(\beta_1 L_1 - \beta_2 L_2)] \tag{2.5}$$

where I_i is the intensity at the input of the device and β_1 and β_2 are the propagation constants in the two branches respectively. It is a sinusoidal function which, besides the length of the paths, depends on the wavelength and on the effective index of the waveguides (both hidden inside β), so a modulation of the output signal can be obtained by acting on one of these parameters.
There are several mechanisms on which the MZI can rely to produce the phase delay and, indeed, the device can be designed to be either a passive or active component. In the first case, the structure itself is optimized to have different parameters on the two branches, as a variation in length or in the effective index, obtained either using different materials, or modifying the width of one of the waveguides. On the other side, an equivalent effect is produced maintaining the same geometry on both branches and exploiting an external actuation on one of them. The latter can directly act on the properties of silicon, through thermo-optic or plasma dispersion effect (see 2.1), or can be provided by additionally integrated active components like ring [31], electro-absorption [32] or plasmonic [33] modulators.
All the techniques and devices employed to obtain such an actuation can be classified as phase shifters, since they are employed to modify the phase of the signal by changing the effective index of the waveguide in which it propagates. The main challenge in the design of this kind of structures is to provide an efficient manipulation of the signal, maintaining a small footprint and low losses and power consumption, a requirement that still represents a great issue for their proper

integration. One of the scopes of this project is to present an alternative solution to this challenge, with the design of a phase shifter that relies on the properties of PCMs, which, despite quite significant losses, can allow non-volatility, so reduced power consumption, and a high miniaturization thanks to a compact geometry.

2.2.5 Optical switches

Optical switches are among the most useful devices in modern silicon photonics, as their integration offers the possibility to perform multiple operations in the circuit while maintaining a limited footprint. They are, indeed, active components which exploit the properties of optical modulators to deviate the path of the signal depending on an external actuation, a contribution that nowadays is essential for large-scale interconnections for computer and data centers communications [34]. Today, a wide range of optical switches relying on different working principles can be found for various applications. Some of the most investigated solutions are shown in Fig. 2.10.

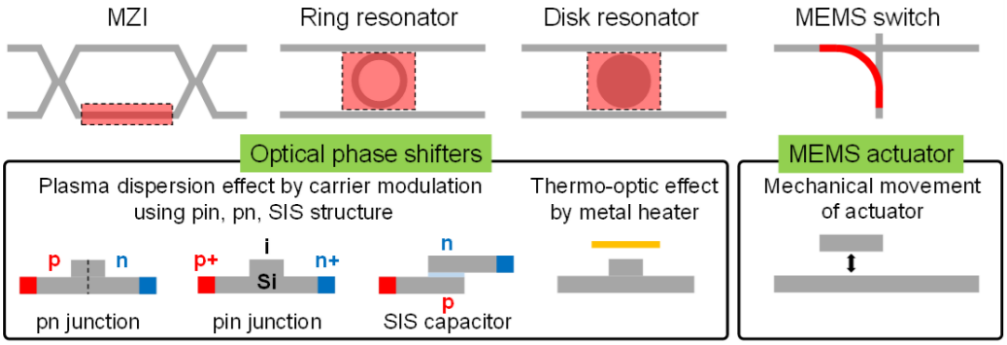

Figure 2.10: Schematic of different types of optical switches, from [34].

Concerning a single switch, the crucial parameters used to estimate the goodness of its modulation are the so-called extinction ratio (ER) and insertion loss (IL), which are respectively defined as

$$ER = 10 \cdot \log\left(\frac{I_{max}}{I_{min}}\right) \quad \text{and} \quad IL = 10 \cdot \log\left(\frac{I_0}{I_{max}}\right) \tag{2.6}$$

in which I_0 is the input intensity, while I_{max} and I_{min} are the maximum and minimum intensity of the modulated signal. Based on the performances of the single element, the main idea is to create switch matrices, to simultaneously modulate the path of multiple signals propagating along parallel or perpendicular waveguides. The maximum dimensions of these matrices depend on their scalability, namely the largest number of signals that can be modulated while maintaining the total

losses under a certain threshold, in order to retain sufficient information about the inputs. Among the available switch mechanisms, MEMS are the one that seem to ensure the highest scalability, since matrices up to 240x240 elements have been reported [35, 36]. They offer a quite compact solution with low losses and a sub-μs operation range, but a high actuation voltage (20 - 40 V). Alternative promising structures mainly exploit the thermo-optic effect obtained through metal heaters, which can offer a comparable power consumption, but much slower speed (around 30 μs) and dimensions up to 32x32 switches [37], or the electro-optic actuation, as in the case of Si *pin* or *pn* junctions, which allow really fast operations (few ns range) and low power consumption (around 1 W) while maintaining relatively reduced losses for matrices up to 32x32 elements [38].
Part of the aim of this project is to study another possible solution for the implementation of optical switch matrices, which, instead of the above mentioned mechanisms, would rely on the optical properties of PCMs, for a potentially non-volatile, fast and low power consuming solution.

2.3 Phase Change Materials

A phase change material is, in its most general definition, a material that presents two (or more) different atomic structures (called states), which affect its physical, optical and electrical properties. Among the large variety of compounds included in this category, during the past few decades the chalcogen-based alloys have attracted more and more interest, starting from their applications for non-volatile memories and optical recordings [14]. Indeed, the reversible, but non-volatile transitions between their structural states, as shown in Fig. 2.11, allows the storage of multi-level information with a retention time in the order of even some years.

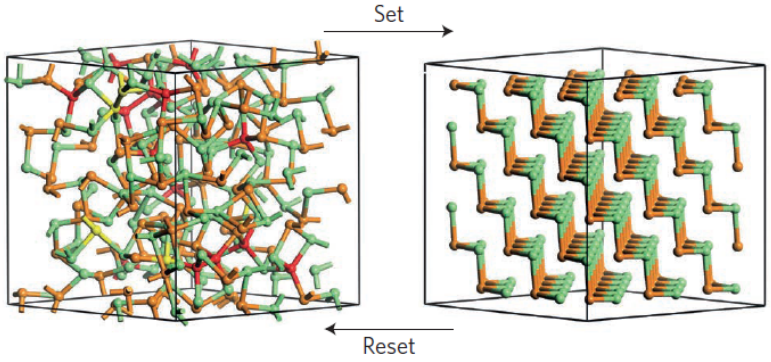

Figure 2.11: Schematic of the reversible and non-volatile transition between the amorphous (left) and crystalline (right) states of a chalcogenide PCM, from [14]

Both transitions, usually in the order of few nanoseconds, can be triggered by

heating the material at different temperatures: the SET operation from amorphous to crystalline is obtained through a slower and more controlled heating over the so-called crystallization temperature, while, vice versa, the RESET is produced by melting the material with a much faster pulse, followed by an abrupt quenching. For this kind of applications, laser beams are employed to actuate the phase change, with an optical readout to extrapolate the stored information.
Today, PCM integration in PICs has led to promising results, especially in the case of germanium, antimony and tellurium alloys obtained as a combination of GeTe and Sb_2Te_3. In particular, GeTe itself, $GeSb_2Te_4$ and, $Ge_2Sb_2Te_5$ (GST-225, or simply GST) are the most employed compounds since, as presented in Fig. 2.12, they show an important change in optical properties, namely the refractive index n and the extinction coefficient k, depending on their state.

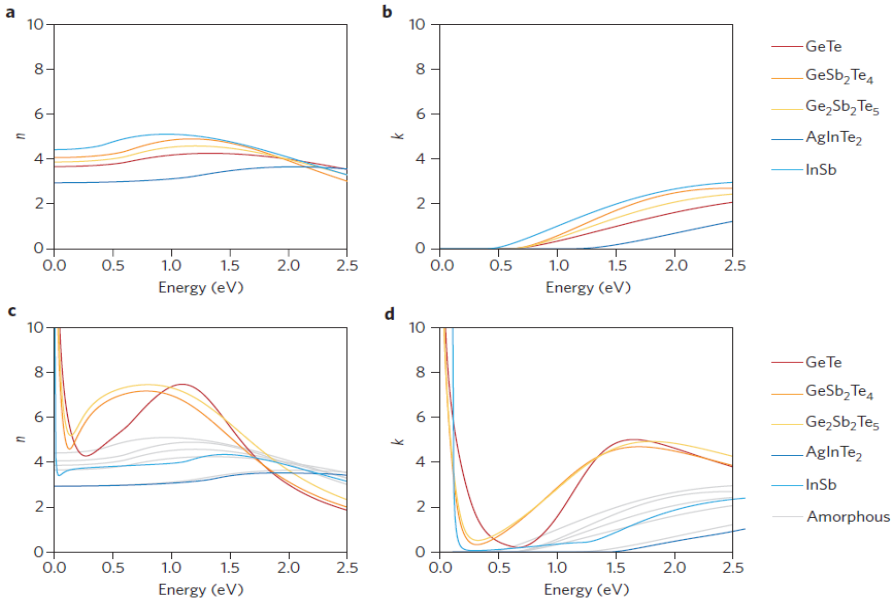

Figure 2.12: Refractive index n and extinction coefficient k of the most common optical PCMs in amorphous (a-b) and crystalline states (c-d), readapted from [14].

Since in the telecommunication range, so for an energy of around 0.8 eV, the variation of n is quite significant, this property is nowadays largely employed to obtain reconfigurable optical devices, like modulators, phase shifters or switches, as it enables a large and efficient signal manipulation. However, the simultaneous increase in k produces higher losses, probably the most detrimental issue when PCMs are involved, and, therefore, their integration should always be complemented by a loss estimation, to evaluate the scalability of the system.
One last consideration about this kind of materials is that they are subjected to spontaneous oxidation when exposed to air, a detrimental process that could even

change their optical parameters. Therefore, to avoid such a deterioration, in current studies a layer of known oxide is deposited on top.

2.3.1 Actuation methods

As mentioned above, the state transition in a PCM can be actuated by means of a localized heating, with different parameters depending on the direction of the transition. In particular, GST alloys present a crystallization temperature between 100 °C and 150 °C, depending on the precise concentration of the single elements, while their melting point, reached for amorphisation, is about 600 °C [17]. In the first case, the transition should be performed in a gradual and controlled way and, therefore, longer (in time) and lower (in intensity) energy pulses are usually employed (between some tens and around 100 ns), in order to give the system the necessary conditions to constitute an ordered structure. On the other side, amorphisation requires much more heating to reach the melting point, while the operation must be performed as fast as possible to avoid the atomic reorganization. As a consequence, in this case, shorter and more intense energy pulses are preferred (in the order of a few ns, or even less).
In general, three main methods can be used to actuate the transition:

- Thermal annealing: the easiest mechanism to be implemented to heat the structure consists in the use of a hotplate, which, obviously, cannot be employed to obtain a localized effect. Indeed, this technique is usually used for general studies on the material as, for example, the extraction of the precise crystallization temperature of the selected alloy [17].
- Optical actuation: heat is provided through a laser beam, which is carefully directed from the external of the chip over the target PCM portion [18, 39]. This approach has the advantage that the laser pulses can be strictly controlled in terms of power and duration, allowing a well localized heating. The main issue is surely represented by the fact that this solution is not integrable and, therefore, an external actuation is always required. Moreover, the alignment of the beam with the sample becomes critical, with the consequent risk of a partial heating and a non complete transition.
- Electrical actuation: heat energy is obtained thanks to the integration of complementary structures, like heaters and electrical contacts, used to apply electrical pulses. The most promising solution consists either in the creation of a highly doped silicon portion underneath the PCM [16], or in the integration of a resistor like a indium-tin-oxide heater [19]. In both cases, the phase transition is driven by Joule heating. This actuation strategy has the disadvantage of more complex design and fabrication to integrate the electrical circuit, but the solution is compact and allows a fully-integrated operation.

In this project, the main idea concerning actuation is to exploit this last option, including doping and metallic contacts in the wings of the same rib waveguides in which the signal propagates. In this way, in principle, a compact and fully-integrated structures could be fabricated.

2.3.2 Deposition techniques

Different techniques can be employed to deposit PCMs, and the choice must be carefully performed, since many proprieties of the deposited film depend on the selected method [17]. Indeed, the material density, composition and stress are affected, together with its optical and electrical parameters, and, therefore, when PCM are involved it is necessary to evaluate how much these quantities are modified during this critical process step. In addition, the deposition technique influences the subsequent processes to pattern the material, since different methods produce films with different step coverage, i.e. with various thicknesses in vertical or horizontal features. A non-conformal step coverage, when less material is deposited on vertical sidewalls with respect to horizontal surfaces, is preferred to perform lift-off processes, since the portions to be removed are well separated from the ones that should remain on the wafer. On the other side, a good conformal step coverage is obtained when the film thickness is uniform along the whole substrate, a condition that makes lift-off more challenging than etching.
Among the wide range of possibilities, sputtering [40] is one of the most promising one, since it is based on physical bombardment of the material source, a solution that is more suitable for alloys as in chalcogenide PCMs. An alternative is represented by pulsed laser deposition (PLD), where the target is irradiated by a laser beam [41]. In both cases, the resulting film presents good density and quite non-homogeneous thickness for a non-conformal step coverage. An even more pronounced effect, with a strongly directional deposition, can be obtained though evaporation: different GST alloys can be deposited either by directly evaporating the already formed compound [42], or by evaporating the single elements in a multi-source process [43], with careful control about the melting point of each of them.
The above mentioned techniques can be all classified as physical vapor depositions (PVD), while a more conformal step coverage can be obtained through chemical vapor depositions (CVD), in which the film is produced thanks to a chemical reaction between the constituents of the alloy at the surface of the target wafer [44]. This solution allows for a good uniformity, and it is particularly suitable to fill high aspect ratio features. As a sub-class of CVD, atomic layer deposition (ALD) is based on the formation of single atomic layers of the material. Therefore, despite the longer time taken by the process, this technique allows for the best growth conformality of the film, and a good control over the deposition rate [45].

Chapter 3

Fabrication Tests on PCMs

The first, fundamental obstacle to overcome in the realization of this project was the novelty of the employed materials. Indeed, on one side, PCMs, and in particular the two selected ones, GeTe and GST-225, are still the subject of many studies, especially in the field of integrated photonics in which they have been only recently introduced [17]. In addition, these materials had never been included in other projects performed at CMI during the past decades: their installation in this cleanroom environment was made only few months ago, specifically for the purpose of this analysis, and therefore both their precise properties and the details about the available techniques to process them had to be determined.
A fundamental aspect for the purpose of this project is to understand how PCMs can be integrated, instead of the commonly employed EBL, through DUV lithography, which could allow a scalable production process with a high throughput (see Sec. 1.2). The scope of this analysis is, therefore, to evaluate the conditions under which these materials can be actually patterned with DUV lithography-compatible equipment, studying which is, among the fabrication alternatives available at CMI, the procedure that will lead to better results.
It is important to point out that this study is not performed at the end of a complete process for the production of real devices, which would require dedicated lithography tools and precise process parameters, not known a priori for new materials. It represents, instead, a preliminary, partial process to obtain all the necessary details about the patterning of PCMs, a crucial step. The outcome of this evaluation is also relevant to understand which are the limitations imposed by this processing choice in terms of resolution, limitations that must be then considered in the design and simulation of the final devices to obtain geometries effectively compatible with these fabrication tools.
In this chapter, the results of the cleanroom processes performed on PCMs and some details about the used machines are outlined. First, the discussion about the choice of the steps to be included in the complete process flow are presented, with focus

on the description of photolithography. Subsequently, the short-loop experiments performed on the PCMs will be illustrated: a complete characterization process, to evaluate the outcome of the materials deposition, is followed by the results of the multiple fabrication tests in two directions, following two main, alternative approaches to pattern the involved materials (lift-off (LO) and etching.)

3.1 Process flow description

The process flow preparation has been performed always considering the main objective of this analysis, that is the implementation of fully-integrated optical components whose efficient fabrication is enabled by DUV lithography, which allows a fast wafer processing applicable in large-scale productions. In order to understand the final goal of this analysis, a schematic of the cross section of the wafer at the starting and end point of the process is presented in Fig. 3.1.

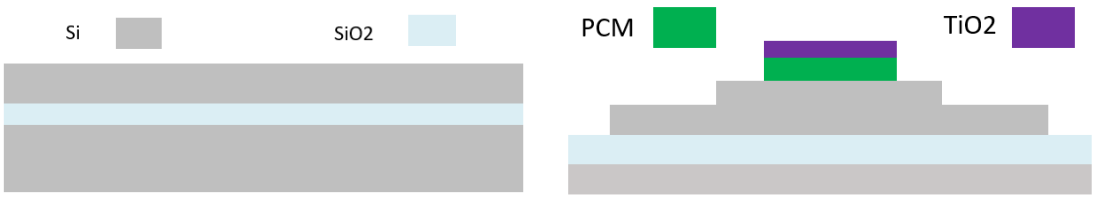

(a) *SOI, with 220 nm device layer* **(b)** *Final structure of the waveguide*

Figure 3.1: Schematic of the section of the initial SOI wafer (left) and the final structure of the Si-PCM hybrid rib waveguide (right), not in scale.

As seen from the picture, the starting point is an SOI wafer as presented in Fig. 2.2, with a BOX of 2 microns and a device layer of 220 nm, but without the cladding oxide, in order to enable the patterning of the Si top layer. On the other side, the final target is a silicon rib waveguide, on top of which the PCM is deposited together with a covering layer of TiO2 to avoid unpredicted oxidation (see Sec. 2.3). The design choice for the waveguide is to have fixed 160-nm-thick wings and 60-nm-thick core, dimensions commonly employed in PIC for various applications. On the other hand, the width of both Si portions and all the geometrical parameters of the deposited materials has been lately determined in the analysis presented in Chapter 4.
The most relevant steps of the complete process flow for the transition between the initial SOI and the final structure are shown in Fig. 3.2. At each stage, the schematic describes the cross section of the structure after the step has been performed, while the bulk Si is not shown as it is not affected during the procedure.

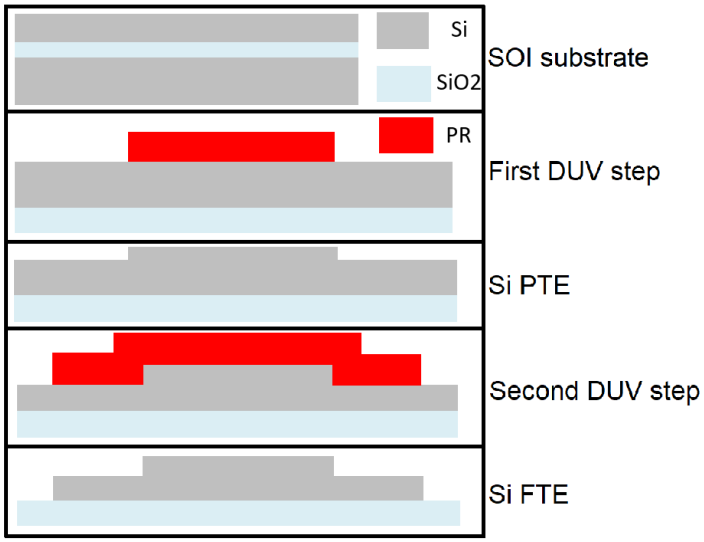

(a) *Si partial and full thickness etch, to obtain the rib WG*

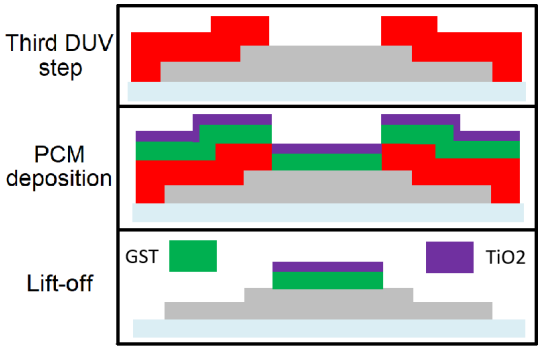

(b) *PCM patterning: lift-off*

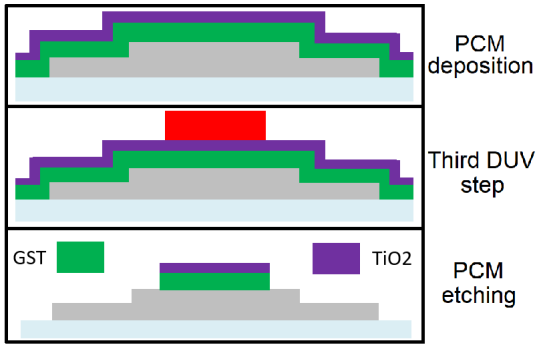

(c) *PCM patterning: etching*

Figure 3.2: Schematic of the most relevant steps of the complete process flow submitted to the approval of the CMI staff.

The first portion of the process concerns the creation of the rib waveguide. The patterning of the device layer is performed in two successive steps, both requiring a dedicated DUV lithography process: first, the central cores are obtained through a so-called Si partial thickness etch (PTE), with the removal of a 60-nm-thick Si layer from the lateral portions; then, the wings are patterned with a full thickness etch (FTE) process, which delimits the waveguides by eliminating the remaining 160 nm of silicon outside these regions.
At this point, the final step consists in the integration of the PCMs. While the previous sections of the procedure have today become a standard way of processing silicon, this last step was the most critical one. Indeed, it was not known how

PCMs could react to techniques commonly used to pattern various kind of materials. Therefore, two main approaches, lift-off and etching, have been tested in parallel, trying to understand which one can provide more promising results.
Actually, the process flow should be completed by the integration of the metallic contacts on the wings of the waveguide. The required steps for this procedure will be included in a future continuation of the project.

For all the described steps, the selective patterning of the involved materials is enabled by DUV lithography, which that can be included in a more general set of techniques called *photolithography*, nowadays present in every process which aims at obtaining features in micro- and nanometric scale. Despite differences in terms of employed energy sources and obtained minimum features dimensions (the so-called critical dimensions (CD)), these techniques are all based on the same working principle: the selective patterning of a material is enabled by the preliminary patterning of a sacrificial layer called photoresist (PR), or simply resist, whose shapes are lately transferred to the target material. The resist is usually constituted by a photo-sensitive polymer whose structure undergoes modifications thanks to the absorbed photons.
Therefore, photolithography employs laser or broadband light sources to irradiate the PR through a so-called mask, selectively open to the radiation in correspondence of the target portions of the resist to be exposed. Finally, the exposed layer is subjected to development, a procedure that removes the superfluous sections, maintaining only the designed features. A schematic of the described process is shown in Fig. 3.3.

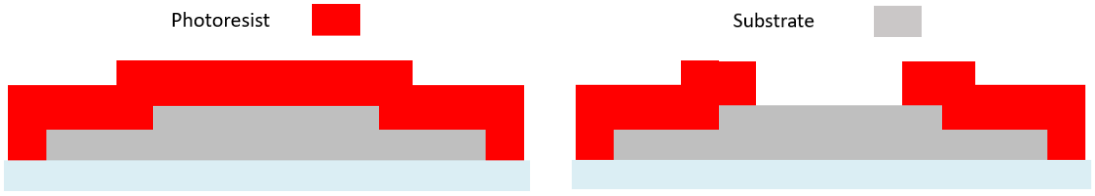

(a) *Resist after deposition* **(b)** *Resist after exposure and development*

Figure 3.3: Schematic of a photolithography step extracted from the process flow.

In general, two main typologies of PR are available, depending on their polarity. On one side, a resist is classified as positive if the exposed regions become more soluble in the developer, since the chemical reaction enabled by the absorbed photons breaks its long polymeric chains. For this reason, the open regions on the mask are the same ones removed in the PR, which presents a positive polarity. On the other side, a resist is negative when the reaction causes the formation of longer and more bounded chains, making the exposed portion more resistant to the developer. In

this case, the unexposed regions are removed and, therefore, the remaining features on the PR are reversed with respect to those on the mask, obtaining a negative polarity. In consequence, the mask design must be performed targeting one of these typologies, fabricating in the second case a layer with opposite features to those transferred on the resist.
Concerning the CMI cleanroom environment, DUV lithography is performed through the ASML PAS 5500/350C stepper, a tool which employs a KrF laser source to generate DUV light at wavelength of $\lambda = 248$ nm. The presence of projection lenses enables a 4x or 5x reductions of the features present on the mask (also referred to as reticle). A single exposure through the reticle only affects a portion of the wafer, but a "step and repeat" procedure allows a faster process over the whole substrate, for a throughput of more that 100 wafers per hour. The expected resolution for multiple features is around 180 nm, while for isolated structures even smaller dimensions can be obtained.
The initial PR deposition (coating) and the final development are made using the ACS200 Gen3 automatic coater and developer, which allows the treatment of positive UV and DUV resists, also performing multi-steps procedures. Indeed, two of the most relevant employed recipes are the deposition of the PR together with a back anti-reflecting coating (BARC), used to reduce the effect of unexpected reflections of the incoming light at the interface with the substrate, and the combination of the final development with a prior post-exposure bake (PEB), to fix the features resolution on the resist. The result is a versatile and fully automatized equipment with a high throughput.

3.2 Required short loop experiments

Since the implemented process flow includes many different steps, among which some have never been tested before, performing the whole routine in sequence, and without preliminary tests, would have represented a procedure with a low probability of success. Moreover, in case of a non-working final device, the research of the processing error would have been too complicated. In consequence, different short loop experiments have been performed with the idea of testing some steps of the process flow singularly.
Different portions of the procedure can be studied independently. In particular, the three main blocks in which the process flow can be divided concern the Si patterning (to obtain the rib waveguide), the PCM treatment (both for its deposition and patterning) and the integration of the metallic electrodes, among which only the second one has been analyzed in detail. Indeed, on the one hand, steps as Si PTE and FTE has been already performed in other research project of the group [46], and therefore the required optimal process parameters are well known. On the

other hand, tests on the electrodes patterning could be carried out only at the end of the complete process, therefore after having completed all the other procedures. Therefore, from the fabrication point of view, the analysis performed in the context of this project has been focused only on the PCMs treatment. First, a characterization of the deposited materials has been carried out with the aim of extracting their optical and structural properties, together with the properties of the obtained thin films. Then, the two selected techniques to pattern the PCMs, i.e. lift-off and etching, has been studied in parallel with the idea of proving that DUV lithography can be effectively employed to pattern this kind of materials, and to estimate the associated optimal process parameters.
An obstacle to this last analysis was represented by the lack of dedicated lithography masks, which can be produced only after a specific design procedure and a highly expensive fabrication. However, an effective solution to overcome this issue relied on the use of reticles already employed in one of the other projects of the group, which presented relevant features, similar in shape and dimensions to the ones required in this study. Since no working device was expected to be obtained at the end of these procedures, all the performed experiments have been carried out on simple silicon test wafer, instead of the more expensive SOI.

3.3 PCMs deposition and characterization

3.3.1 Sputtering deposition of PCMs

Among the large variety of available solutions for the deposition of PCMs (see Sec. 2.3.2), sputtering was selected as the safest technique to work with this kind of materials without denaturing them. Indeed, this technique has been widely analyzed and employed in many recent studies involving PCMs [15, 16, 47], and it presents the great advantage to maintain the same stoichiometry of the source on the deposited film, avoiding the risk of unexpected variations in its composition. In addition, sputtering allows the deposition of even complex alloys, as GST, since no chemical reaction is required.
A schematic of the sputtering chamber is shown in Fig. 3.4. The technique relies on physical bombardment of a bulky source of the material to be deposited by means of heavy ions, usually obtained by non-reagent elements as argon. The latter cause the detachment of surface atoms, that are then directed in a low pressure ambient towards the wafer at the bottom of the chamber.

The source and the wafer are disposed onto two electrodes, between which a high potential is applied both to ionize the Ar atoms and to accelerate them. Depending on the voltage, two main modalities are possible, namely DC (direct current) and RF (radio-frequency). In the first case, a constant voltage of few hundreds of volts is applied, with the advantage of a simple implementation, while in the second

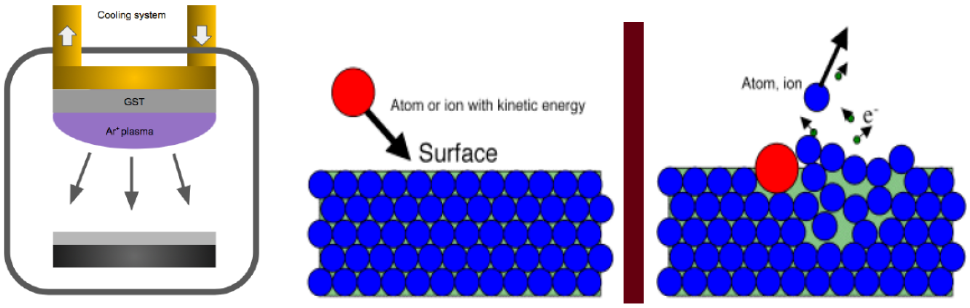

(a) *Sputtering chamber* **(b)** *Ion bombardment of the target surface*

Figure 3.4: Schematic of the typical sputtering chamber (left) and working principle (right), taken from [17]

the voltage is periodically inverted, avoiding the risk of charge accumulation at the surface of the target and consequently allowing also the deposition of non-conductive materials. Regardless of the chosen modality, the resulting film always present poor conformality (see Sec. 2.3.2), since the operation is performed at low pressure and, therefore, the atoms removed from the source travel along straight lines to reach the wafer. A possible way to improve the result (if required) consists in a moderate heating of the substrate to 100-400 °C, to promote both the material adhesion and a partial surface migration of the atoms.
For the purpose of this project, the selected PCMs have been installed inside the Alliance-Concept DP 650 tool, one of the available sputtering machines at CMI. which presents a main chamber at low pressure, with 6 source holders for the deposition of multi-layered structures, and a loadlock chamber to load the sample. Both DC and RF modalities are available. The selected recipe to deposit both PCMs is a DC sputtering at room temperature, also used for the deposition of a thin TiO_2 layer on top of them to avoid spontaneous oxidation (see Sec. 2.3).

3.3.2 Deposition rate extraction

The most important parameter to be determined while dealing with the deposition of an unknown material is the rate at which it accumulates at the surface. This quantity is specific for each material, but may vary depending on the conditions at which the deposition is performed. Therefore, once a certain machine and recipe have been selected, it is necessary to perform some deposition tests evaluating the thickness of the obtained films.
Different techniques are available to measure the thickness of multi-layered structures, first and foremost ellipsometry, which can provide accurate results if the optical parameters of the involved materials are known. Unfortunately, in this case

the latter were unknown at this early stage of the project, therefore another simple solution has been employed: some of the wafers have been covered with a strip of adhesive tape, removed after the deposition. In this way, the PCM deposited on top of the tape is removed as well, while it remains in the rest of the wafer, forming a step. The height of the latter is then measured through a mechanical profilometer. An example of one of the measurements is reported in Fig. 3.5.

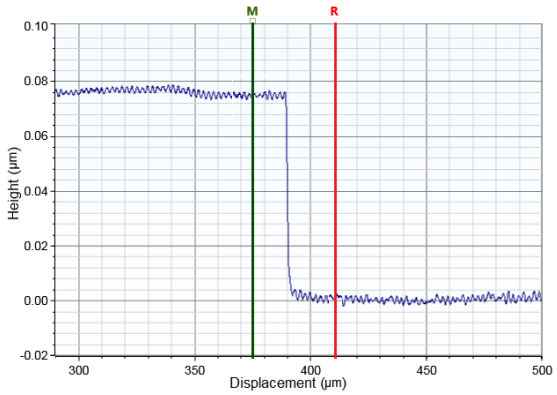

Figure 3.5: Surface profile of a deposition test (mechanical profilometer).

Analyzing the profile of the surface (in blue), the step is measured by disposing two dedicated cursors at the edges of the feature. The software automatically computes the vertical separation between the points in which the line of the surface profile is crossed. Many different wafers have been tested with this procedure, and the resulting thicknesses of the step for some relevant cases are reported in Table 3.1.

PCM	**Deposition time (s)**	**Step thickness (nm)** (center)	**Step th. (nm)** (edge)
GeTe	20	23-25	20-22
GeTe	40	47-49	43-45
GST	30	50-52	45-47
GST	50	83-85	75-77

Table 3.1: Thickness of the feature obtained on different samples, for both PCMs and for different deposition times.

Analyzing the results, it can be noticed that the deposition is not completely uniform on the whole wafer. Therefore, the sputtering rate has been extracted separately for the center of the wafer, and as an average value, obtaining, respectively, for GST around 17 Å/s and 14 Å/s, while for GeTe were 12 Å/s and 10 Å/s.

3.3.3 Residual stress measurement

Another relevant parameter to be analyzed after the deposition of a new material is the eventual presence of residual stress on the film. Although relevant issues about stress on PCM layers for integrated photonics have never been outlined in recent studies, it has been largely reported that this quantity can lead to numerous detrimental effects on the structure [48]. Indeed, an excess in residual stress can potentially affect the performances and durability of the concerned portion of the device, causing in the worst case a crack of the structure, especially in suspended layers usually present in MEMS components. In particular, concerning the outcome of this project, a potential strong residual stress could lead to bad adhesion of the deposited layer, with the risk of detachment in some portions, or to a stretching of the atomic bonds with consequent modifications of the optical parameters, especially in the crystalline state.
This kind of analysis has been performed at CMI with the Toho Technology FLX-2320-S stress measurement tool, suitable for the investigation of thin films. In order to have a reference measurement, the machine measures the curvature of the wafer along different directions without the material under examination. The procedure is then repeated after its deposition, and the software computes the difference between this last evaluation and the reference, extracting from it the value and the typology (compressive or tensile) of the film stress.
To have a practical, but still representative analysis, the measurements have been performed along two perpendicular directions, obtained with a rotation of the wafer of 90 degrees. Fig. 3.6 shows the results of one of the studied wafers. The blue dots represent the deflection of the wafer along the measurement direction.

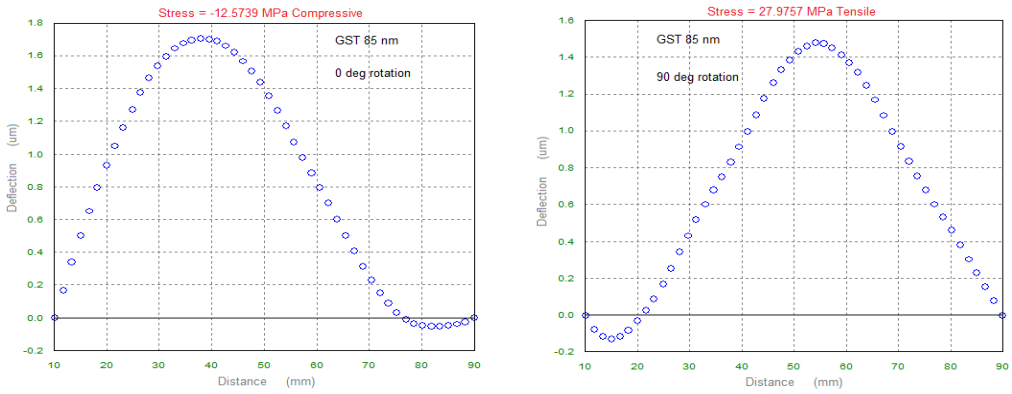

(a) *Wafer rotation 0 degrees* **(b)** *Wafer rotation 90 degrees*

Figure 3.6: Stress measurements at a wafer rotation of 0 and 90 degrees after the deposition of a 85 nm thick layer of GST over a silicon test wafer.

It can be observed that the measured stress is compressive for one orientation of the wafer and tensile for the other, with values around 13 MPa and 28 MPa respectively, and similar results have been obtained for different analyzed films. However, it has been indicated in recent studies [48] that in structures with high residual stress, the result of this kind of measurements is in the order of some hundreds of MPa, or even more. Therefore, for this analysis, we can conclude that the PCM layers in exam only present negligible values of stress after deposition.

3.3.4 Surface analysis after deposition

One last property of the result of the sputtering process to be determined it the state in which the PCM is deposited. It has been already reported in different studies that the obtained PCM films are amorphous [15, 17] for different kind of deposition techniques. In addition, in sputtering only atoms alone or in small clusters are deposited one after the other in a quite random and fast process and, therefore, they should not have the correct conditions to form ordered structures. As a consequence, it was straightforward to assume that also in the context of this project amorphous-as-deposited PCM films are obtained using this procedure.
However, a quick analysis of the deposited layers was anyway necessary. In order to study the surface of the films, an effective alternative to atomic force microscopy (AFM), more suitable for this kind of analysis, but not available when this portion of the project has been performed, was to take pictures of the surface with the scanning electron microscope (SEM).
SEM images have been obtained during the semester with two alternative tools, Zeiss LEO 1550 and Zeiss MERLIN which, despite some differences in resolution (around 5 nm against 1 nm respectively), present almost the same characteristics. They rely on the same principle: an electron beam is extracted from a Field Emission Gun by a strong applied voltage, and then directed vertically towards the sample across a column maintained in very high vacuum ($10^{-}10$ mbar). Along the latter, alignment coils and objective lenses focus and deviate the beam towards the spot selected through the associated software. The high-resolution image is then obtained analyzing the electrons coming out from the surface of the sample, mainly part of the so-called backscattered electrons.

Since the materials under examination present a highly reflecting surface, the observation of areas with PCM alone would have been very challenging. Therefore, the same procedure employed for the extraction of the deposition rate (see Sec. 3.3.2) was followed: a tape has been removed after the PCM sputtering, and the resulting step allowed to observe the differences between the deposited material and silicon underneath. Two examples of SEM pictures of different analyzed wafers are shown in Fig. 3.7.

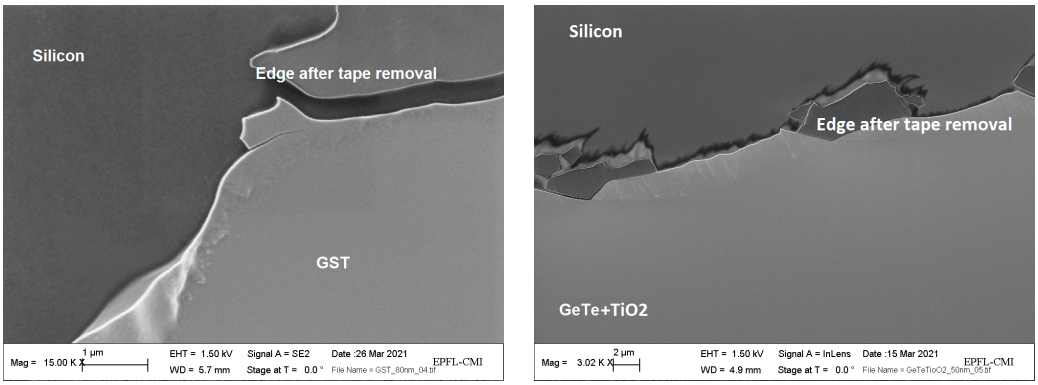

(a) *GST (80 nm) over Si* **(b)** *GeTe (50 nm) + TiO_2 (10 nm) over Si*

Figure 3.7: SEM images of the surface of different deposited PCM layers (light gray), in contrast with the silicon substrate (dark gray).

Apart from the rough edge due to the abrupt removal of the tape, it can be noticed that both GST alone on the left and GeTe covered with TiO_2 on the right present high uniformity and a homogeneous surface. The same result has been obtained also in other portions of the wafer, away from the step, and for other samples, regardless of the choice of the PCM, of their thickness and of the presence of the oxide on top. The absence of ordered structures could prove the amorphous character of the obtained layers, but a more accurate control at the AFM or with X-rays tests should be later necessary to have a definitive confirmation.

3.3.5 Ellipsometry

The conclusive aspect of the preliminary characterization procedure consisted in the extraction of the optical parameters of the PCMs. Even if these properties have been already widely analyzed during the past twenty years, different expressions of the dispersion relation and, consequently, different values of refractive index n and extinction coefficient k have been obtained in different studies. Indeed, it has been proven that these variations can be attributed to the deposition and fabrication conditions at which the selected material is processed [49], therefore, it is necessary to estimate the optical parameters each time a new process is followed.
Ellipsometry is the most common technique employed for this kind of analysis. A light beam with known linear polarisation, and coming from a fixed angle, is focused onto a selected spot on the sample and, after its reflection at the interface between different layers of the wafer, the beam is collected on the opposite side. Through the evaluation of the change of polarization of the light, in general elliptically polarised, the tool can extract the optical parameters of the layers under examination and/or

their thickness if required.
However, this tool can be easily employed only when the dispersion relation of the involved materials is well known, or, alternatively, if the parameters of the model used to approximate it are already given, while the procedure becomes much more complicated when an almost unknown material is analyzed. In the case of PCMs, the lack of uniform information in literature did not allow to have a reference dispersion relation, and the fitting procedure of the performed measurements could not produce satisfactory results.
A solution to overcome this issue was found only at the end of the period of the project. A collaboration has been established with the Silicon Austria Lab, which helped in the extraction of the parameters. The results of the measurements for different samples of both GeTe and GST, in the amorphous state, are presented in Fig. 3.8.

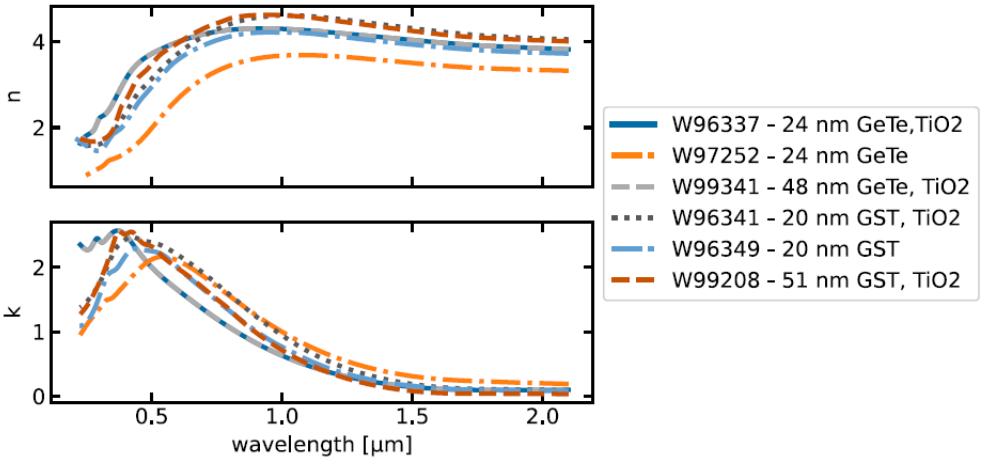

Figure 3.8: Dispersion relation of different test samples, covered by amorphous GeTe or GST, in some cases covered by around 10 nm of TiO_2, from [50].

By comparing these experimental results with the curves presented in Fig. 2.12, it can be observed that for most of the curves, and for both materials, the values of refractive index are almost the same, equal to around 4 at a wavelength of 1550 nm. Concerning k, however, both PCMs presents a consistent discrepancy, with values around 1 instead of 1.9 and 0.1 for GST and GeTe respectively. The corresponding values for the crystalline state have still to be determined.
Unfortunately, these results only arrived at the very end of the semester and, therefore, in the meantime, all the simulation work has been performed with values of the optical parameters extracted from the [14]. A further step in this project would be to perform again the simulations changing the parameters of the involved PCM accordingly to the measurements results.

3.4 First approach: Lift-off

The first technique selected to pattern the PCMs is lift-off. As presented in Fig. 3.2(b), in this process photolithography is performed directly on the substrate, while the material to be patterned is lately deposited over the resist. Subsequently, the latter is removed thanks to a stripper solution, eliminating also the portions of the material deposited on top of it. Therefore, in the end, the only features that remain on the wafer correspond to the regions in which the PR was open.
This approach surely has the advantage to avoid the risk of damaging the substrate, which is only in contact with the resist in portions in which the PCM is removed. Moreover, the solvent used for the final strip is totally compatible with silicon and, therefore, no corrosion or other types of reactions can happen. Nevertheless, the main drawback is that the sidewalls of the resist are never perfectly vertical, since the upper portion is usually overexposed with respect to the bottom one. Therefore, the material can deposit also on these lateral edges. If this effect is so extended that there is a continuity between the portions over the resist and those in contact with the substrate, there is the risk of removing the whole structure. In intermediate situations, the solvent cannot easily reach all the portions of the PR, and the process takes a long time. In consequence, to avoid this issue, the thickness ratio between the deposited material and the resist should be at least 1:3 (1:5 is preferable).
In the context of CMI, lift-off is performed by immersing the wafers into wet benches containing the Remover 1165. If the adhesion of the material to the substrate is good, the process can be speed up thanks to the sonicator, a tool that generates acoustic waves inside the remover and helps the resist detachment. At the end, the wafer must be immersed into isopropanol, which contrasts the solvent, and then rinsed in water to eliminate all the residuals.
Different lift-off tests have been performed inspecting all the aspects that can influence the process. Since the first attempts, completely similar results have been obtained depositing either GeTe or GST, even on wafer processed together. Therefore, in the following sections the description of the processes will be performed, for the sake of simplicity, without specifying the nature of the PCM.

3.4.1 First test

The first attempt was performed to understand, above all, if this approach can be effectively followed in this kind of applications. Indeed, the limitations mentioned above usually relegate the use of lift-off for micrometric features, and previous tests carried out for other projects involving DUV lithography at CMI led to bad results. In consequence, as suggested by the CMI staff, the safest choices in terms of type of PR and process parameters have been made.

In particular, among the two main DUV resists, JSR M108Y and JSR M35G, respectively 450 nm and 1.2 μm thick, the second one was selected (without BARC, not used for lift-off) to increase the thickness ratio with the deposited PCM. Moreover, since the optimal parameters for exposure, namely the precise values of dose and focus of the light beam (both affecting the CD), were not known, the suggested approach was to perform a dose-focus (d-f) matrix. In this way, instead of processing the whole wafer with the same parameters, each die is exposed with a different d-f combination. The optimal values can be then estimated a posteriori, observing in which region of the wafer the best results in terms of CD are obtained. A quite large d-f matrix, centered in the suggested values of 45-0 respectively, with step 5 for dose and 0.5 for focus, was selected, in order to have a sufficiently wide range of combinations to include the optimal region.
Before depositing the PCM on top, the result of this lithography step have been observed at the SEM, in order to understand in which portions of the wafer the resist was correctly open, and in which the exposure parameters were not sufficient to create the features. Although this kind of observation is quite hard to perform, since the PR is not conducting and electrons tend to accumulate on its surface distorting the image, the aim is, in case of a bad result, to discriminate between an issue due to lithography or to the successive steps (deposition and resist strip). Fig. 3.9 shows the effect of a dose variation.

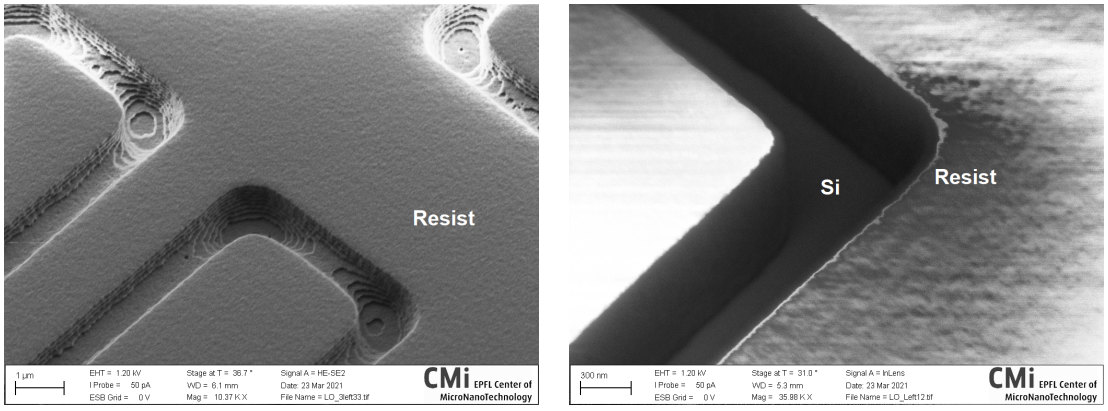

(a) *Dose 30, focus 0, feature not open* **(b)** *Dose 45, focus 0, resist open*

Figure 3.9: Resist observation for the first LO test. A too low dose (left) does not allow the complete exposure of the PR, which happens for higher dose (right).

As it can be noticed on the left, a too low dose leads to an incomplete exposure of the resist, which becomes soluble in the remover only on its surface. Therefore, after development some residuals remain at the bottom of the analyzed feature, leading to the complete removal of the material deposited on top. On the right, a

higher dose allows instead the complete opening of the resist and, in consequence, a bad result for the whole process in this region of the wafer cannot be, in principle, attributed to the lithography step.
The influence of a focus variation is different. For a zero value, the light beam is collimated exactly on the surface of the wafer, leading in principle to vertical walls. For negative or positive values, the collimation point is vertically shifted up or down respectively, with a non uniform exposure of the resist and, consequently, tilted sidewalls. Fig. 3.10 presents the described effect.

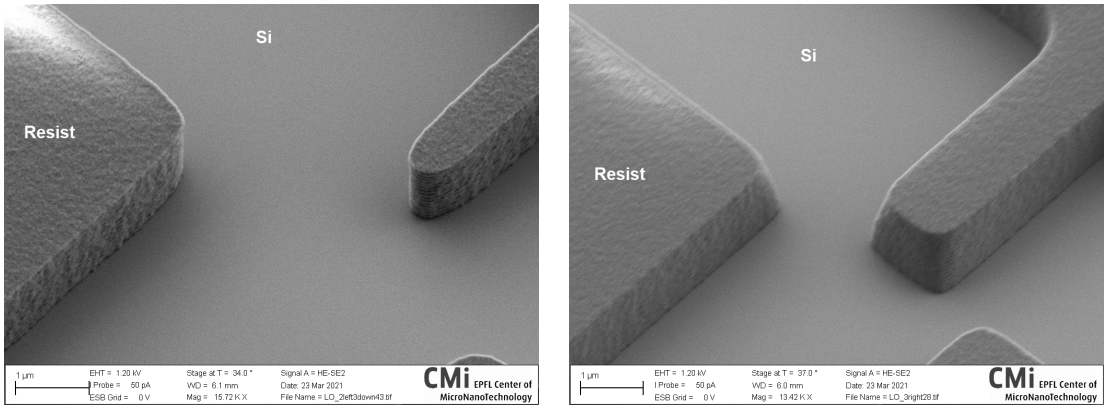

(a) *Dose 45, focus -1.5* **(b)** *Dose 45, focus +1.5*

Figure 3.10: Resist observation for the first LO test. A negative focus (left) leads to sidewalls with negative slopes, and vice versa for a positive focus (right).

It can be observed, in particular, that a negative focus, for which the beam is collimated over the resist, produces features with negative edge slopes, with a thinner and thinner section moving from the surface of the resist to the substrate. The opposite effect is obtained for a positive value. In principle, the first situation is preferable for lift-off since, in this way, the material deposition on the sidewalls is greatly reduced, and the process may be faster. However, in regions exposed with too high or too low values of focus it was observed that smaller features, in the order of few hundreds of nm, were completely distorted.
Once completed the resist analysis, around 50 nm of PCM and 10 of TiO_2 have been deposited on top, and the wafer was immersed in the remover. Again, the safer option was to avoid the use of sonicator, since it would have been detrimental in case of bad adhesion of the material over silicon. After few hours, and even the day after (a sufficient timing for a common lift-off process), a quick observation with the naked eye showed that no modification to the surface of the wafer happened. Therefore, only after one week the latter was removed by the solution, cleaned and observed again at the SEM. Many of the dies at the edges of the wafer, for extreme

values of focus and at too low dose, were completely removed, as expected from the resist observation, while only some modifications happened in the other portions. The results of this step are presented in Fig. 3.11.

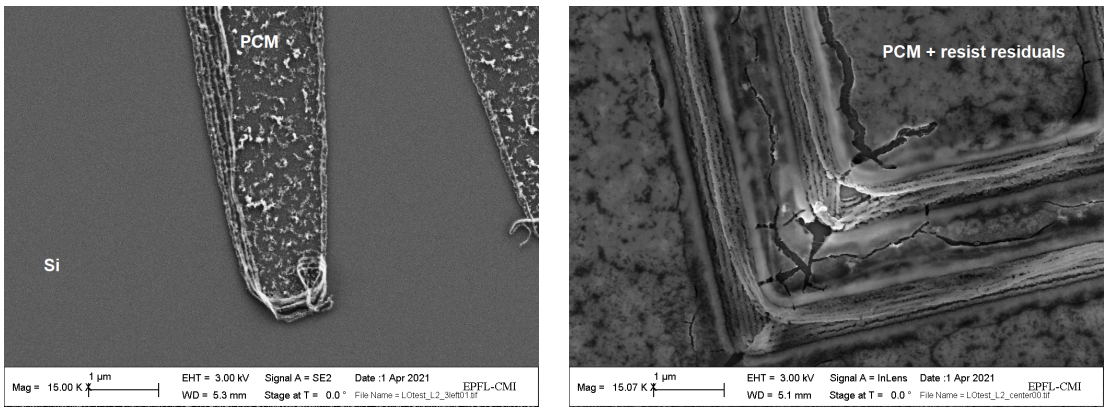

(a) *Isolated feature* **(b)** *Multiple parallel lines*

Figure 3.11: Results of the first LO test after one week in the remover. Process completed for isolated features (left), not in the case of multiple lines (right).

The process was completed only in the case of isolated structures, surrounded by large portions of resist which have been completely removed (Fig. 3.11(a)). However, even in this case some residuals remained at the edges of the features, and the quality of the PCM film was very poor if compared to the ones presented in Fig. 3.7. On the other side, the process was far from being completed in regions with multiple features, close enough to be separated only by small sections of PR, hardly reached by the solvent (Fig. 3.11(b)). Indeed, in this case only small cracks in the structure were created, and the majority of the resist was still present.
At this point, the wafer was immersed again in the solvent. The main idea was to understand if the process could restart, even if usually this procedure must be avoided, and the remover should act on the resist in a continuous way. After one additional week, only negligible changes have been observed and, therefore, a more harsh approach was adopted, employing the sonicator for 90 seconds. Finally, this last step improved the situation, as shown in Fig. 3.12.

Although even in this case the process was not perfectly completed, this last observation led to interesting conclusions. Indeed, the sonicator helped in the removal of many residual portions of the resist both for isolated or grouped features, but without damaging or completely removing the deposited layer. Moreover, the dimensions of the obtained structures are around 500 nm, highly promising for the context of this project. However, the quality of the film is poor, and these results have been obtained only in few portions of the wafer, while in other regions the

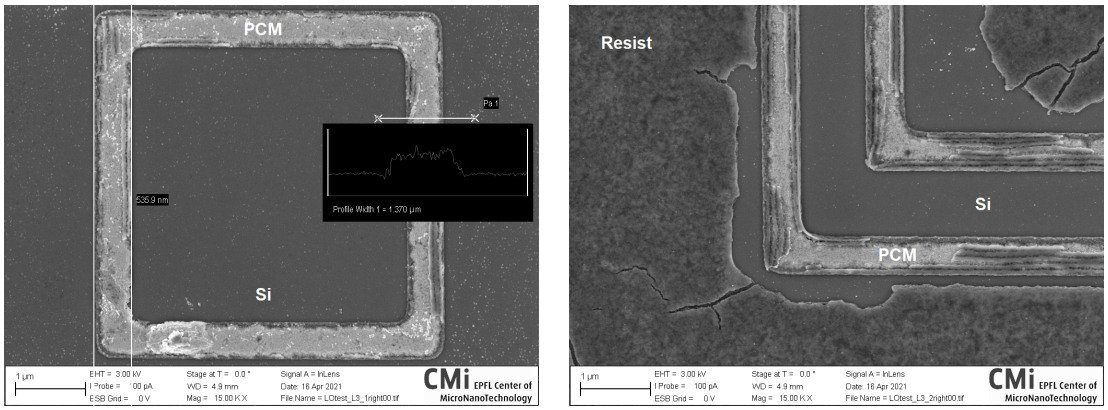

(a) *Isolated feature* **(b)** *Multiple parallel lines*

Figure 3.12: Results of the first LO test after the use of sonicator. Improvements have been observed both for isolated structures (left) and parallel lines (right).

situation was close to the previous observation.
In conclusion, even if the outcome is still not acceptable for future applications, this test proved that lift-off can be applied for features processed by DUV lithography, so in the order of few hundreds of nanometers, and that the adhesion of the PCM to the Si substrate is good enough to withstand the use of sonicator.

3.4.2 Second test

The results of the first test have been exploited for the realization of a second attempt, with the idea to improve the process in its weak points, primarily the conclusive lift-off, and to extract additional information about the optimal parameters for lithography and the result of the deposition.
This time, two wafers have been processed in the same way as in the first test. For both, resist M35G was maintained, together with the d-f matrix described above. The only variation relied in the choice of two different lithography reticles, previously employed in other projects but meant for an etching process, so with reversed features with respect to those required for a lift-off. However, the idea behind this decision was to obtain bigger portions to observe the resulting quality of the deposited film. Moreover, these masks presented anyway some test structures useful for the inspection of the exposure parameters.
The preliminary resist observation in both wafers gave similar results to the first test, with a well developed resist in the center, and not completely open at the edges. In particular, an accurate inspection of peculiar test structures, repeated in every die, allowed to understand that the optimal region lies around the center

of the wafer, with 0 focus and slightly lower doses with respect to the suggested one of 45. For higher values, indeed, the same features were larger than the ones designed on the mask. In addition, an accurate examination of the status of the wafer after deposition was performed, to evaluate the quality of the obtained PCM both on the substrate and on the sidewalls. The outcome is shown in Fig. 3.13.

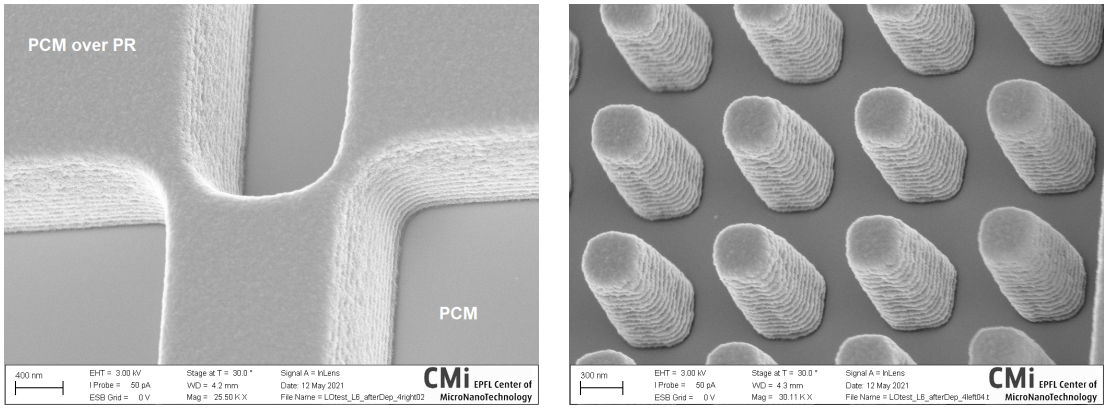

(a) *Test structures: bars* **(b)** *Test structures: dots*

Figure 3.13: Results of the PCM deposition for the second LO test.

As presented in both pictures, the PCM completely covers the sidewalls of the resist, which present a wavy shape, either due to the nature of the polymer, or to some artifacts of photolithography, which anyway does not influence the final result. A similar result was observed in both wafers and in many different portions of the surface. This is surely the reason why the PR strip takes such a long time. At the end of this imaging step, the samples have been immersed in the remover and left inside the solution for a week, after the action of two minutes of sonicator. The results of the final observation at the SEM are presented in Fig. 3.14.

It can be noticed that not only the process is completed, and no portion of the resist remained attached on the surface, but also, more importantly, the quality of the obtained film is very good. Indeed, despite little contamination probably coming from the solvent, previously employed by other CMI users, the surface is completely smooth and uniform, as previously presented in Fig. 3.7. In addition, in Fig. 3.14(b) it can be observed that even features in the order of 300 nm can be obtained, with a gap of only 150 nm. An analysis of the same structure in other dies of the wafer led to the conclusion that this is more or less the lowest bound for resolution, since for smaller gaps some of the fingers had been removed. On the contrary, smaller features, down to around 200 nm have been observed. Those limits confirm the theoretical expectation for this kind of DUV equipment (see Sec. 3.1).

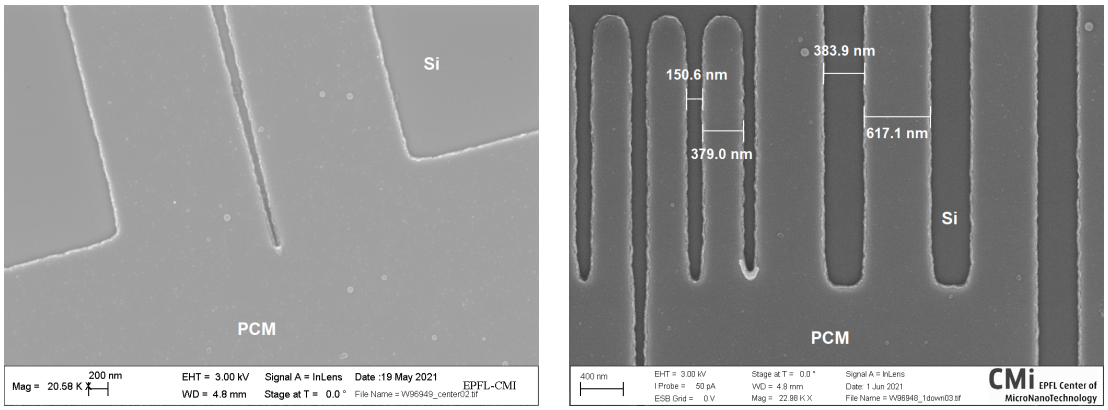

(a) *Test structures for metallic contacts* **(b)** *Test structures: fingers*

Figure 3.14: Results of the second LO test.

In conclusion, the result of this second lift-off attempt are highly promising, with resolved features in the order of 200 nm and a high quality film. Further tests were anyway necessary to try out the same process with a photolithography mask actually meant for lift-off.

3.4.3 Third test

The third test has been performed with the intent of obtaining the same good result of the previous one, but with the lithography mask employed in the first attempt. In parallel, one last important goal was the more precise extraction of the optimal parameters for the exposure step.
Also in this case two wafers have been processed, but with different resists, attempting the same procedure also with the 450-nm-thick M108Y. Because of their different thicknesses, the two PR have been exposed with different d-f matrices: since in the previous test the combinations applied to the edge dies led to bad results, a slightly narrower range was selected for the resist M35G, always centered in 45-0, but reducing the steps to 3 and 0.1 respectively; for the thinner resist, lower dose values are required for a good exposure, therefore the chosen d-f matrix was centered in 30-0, with variations of 5 and 0.5.
The following processes have been performed exactly as in the previous tests. The only difference was the addition of a second step in the sonicator after few days of immersion in the remover, with the aim of speeding up the resist strip. Indeed, this time the process was completed in 5 days. The final results are shown in Fig. 3.15.

Unfortunately, it can be observed that the outcome was negative for both wafers. Indeed, regardless of the employed resist, in both cases large portions of the features

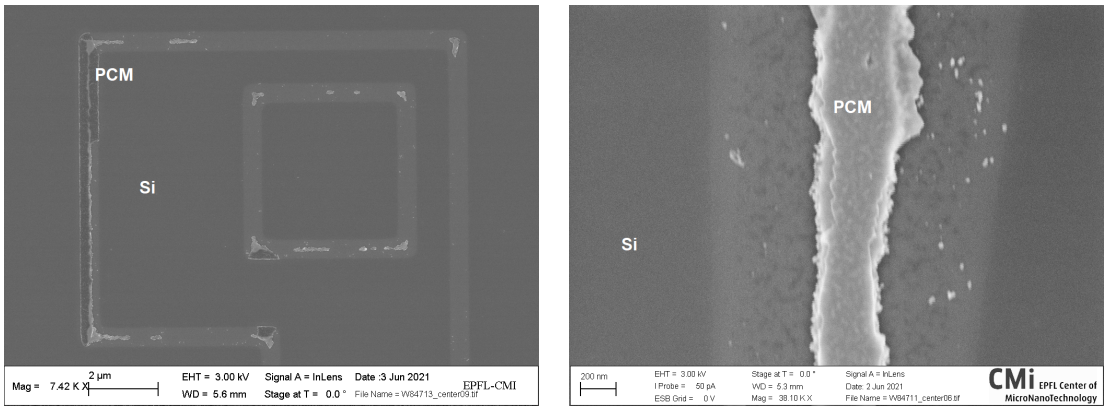

(a) *Interconnections, resist M35G* **(b)** *Grating coupler, resist M108Y*

Figure 3.15: Results of the third LO test.

were removed, and even the ones remained on the surface presented a bad film quality, and a non uniform structure. In particular, Fig. 3.15(b) shows a detail which clarifies the situation: the central portion of the feature was still present on the wafer, while the sides only left a shadow on the substrate. A possible explanation of this phenomenon relies on the fact that, even if the resist seemed open in the preliminary observation, a thin portion on the bottom of the feature was not removed during its development. In this case, the remover could have penetrated under the edges of the features, eliminating those lateral portions. However, an alternative interpretation for this result is a too harsh treatment with the sonicator, even if some features were not completely removed.
An additional test was then necessary to investigate the reason behind this result, with particular attention to the result of the lithography step.

3.4.4 Final test

The successive attempt was performed exactly in the same way of the third one. Again, two wafers with different resists have been processed, but this time, after their development, an additional step was included to eliminate possible residuals from the bottom of the features. This procedure is called Descum, and consists in exposing the resists to a plasma cleaning at low power (for 20 seconds at 200 W in this case), based on a flow of oxygen plasma. The latter is generally used to completely remove the resist in other applications, but in this situation it is employed only for a limited amount of time, eliminating only a thin surface portion. The following steps were maintained as in the other attempts, and again the wafers remained in the remover for a week with only an initial use of sonicator. All the

adopted measures finally led to a satisfying result, as presented in Fig. 3.16.

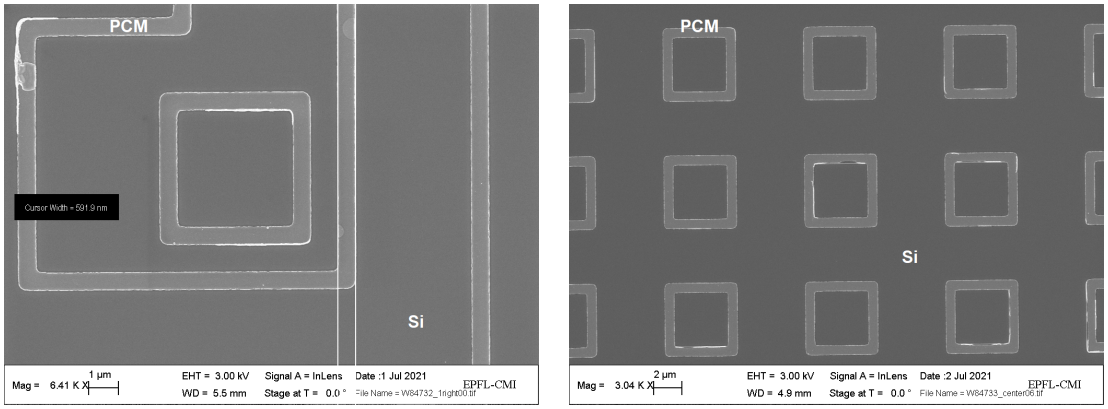

(a) *Interconnections, resist M35G* **(b)** *Square test structures, resist M108Y*

Figure 3.16: Results of the final LO test.

It can be observed that high quality films are present around the center of both wafers, and that the same features were produced whatever the employed resist. Actually, the process was not completely finished in the whole wafer, since, especially in the case of M108Y, in the edge dies some residuals of PR still remained in the middle of the smallest features. Anyway, we can conclude that the outcome of this final attempt clearly proved that lift-off is possible for this kind of application. One last point to be analyzed concerns the optimal exposure parameters: an observation of the smallest features present on the wafer coated with M35G confirmed that the optimal region lies on a zero focus value, and for doses slightly smaller than the one applied in the center, since the best results in terms of feature dimensions and proportions have been obtained for doses between 40 and 45. On the other side, similar results have been obtained also for the thinner resist, with optimal region located around the center of the wafer, for doses around 25. Definitive trials in this regards could be performed with a very narrow matrix in these suggested doses ranges, to finalize this last matter.

3.5 Second approach: Etching

The second alternative to pattern the PCMs is etching. As presented in Fig. 3.2(c), this technique leads to the selective removal of unwanted areas of a film already deposited on the substrate. Therefore, in opposition to what happens for lift-off, the photolithography step is performed after the deposition of the target material, with the aim of masking the areas that should remain on the wafer during the process.

In general, two main, alternative approaches can be employed: in wet etching, the material is dissolved in chemical solutions, which react with the surface of the immersed wafer; in dry etching, usually the reagents are in gases in form of a plasma, although in some cases a physical bombardment of the surface is employed without the need of a chemical reaction. Wet solutions generally perform a stronger action on the wafer, even allowing the selective removal of highly resistant materials, but they are commonly quite dangerous mixtures that cannot be employed with delicate targets. On the other hand, dry etching is usually a safer approach that is preferable when its action can be sufficient to obtain the required patterning.
Dry etching is considered to be the most suitable solution for PCMs to obtain good film quality avoiding a consistent damage of the sidewalls. In particular, during the past few years promising results have been obtained through inductive coupled plasma (ICP), a process in which a reactive plasma is created by RF generators through inductive coils, and that is being investigated in many applications [51, 52]. However, in the cleanroom environment of CMI, the suggested method to etch PCMs is ion beam etching (IBE), a technique that exploits ICP, but relies on ion bombardment of the surface and not on chemical reactions. The process is similar to the one employed for sputtering (see Sec. 3.3.1), with the generation of Ar^+ ions that, subsequently, are accelerated towards the sample to physically remove portions of the material on the surface. Since no chemical reaction is required, this procedure can be, in principle, applied for any kind of material and, therefore, it has been selected as a safe technique to pattern PCMs without the need of exotic or dangerous etchants.

In particular, the machine used for this project is Veeco Nexus IBE350 ion etcher, a tool that relies on the generation of a 350 mm ion beam controlled by a three-grids collimation optics system, with a large variety of energy capability (from 50V to 800V) to allow either a low ion damage of the surface, or a quick etch of different materials. Very low pressures (down to 10^{-7} mbar) avoid the risk of contamination of the chamber or of the wafer, and a movable wafer holder can be finely tilted for a better shape control over complex structures. The system is equipped with an end-point detection mechanism which monitors the concentration of the elements in the chamber, plotting output curves in a concentration vs time graph. When the curve relative to a specific elements rises, it means the latter is being removed from the sample, and detected in high concentrations inside the chamber. The process must be stopped when the curve of the target material starts dropping, meaning that all the monitored element has been etched, while that of the underlying materials starts increasing.
Different etching tests have been performed to investigate the quality of the obtained films, and to extract some useful parameters concerning the peculiar treatment of PCMs.

3.5.1 First test

The first attempt has been carried out with the idea of performing a comparison between GeTe and GST on two identically processed wafers, obtaining the first values to derive their etch rate. The procedure was facilitated by the fact that, adopting the most common choice for the resist, i.e. M108Y with BARC, the optimal exposure parameters had been already extracted in previous trials. Therefore, after the deposition of around 50 nm of PCM and 10 nm of oxide, both wafers have been exposed with fixed d-f values of 29-0, without the need of parametric variations.
After a rapid check of the correct outcome of photolithography, the critical point remained the BARC opening in regions where the resist had been patterned. Indeed, BARC is not affected by development, and its removal could not be performed using IBE in the same step to etch the PCM underneath. In consequence, this procedure was performed with a dedicated recipe in the SPTS Advanced Plasma System (APS) module, a dry etcher usually employed to pattern silicon oxide and silicon nitride. An SEM observation of the opened BARC are shown in Fig. 3.17(a). The darker layer between resist and PCM corresponds to the BARC residual portion protected from the etchant by the PR during the procedure.
At this point, the PCM layer was finally exposed, and ready to be processed in the IBE. Fig. 3.17(b) presents the result of this step, result obtained in both wafers regardless of the nature of the etched PCM. A tilt angle of -10° was applied, since it was suggested as the most suitable choice to correctly etch the corners of each feature, producing a correctly flat surface.

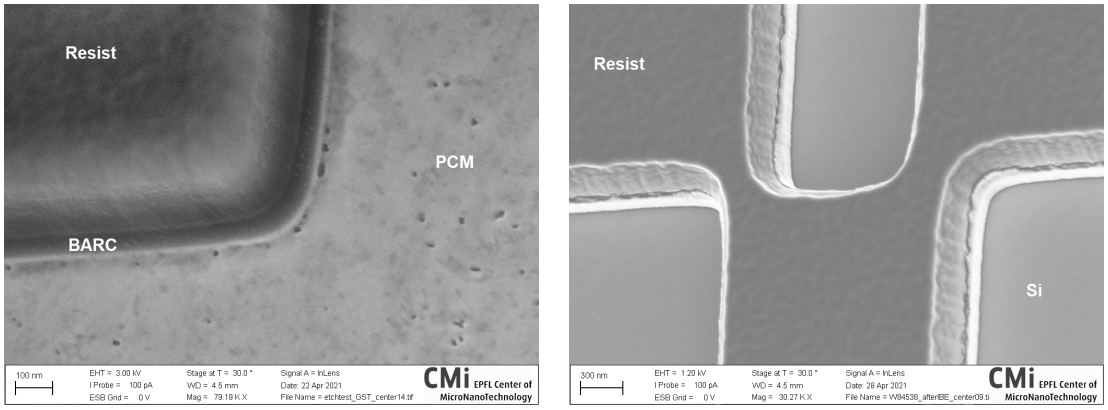

(a) *Wafer surface after BARC opening* **(b)** *Wafer surface after IBE*

Figure 3.17: Results of the BARC opening (left) and the IBE (right) steps.

In the right picture, it can be noticed that at the bottom of the sidewalls an additional layer is present. With high probability, the latter was formed by the etched material, suddenly redeposited before being removed. This phenomenon

could be avoided performing a resist reflow, a procedure that modifies the sidewalls to obtain a positive slope, as the one presented in Fig. 3.10(b). In this way, much less material is going to redeposit.
Unfortunately, an unpredicted issue was encountered during this last procedure, even if it has been performed together with a member of the CMI staff, interested in the outcome of the process for new materials. Indeed, the suggested recipe to etch the materials set a medium voltage to accelerate the beam, expecting the process to last few minutes. However, the curves (on the end-point screen) related to the elements composing the PCMs suddenly dropped down, meaning that the layers had been totally etched in few seconds. In consequence, the process continued on the bare Si substrate, overetching it, something that must be avoided in a future complete process flow, since the silicon thickness will be, in that case, a critical parameter affecting the modes of the waveguides (see Sec. 2.2.1).
A check of the amount of removed Si has been performed after the conclusive resist removal, a procedure that employs a flow of oxygen plasma for few minutes. The final results of the whole process are shown in Fig. 3.18.

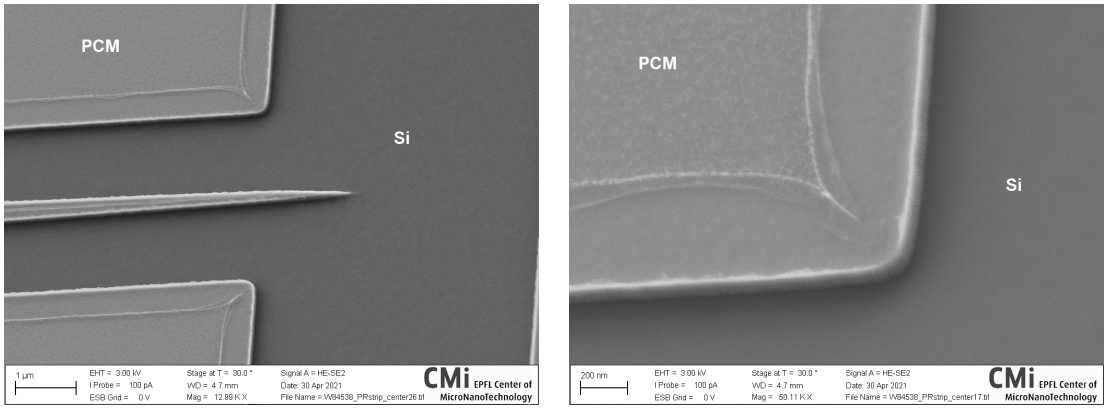

(a) *Test structures: adiabatic coupler, GeTe* **(b)** *Test structures: metal pad, GST*

Figure 3.18: Results of the first etching test for both the processed wafers.

First of all, it can be noticed that the quality of the obtained layers is totally comparable in both wafers, meaning that the procedure can provide the same outcome for GeTe or GST. However, the film uniformity is not as good as the one obtained in the lift-off tests: on one side, some unusual (but equal in each feature) lines are present on top of the layer, surely some artifacts caused either by the resist or by the BARC; on the other, some portions of redeposited material are present on the sidewalls, as expected from the previous observation.
In order to quantify the Si overetch, a conclusive surface analysis was performed on both wafers with the mechanical profilometer. Instead of the expected 60 nm

in total, the measured step was in both cases around 90 nm, meaning that 30 nm of silicon had been removed. A possible explanation for the very quick etching of the PCM layer is that the BARC opening process was performed for too long, with a consequent removal of a portion of the materials underneath. Moreover, the use of a medium-intensity ion beam surely worsened the situation, preventing the precise detection of the end point. In consequence, an additional test was necessary to understand if the presence of BARC was strictly required, or if similar results could have been obtained avoiding it, this time also employing a lower acceleration voltage for the beam for a better control over the etching time.

3.5.2 Second test

As anticipated above, a second attempt was performed coating a wafer with resist M108Y, but without BARC. In this case, as it was for lift-off, the optimal exposure parameters were unknown, therefore a d-f matrix was applied, with a central 30-0 combination and variations of 5 and 0.2 respectively.
Since no BARC opening was necessary this time, the wafer has been right away processed in the IBE, but using a low-voltage recipe, with the idea of stopping the process right at the interface with the substrate. Nevertheless, once again an issue occurred during the procedure: the curves for the concentration of four different elements (Ti, Ge, Te and Si) were monitored in the same plot, but the one related to Ti reached values more than one order of magnitude higher than the others. Therefore, the exact point in which the silicon curve started increasing was not correctly detected, resulting again in a slight overetch. The process was anyway stopped after around 2 minutes. Additional 10 seconds were added at the end to check the status of the wafer, confirming that in this case only Si was being etched. The final results, after the resist removal, are shown in Fig. 3.19.

Despite a different color of the pictures, only due to a different set up of the SEM parameters, the obtained features are completely equivalent to those presented in Fig. 3.18. This outcome proves that BARC is not strictly necessary for this kind of procedure and, as a consequence, for successive analysis it will be avoided, increasing the possibilities to correctly detect the substrate surface at the end of the etch step.
Similarly to what happened during the lift-off tests, better features on the wafer were obtained for zero focus and doses slightly lower than the one applied in the center. A definitive study in this regards could be performed with a narrow d-f matrix around the values of 25-0 for a more precise inspection of these parameters.

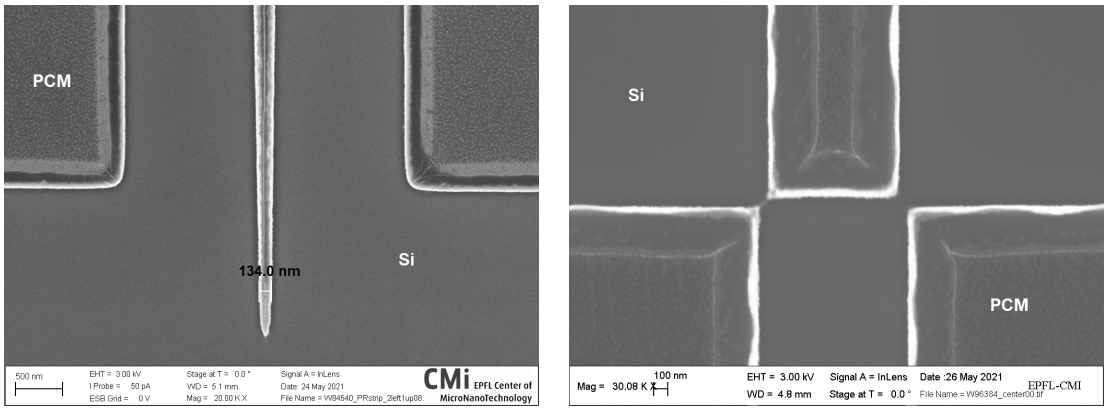

(a) *Test structures: adiabatic coupler* **(b)** *Test structures: bars*

Figure 3.19: Results of the second etching test.

3.5.3 Etch rate extraction

Once the prove that a good result could have been obtained in an etching process without the use of a BARC, the last step of this analysis concerned the extraction of the etch rate for the two involved PCMs.
For this purpose, five different wafers have been prepared, depositing on all of them around 100 nm of PCM and 8.5 nm of TiO_2, employing GST on four and GeTe on the last one, in order to extract sufficient information on both. On all of them, the same lithography step has been performed, applying constant exposure parameters fixed at 25-0. Subsequently, the samples have been processed in the IBE for different defined times, ranging between one and two minutes, and, at the end, the resist was removed from all of them. The result of this process is a set of wafers processed exactly in the same way, except for a variable exposure to the ion bombardment. Therefore, a final inspection with the mechanical profilometer allowed the extraction of the total thickness of the portions removed from the surface. The successive analysis on the measurements is shown in Fig. 3.20.

The procedure consisted in fitting the four values related to the samples with GST, and obtaining a line whose starting point is at a value around 49 s. This constant offset can be attributed to the removal of the top oxide layer. Its etch rate can be in consequence computed dividing its thickness by the required time, obtaining a value of around 0.17 nm/s. Assuming the same shift also for a wafer with GeTe, the last sample alone was sufficient to obtain a representative line also for this second material. The slope of the curves can, finally, provide information on the etch rate of the materials.
In conclusion, the extracted etch rates of GST and GeTe, processed in IBE with a low-power recipe at an angle of -10°, are, respectively, 2.1 nm/s and 2.4 nm/s.

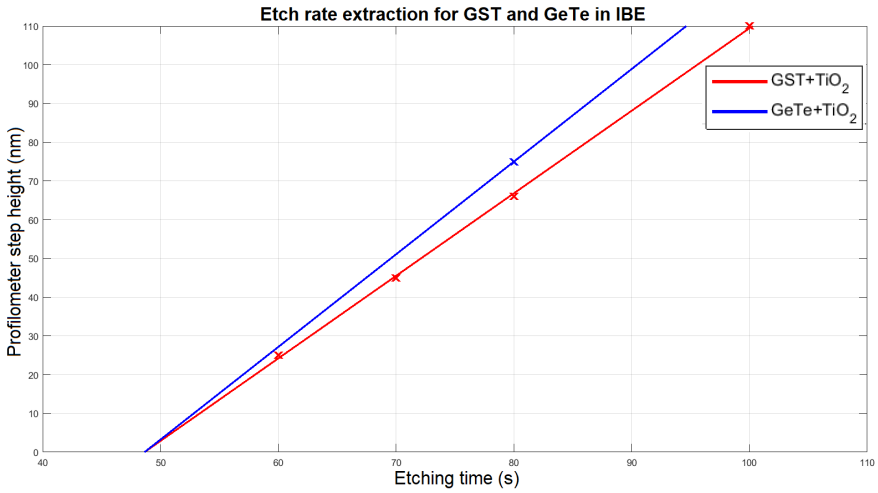

Figure 3.20: Data analysis for the extraction of the PCMs etch rate.

3.6 Lift-off and etching for PCMs: summary

The analysis of the integration of PCMs in silicon PICs, performed in the cleanroom environment of CMI at EPFL with the idea of including their treatment into standard processes, has produced highly promising results. Indeed, it has been demonstrated that the patterning of this kind of materials can be efficiently obtained through DUV lithography, a technique that, thanks to its high throughput, can enable a large-scale production of the involved devices. Dimensions in the order of few hundreds of nanometers have been obtained with both the approaches selected for this procedure, i.e. lift-off and etching, always respecting the constraints in terms of resolution imposed by the lithography step to around 150 nm. Tab. 3.2 presents a comparison between the results obtained with these techniques.

	Lift-off	**Etching**
Resist	M108Y NO BARC M35G NO BARC	M108Y NO BARC
Exposure parameters	Dose 40-45, focus 0 Dose 20-30, focus 0	Dose 20-30, focus 0
Additional procedures	Descum: 20 s, 200 W Sonicator: 2 min	IBE: low power recipe

Table 3.2: Comparison between the results of the fabrication tests performed on PCMs employing lift-off and etching.

In addition to what is included in the table, lift-off presents the advantage to avoid the risk of damaging the substrate, which is not affected by the procedure, and the produced films present very high quality and a smooth surface. However, the immersion in the remover takes around 7 days, and some residuals of the resist can be still present at the end. A possible solution would be to employ an additional step in the sonicator before removing the wafer from the solution, but only fr a limited time, in order not to cause the detachment of some features.
On the other hand, performing etching high attention must be paid to correctly detect the end-point of the process, reducing as much as possible the substrate overetch. Moreover, the quality of the obtained film is not as goo as in the previous case. However, with this technique the procedure is much faster than for lift-off, therefore enabling a faster production.
The analysis must be completed by performing conclusive tests to extract the precise exposure parameters, which can be ultimately determined only employing dedicated masks, with definitive layouts as the ones that will be presented in the remaining chapters.

Chapter 4

Design and Simulation of reconfigurable optics

After the accurate inspection of PCMs from the fabrication point of view, the results coming from the characterization process, and the limitations in terms of features dimensions have been then employed in the analysis of the integration of this kind of materials in components for silicon PICs. In particular, on one side, the simulation of reconfigurable couplers and phase shifters has been carried out using the values of the optical parameters extracted both from literature and from the study made at the beginning of this project, while, on the other, the design of the optimal geometries has been performed coping with the constraints imposed by the selected fabrication techniques.
Concerning the PCMs optical parameters, the simulations have been run with values suggested in literature, expecting only negligible variations with respect to the real ones extracted through ellipsometric measurements. The most important aspect was, indeed, to set up the simulation environment, and to understand how to provide reasonable results, even with test parameters. In principle, if significant deviations upon material characterization were detected, the computation would be performed again making the appropriate corrections, but the models are already built, and this process only would require a quite moderate effort.
In this chapter, the results of the simulation and design process are outlined. Preliminary 2D models have been used to extract the optimal geometric parameters of the section of the components. The latter have later been employed to generate more complex 3D structures, for a more accurate analysis of the final devices.
Optical simulations have been carried out exploiting the potential of the Wave Optics Module provided by Comsol Multiphysics®, while the analysis of the obtained results was subsequently performed with MATLAB®.

4.1 Wave Optics Module: 2D and 3D models

The Wave Optics Module is a peculiar package provided by Comsol Multiphysics to extend its functionalities for the resolution of problems in the electromagnetic waves field for frequencies commonly applied in optical telecommunications [53]. This module is, therefore, particularly suitable for simulating optical components like fibers, waveguides, lasers and active devices, both in 2D and 3D geometries. However, 3D simulations are usually avoided in the early stages of a design process, due to their complexity and computational cost. In consequence, the main approach, consists in employing 2D models to extract all the available information about the geometry and the behaviour of the electromagnetic waves in the structure, using 3D computations only at the very end to confirm the results of the preliminary analysis.

The starting point to build a complete model is, therefore, a 2D study called modal analysis, which, given the geometry of the section of a waveguide, allows the extraction of the effective index and field distribution associated to each mode (see Sec. 2.2.1) propagated in such a structure.
Among the physical interfaces present in the Wave Optics Module, the most useful one to perform modal analyses is the Electromagnetic Waves, Frequency Domain Interface, which allows various types of studies both in frequency or wavelength domains. The governing equation solved in this kind of study is a general expression of the wave equation written as

$$\nabla \times \mu_r^{-1}(\nabla \times \mathbf{E}) - k_0^2 \left(\epsilon_r - \frac{j\sigma}{\omega\epsilon_0}\right)\mathbf{E} = 0 \tag{4.1}$$

in which μ_r is the relative permeability, ϵ_r is the relative permittivity, σ the electrical conductivity, ϵ_0 the vacuum permittivity, and k_0 is the wave number of free space, all parameters that vary depending on the domain in which the problem is solved, while ω is the frequency. This equation is used for the electric field in a 3D space, but with a 2D geometry, for the cross-section of a waveguide oriented along the z axis, the field is expressed exactly as in Eq. 2.1. Therefore, Eq. 4.1 can be simplified into Eq. 2.2, and the solver performs the 2D mode analysis.
On the other hand, 3D simulations are computed with the Beam Envelopes Interface, mainly used in systems where the field amplitude varies slowly on a wavelength scale. In this case, a Boundary Mode Analysis is performed similarly as before to compute the modes in the initial and final sections of the 3D structure. Then, the result is employed in a Frequency Analysis to study their uni- or bidirectional evolution in the system. In the first case, relevant for the scope of this project, the equation to be solved is always Eq. 4.1, but the field is expressed as

$$\mathbf{E}(\mathbf{r}) = \mathbf{E_1}(\mathbf{r}) \cdot e^{-j\phi_1(\mathbf{r})} \tag{4.2}$$

as the product between the electric field envelope $\mathbf{E_1}$ (the final unknown) and the phase function $\phi_1(\mathbf{r}) = \mathbf{k_1} \cdot \mathbf{r}$ (where $\mathbf{k_1}$ is the wave vector), both with a more complex 3D dependence that makes the problem more complicate.
However, Eq. 4.1 alone is not sufficient when multiple domains are included. Indeed, each material presents its own parameters, leading to discontinuities at the interfaces. Therefore, to ensure the continuity of the electromagnetic field, additional boundary conditions are necessary. Their most general formulation concerning the electric field can be written as

$$\mathbf{n_2} \times (\mathbf{E_1} - \mathbf{E_2}) = 0 \tag{4.3}$$

where $\mathbf{E_1}$ and $\mathbf{E_2}$ are the field in the two domains, and n_2 the curl of the contact surface. Similar equations can be written for the magnetic field.
While this equation is easily applicable for the internal boundaries, a different treatment is required for the extremes of the geometry. Both the described interfaces provide a quite various range of external boundary conditions. Among them, some of the most employed are the Perfect Electric Conductor, to simulate metallic surfaces or symmetric domains, the Perfectly Matched Layer, to absorb all the incoming radiation with small reflections, and the Impedance Boundary Condition, for domains in which the field is known to penetrate for a short distance. Although this choice can usually affect the simulation result, in optical waveguides the field is so confined in the core region that, if the geometry is truncated sufficiently far (in the order of some multiple of the wavelength), the boundary condition only produces negligible effects. In this project the Impedance Boundary Condition has been applied, assuming a very low field at the edges of the model.

Once the geometry of the problem is set, and the behaviour of the field at the boundaries is specified, combining Eq. 4.1 and 4.3 the solver has all the necessary elements to conclude the analysis, for which the Finite Element Method (FEM) is applied: each domain is divided into much smaller elements of a fixed shape, generally squared or triangular in 2D, cubic of tetrahedral in 3D, and the solution is approximated on each of these portions using a constant, linear or higher order elementary shape function. The resulting geometrical division is called mesh. The latter can be created by the solver itself, following the specifications of the physics of the problem, or, on the other hand, defined by the user if the automatic one seems not accurate enough, with the possibility to finely tune each characteristic of the geometrical division.
All these aspects of the Wave Optics Modules have been analyzed and adapted in all the 2D simulations and design of the target optical components. The motivation behind the creation of each 2D model and their respective results are now outlined.

4.2 Adiabatic coupler design: 2D analysis

The first design and simulation process was performed to study the integration of PCMs in reconfigurable optical switches. As anticipated in Sec. 2.2.5, these elements are active components employed in PICs to selectively deviate the path of the propagating signal, allowing an efficient on-chip data transmission. The main aim of this analysis is to design a non-volatile, low power consumption alternative solution to existing thermo-optical, opto-electric or MEMS-based switches.
Many of the just mentioned switching architectures rely on directional couplers (see Sec. 2.2.2) to transfer the light to alternative optical paths. However, these elements are limited in terms of bandwidth, and therefore their correct operation can be compromise by variations in the signal wavelength. In consequence, adiabatic couplers can be more suitable for this kind of applications, since their bandwidth is expected to be much wider (see Sec. 2.2.3). For this reason, a detailed design procedure to extract all the optimal geometrical parameters for this optical component has been performed. In order to achieve this final goal, also the parameters of the directional coupler has been determined. Fig. 4.1 presents a schematic of these elements, with a detail on the involved parameters.

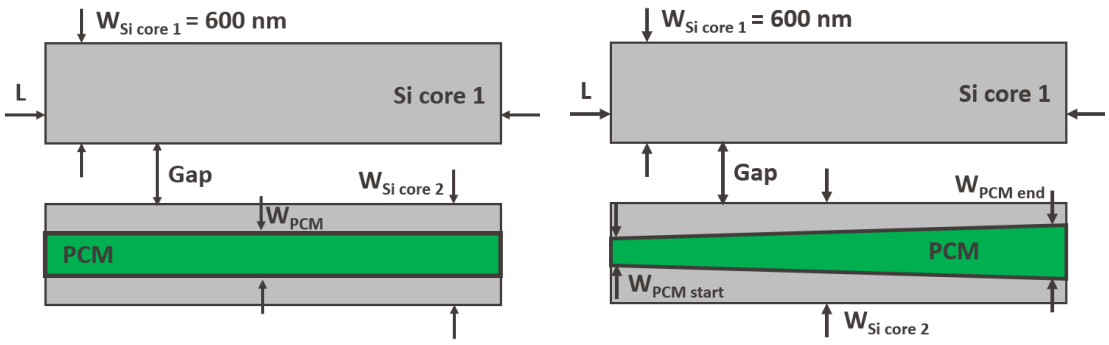

(a) *Directional coupler, constant PCM width* **(b)** *Adiabatic coupler, variable PCM width*

Figure 4.1: Schematic of the top view of a directional coupler (left) and of an hybrid adiabatic coupler (right) with PCM deposited on top of one of the Si cores.

The design procedure has been then adapted to the extraction of its geometric parameters: first, the waveguides forming the directional coupler were simulated singularly, determining the optimal parameters to fulfill the coupling condition between them; then, the adiabatic coupler has been obtained by varying the width of the PCM, obtaining a gradual increase between its initial and final portions. In this last configuration, the coupling condition is fulfilled only in the point in which the PCM width is equal to that of the directional coupler.

4.2.1 Silicon rib waveguide

The first step for the design of the adiabatic coupler consists in the analysis of a single silicon rib waveguide, which represents one of the two branches of the coupler. The aim of this first simulation was to understand how the field behaves in such a structure, and to extract the effective index of its fundamental mode. In order for the coupling to happen, the latter is the value that must be subsequently matched in the second waveguide.
The creation of the model started with the definition of the geometry. Besides the total thickness of the Si portion, which was fixed a priori to 220 nm, under the assumption of working on a SOI wafer, the other parameters have been chosen according to common practices in currents PICs: the width and the thickness of the core have been set to 600 nm and 60 nm respectively. Therefore, the resulting thickness of the slab was set to 160 nm, and its width to around 2 μm to obtain sufficiently large lateral wings. Two additional portions of air and SiO_2 completed the structure, creating a domain large enough to truncate the surface far from the central waveguide.
At this point, the Impedance Boundary Condition was applied to the external edges of the geometry, and a triangular user-defined mesh was selected, in order to obtain a finer partition of the most critical domains. The obtained partition and the results of the subsequent simulation are shown in Fig. 4.2.

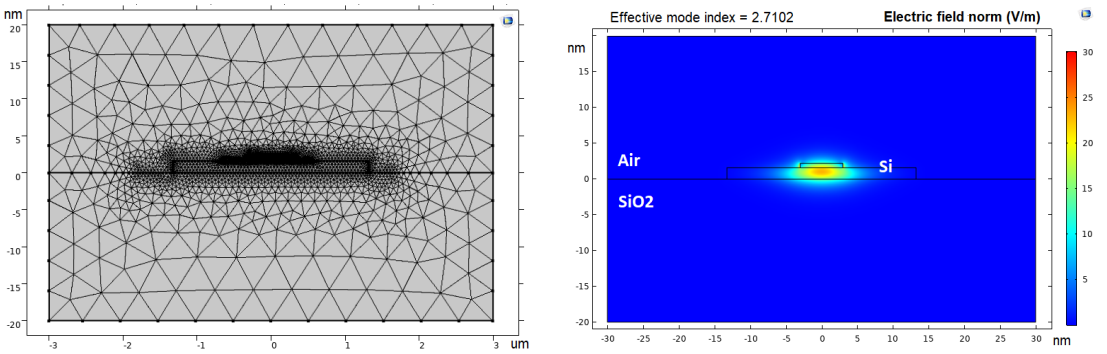

(a) *Geometry and mesh* **(b)** *Electric field, fundamental mode*

Figure 4.2: Geometry (left) and electric field norm of the fundamental mode (right) of a silicon rib waveguide.

It can be observed in Fig. 4.2(a) that the mesh is highly defined around the waveguide, while it is quite coarse going towards the edges. This configuration is justified by the fact that the field in those portions is expected to be almost zero. The hypothesis is confirmed by the result in Fig. 4.2(b), which presents the fundamental mode of the waveguide, the one with the highest effective index:

the electric field is completely confined in the silicon portion, and decays almost immediately to zero outside, meaning that the confinement is high. The effective index of the mode is around 2.71.
The outcome of this simulation also showed that, besides the fundamental mode in which we are interested, higher order modes are propagated in such a structure. However, the latter are mainly confined in the lateral wings and, in addition, present quite different effective indices (all lower than 2.52, the value of the second propagated mode). In consequence, they should only slightly interact with the central portion of the waveguide, causing a negligible effect if only the fundamental mode is excited by the field.
After having confirmed that the structure can provide a strong confinement, the last analysis in this model required a parametric variation (called "sweep" in this context) of the only hanging parameter, i.e. the width of the waveguide base, which undoubtedly affects the field in the central region. The idea is to obtain the value beyond which the effective index of the fundamental mode saturates, meaning that from that point it is no more influenced by the dimension of the wings. The outcome of this evaluation is showed in Fig. 4.3.

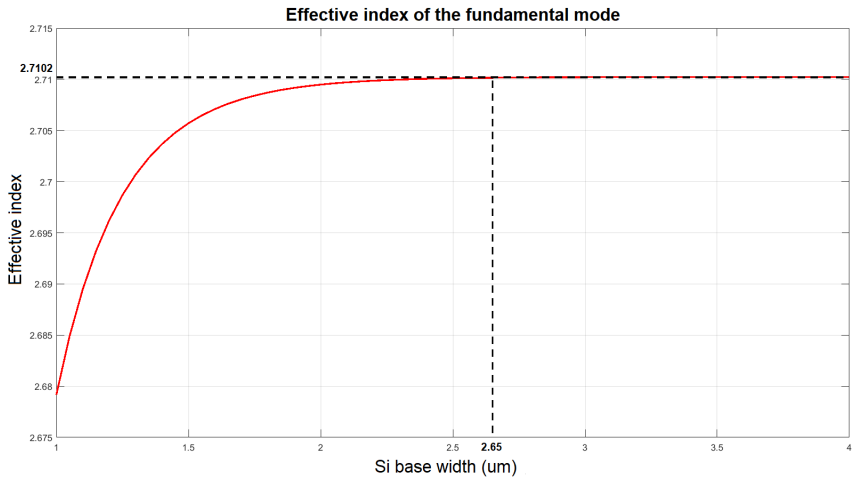

Figure 4.3: Variation of the effective index of the fundamental mode in the silicon rib waveguide with respect to the width of the Si base portion.

It can be observed that the effective mode index increases together with the width of the base up to the saturation value of 2.7102, obtained in correspondence of a width of 2.65 μm. Therefore, as long as the wings are large enough to satisfy this lower bound, their width can be modified to include the metallic contacts without affecting the fundamental mode.

4.2.2 Silicon rib waveguide with PCM on top

The second step of the design process is the analysis of the other, single waveguide which completes the adiabatic coupler. In this case, the PCM is deposited on top of the silicon core. The purpose of this study was the extraction of the optimal geometrical parameters of the Si-PCM hybrid rib waveguide to match the same effective index of the case with Si alone. This matching condition must be fulfilled to enable the power transfer in the directional coupler.
The geometry of the model has been defined exactly as in the previous simulation, with the only exception of the additional PCM layer (over the Si core) covered by 10 nm of TiO_2 to avoid its spontaneous oxidation (see Sec. 2.3). However, this time too many degrees of freedom were present in the design of the geometrical parameters of the system, since the PCM thickness and width, and the widths of both the Si core and base were all quantities to be determined. Therefore, some preliminary relations have been established: the width of the base has been fixed to 2.65 μm, the saturation value obtained from the previous model, and the width of the PCM has been set to be always 200 nm narrower than that of the Si core. This last condition is reasonable considering that the effective index matching should happen in the middle of the adiabatic coupler. In this way, enough margin is left to design its initial (smaller) and final (larger) portions, which respectively should not go much lower than 150 nm, to comply with the fabrication limits, and cannot exceed the dimension of the Si core. In conclusion, only the PCM thickness and the core width remained the floating parameters to be analyzed.
Similarly as before, Impedance Boundary Conditions have been applied at the edges of the geometry, and a user-defined triangular mesh was created. The only additional challenge was the definition of the optical properties of the involved PCMs, not included in the Comsol library. n and k of both materials have been extracted from [14]. In particular, the complex refractive index of GeTe was set to 3.95+0.1i for the amorphous state, and to 6.60+0.43i in the crystalline one, while for GST the same quantities are 4.30+0.1i and 7.45+1.8i, respectively.
At this point, the simulation was ready to be performed, including parametric sweeps over the PCM thickness (limited between 10 nm and 50 nm, to minimize the losses), the Si core width and the state of both PCMs. As an example of the obtained results, the fundamental modes of the waveguide with GeTe in amorphous and crystalline states are shown in Fig. 4.4.

Similarly as the case of the single silicon waveguide, the field is well confined in the center of the waveguide. However, the effect of actuation can be clearly seen comparing the two pictures: with the PCM in the amorphous state, the mode propagates mainly in silicon, with a lower effective index; on the other side, with the same geometry, but the crystalline structure, the mode is shifted towards the PCM layer, with a higher effective index. It can be also noticed that, as a consequence

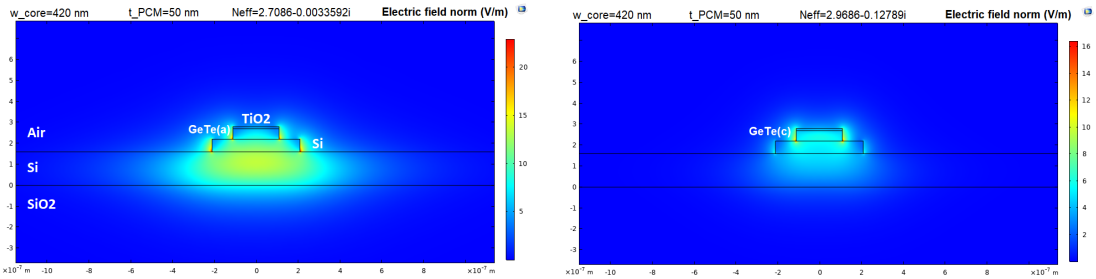

(a) *GeTe in amorphous state* **(b)** *GeTe in crystalline state*

Figure 4.4: Fundamental mode is Si-PCM hybrid rib waveguide with 50 nm of GeTe in amorphous (left) and crystalline (right) states, and core width of 420 nm.

of the relatively high extinction coefficient of the PCM, the mode presents in both cases a non-negligible imaginary part in the effective index. The latter is linked to absorption in the structure and, therefore, a consistent attenuation of the signal is expected, especially with the PCM in its crystalline state.
Nevertheless, this significant change in the real part of the effective index is the fundamental property for which PCMs have been analyzed in this context. Indeed, concerning the adiabatic coupler, the consequence is that, maintaining the exact same geometry, the coupling condition is not fulfilled in both cases. Therefore, the PCM actuation is sufficient to change between the ON/OFF state of the switch. The effect of the actuation, in the case of GeTe and for some selected thicknesses, is shown in Fig. 4.5.

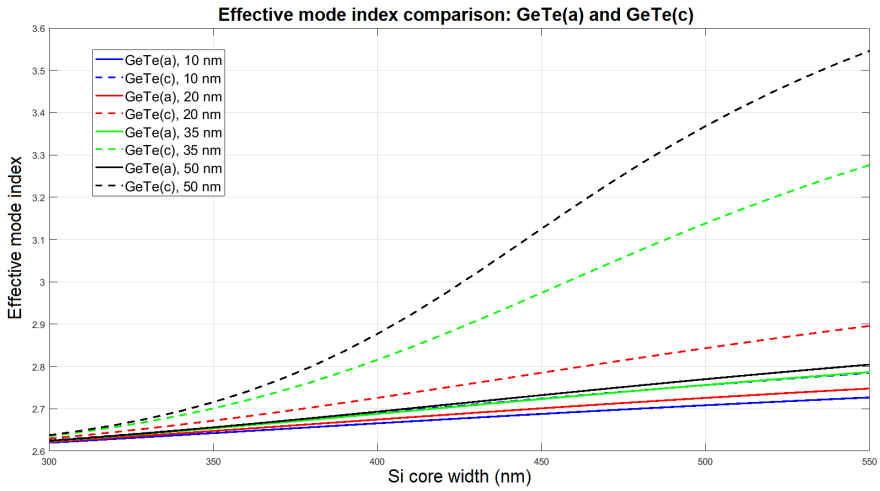

Figure 4.5: Variation of the effective index of the fundamental mode versus core width, for GeTe amorphous and crystalline at different thicknesses.

On the one hand, it can be noticed that, for each state or thickness of the material, the effective mode index always increases for a larger core (and so, for a larger PCM). On the other hand, the difference between the amorphous and crystalline curves is more pronounced for a thicker layer. Therefore, in principle, a thicker PCM should allow a better separation between the ON and OFF state of the switch, even if it would also produce higher losses.
The values of the effective index of the fundamental mode, for each combination of PCM thickness and core width, and for the two materials in both states, have been then extracted and analyzed with the idea of finding the best combinations to match the index of the Si waveguide. The procedure for the extraction of the optimal core width (and, in consequence, the optimal PCM width) in the case of amorphous GeTe is presented in Fig. 4.6.

For each of the nine curves, relative to different thicknesses between 10 and 50 nm, the optimal core width is the value for which the effective index is equal to 2.71. For the sake of simplicity and to speed up the computation, starting from this point only four relevant thicknesses (10, 20, 35 and 50 nm) have been analyzed. The same study has been performed for both materials and both states, obtaining in each case a similar trend. The extracted values of the optimal core widths are presented in Table 4.1.

PCM	**State**	W_{core} **(nm)** t = 10 nm	W_{core} **(nm)** 20 nm	W_{core} **(nm)** 35 nm	W_{core} **(nm)** 50 nm
GeTe	a	505	468	438	422
GeTe	c	430	385	360	350
GST	a	495	455	423	407
GST	c	420	383	367	360

Table 4.1: Optimal Si core widths for different PCM types, states and thicknesses.

It can be observed that the results are totally analogous for the two materials, with limited variations due to their different optical parameters. In each case, in order to obtain a constant effective index, a larger width compensates either a smaller thickness, or a reduction in the refractive index of the material, leading therefore to higher values in the amorphous state.
Up to this point, in principle, either of the PCM states could have been associated to the ON state of the switch. Indeed, it was not specified if the coupling should happen with the amorphous or crystalline PCM, as long as the phase matching condition is fulfilled for only one of the two states. Based on this choice two main design approaches could have been followed: since only when the switch is active the signal actually propagates in the waveguide with the PCM, and because of the

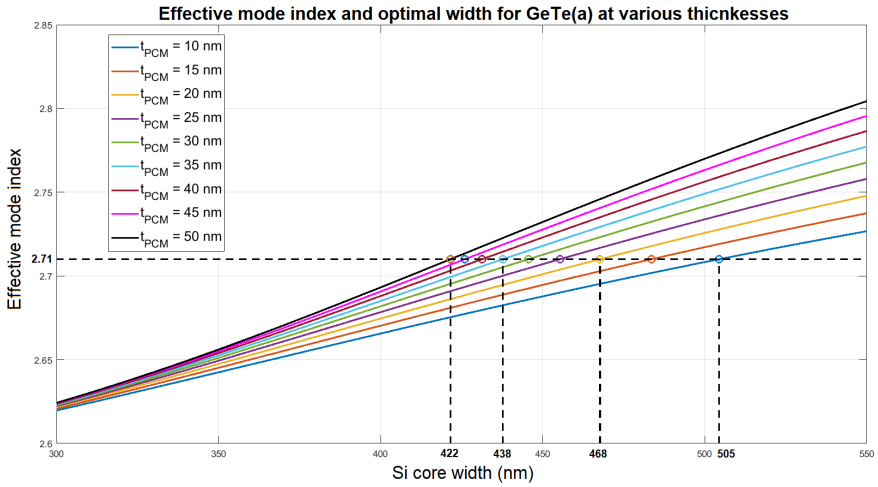

(a) *Amorphous GeTe*

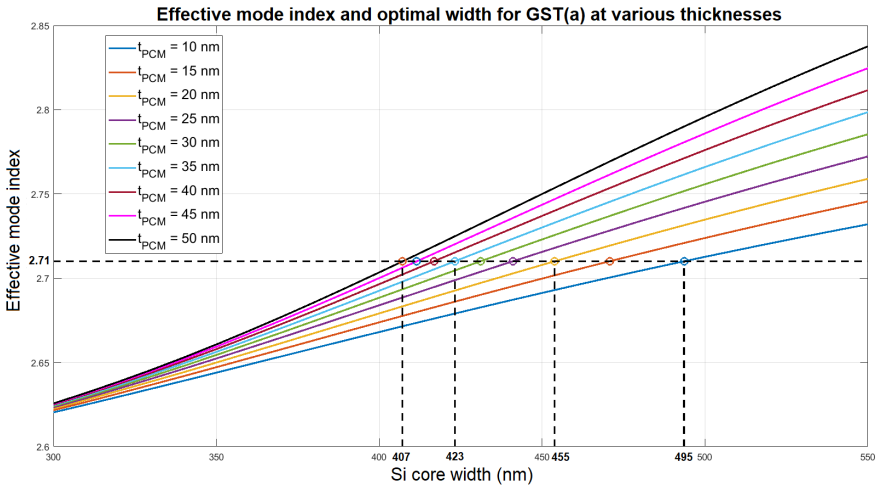

(b) *Amorphous GST*

Figure 4.6: Optimal core widths for GeTe and GST at four relevant thicknesses.

higher losses expected in the crystalline case, a geometry that allows the coupling with the amorphous material would result in a lower attenuation in the ON state. However, the PCM could affect the signal also when the switch is OFF, and the material in its crystalline form would increase the losses. The outcome is, therefore, a less-lossy ON state and a more-lossy OFF state. The opposite result is obtained designing the structure to match the coupling condition with a crystalline PCM. A complete analysis to extract the optimal configuration would have required the design of both these geometries, for both materials, and a final comparison in terms of performances, especially concerning scalability. However, comparing the optimal

core width values, it can be observed that the crystalline case could have led to more challenging structures from the fabrication point of view. Indeed, recalling that the PCM width was fixed to be 200 nm narrower than that of the core, the dimension associated to this PCM state are (with the single exception of the lowest thickness) around the resolution limit of DUV lithography for this central section of the coupler. Therefore, to fabricate its initial, smaller portion, EBL would be required. In conclusion, the analysis has been carried out only targeting geometries suitable for a switch active in the amorphous state.

4.2.3 Symmetric Coupler

The successive step consisted in the combination of the previous models to obtain a symmetric coupler, the central section of the future adiabatic coupler where the signal is transferred for an active switch, i.e. when the PCM is amorphous. The aim of this analysis was in first place to prove the correctness of the previous results, checking if the the electric field is correctly shared between the waveguides in the ON state, and well separated after the actuation. Moreover, both the losses caused by the PCM and the coupling length have been extracted, the latter lately used as a starting parameter for the length of the 3D model.
The structure has been created adding to the same silicon base both the cores of the previously analyzed waveguides. While the other dimensions had been already fixed, this time the gap between the waveguides represented another degree of freedom in the design. Therefore, the parametric sweep has been performed on both the PCM thickness and the middle separation. The result for amorphous GST, with a thickness of 50 nm (and the associated optimal width previously extracted) and a gap of 200 nm is shown in Fig. 4.7, where the characteristics of the two fundamental supermodes (see Sec. 2.2.2) are presented.

In particular, on the left the symmetric supermode is shown: it can be observed (on top) that its distribution is completely shared between the waveguides, with an effective index around 2.74, slightly above the one of the single waveguides alone. Moreover, its phase is constant along the whole surface (down). On the other side, the antisymmetric mode is also correctly distributed in both elements with an effective index around 2.67, but as expected, this time its imaginary part changes from negative to positive from the left to the right waveguide, with a zero point in the middle. The same trend is followed by the associated phase, which abruptly changes sign in the central section. We can conclude that the coupling condition is fulfilled, as expected from previous simulations.
The last aspect to be analyzed how the modes change after the actuation, i.e. when the PCM is in its crystalline form. Always considering the same geometry, the result with crystalline GST is shown in Fig. 4.8.

It can be immediately noticed that both modes are confined only one of the

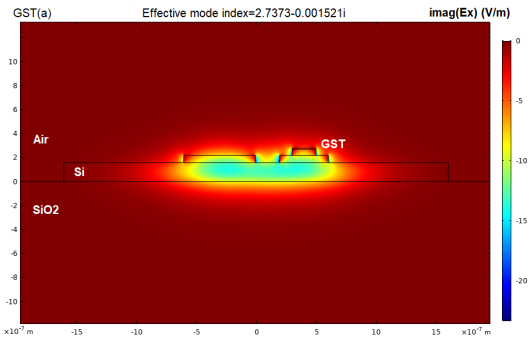

(a) *Symmetric supermode, imag part*

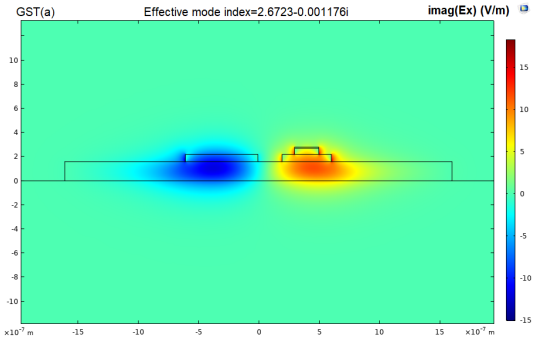

(b) *Antisymmetric supermode, imag part*

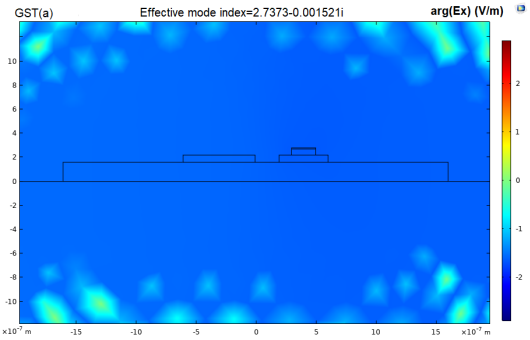

(c) *Symmetric supermode, phase*

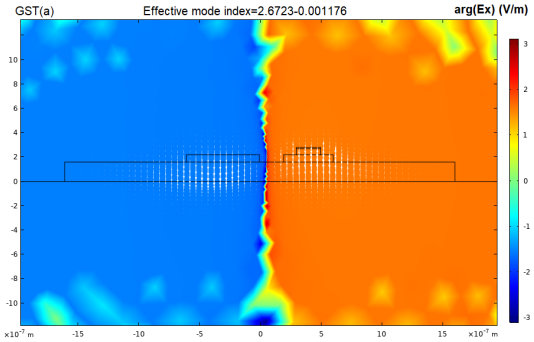

(d) *Antisymmetric supermode, phase*

Figure 4.7: Imaginary part (top) and phase (down) of the TE symmetric (left) and antisymmetric (right) modes of the 2D coupler, with amorphous GST of thickness 50 nm and a middle gap of 200 nm.

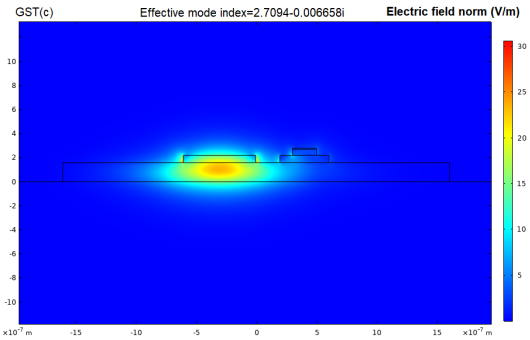

(a) *Symmetric supermode, norm*

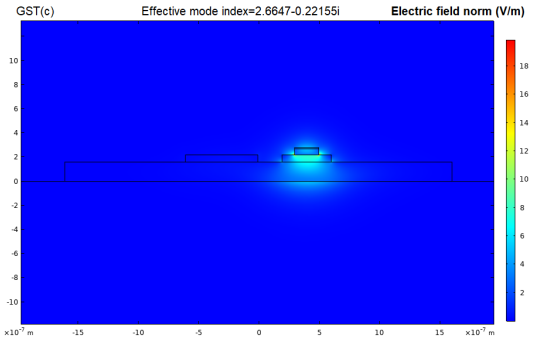

(b) *Antisymmetric supermode, modulus*

Figure 4.8: Norm of the TE symmetric (left) and antisymmetric (right) modes of the 2D coupler, with 50 nm of crystalline GST and a middle gap of 200 nm.

waveguides: the coupling condition is properly broken. Moreover, the index of the first mode (left) is around 2.71, a value that is highly promising. Indeed, in this configuration, which corresponds to an OFF switch, the signal should remain in the Si waveguide on the left, and the right portion should not interfere with its propagation. Therefore, as correctly obtained, its index should remain the same of the single Si rib waveguide, as if the second waveguide were not present. In conclusion, the overall working principle of the coupler has been correctly proven, confirming the expectations of the preliminary analyses.
The final ingredient to complete the model was the estimation of the coupling length and the losses related to each parametric variation. The first quantity has been computed with Eq. 2.4, using the effective indices of the two fundamental modes of the structure. The second one was calculated with Eq. B.3, starting from the imaginary part of the effective index. The results for both materials and for some relevant geometries are shown in Table 4.2.

PCM	**Gap (nm)**	$\mathbf{t}_{PCM}$ **(nm)**	$\mathbf{W}_{core}$ **(nm)**	$\mathbf{L}_C$ **(μ m)**	**Losses (dB)**
GeTe	200	20	468	12.8	0.45
GeTe	200	50	422	12.2	0.73
GeTe	300	20	468	18.3	0.65
GeTe	300	50	422	17.4	1.1
GST	200	20	455	12.6	0.44
GST	200	50	407	11.9	0.76
GST	300	20	455	18.0	0.63
GST	300	50	407	17.0	0.96

Table 4.2: Estimated values of coupling length and losses of the 2D coupler, for GeTe(a) and GST(a) and for different combinations of gap and thickness.

It can be observed that the same trend is followed by both PCMs, which present very similar values: a larger gap causes a significant increase of both coupling length and losses, while a higher thickness reduces the former, but increases the latter. In any case, the effect on the field attenuation is comparable to the one caused by scattering in a waveguide (see Sec. 2.2.1), or even larger, becoming in consequence the dominant contribution. However, these were only estimated quantities, a definitive confirmation required the successive 3D analysis.

4.2.4 Adiabatic Coupler

After the analysis of the central section of the adiabatic coupler, the successive step consisted in the study on its initial and final portions, to predict its best

geometrical parameters. The main idea was to find the optimal PCM widths to break the coupling condition (see Sec. 2.2.3) fulfilled in the middle, obtaining a good separation of the modes between the two waveguides.
Therefore, the simulation has been performed using the same model of the 2D coupler, computing for both PCMs a parametric sweep over their width. An example of the final section of the adiabatic coupler, with amorphous GeTe for a thickness of 50 nm and a width of 400 nm (much larger than 222 nm, the optimal value in the center of the structure), is shown in Fig. 4.9.

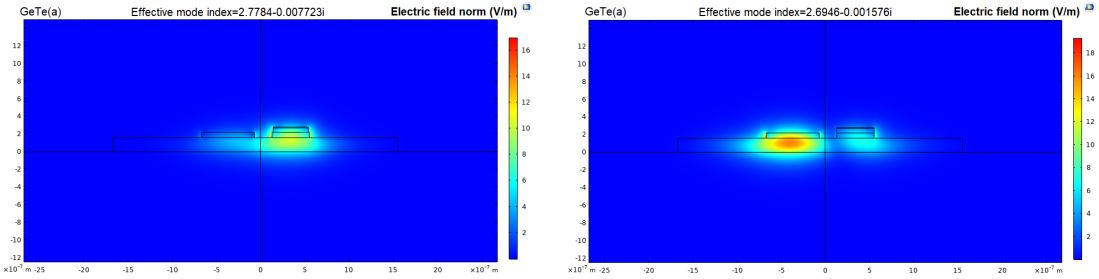

(a) *Symmetric supermode, norm* **(b)** *Antisymmetric supermode, modulus*

Figure 4.9: Symmetric (left) and antisymmetric (right) modes of the final section of the adiabatic coupler, with 50-nm-thick and 400-nm-wide GeTe.

Although some limited portions of the modes remain shared between the waveguides, the large majority of the field is localized in only one of them. In particular, the symmetric mode (on the left, with higher index) propagates in the hybrid WG, while the antisymmetric mode (on the right, with lower index) is confined in the silicon one. A similar result has been obtained also for a crystalline PCM, but with even higher effective indices, meaning that the modes are even better separated.
The main challenge in this situation was to design an overall structure in which the excitation of the same input mode (coming from the single Si waveguide) would evolve either in the fundamental or in the second mode depending only on the state of the PCM, so respectively transferring to the hybrid waveguide, in the ON state, or remaining in the Si one, with an OFF switch. To fulfill this purpose, an accurate analysis of the distributions of these two modes for different PCM widths (and gaps) has been performed dividing the geometry in the middle: in the two resulting halves of the surface, the power flow transported by each mode has been computed as the surface integral of the square of the electric field (see Appendix A). The ratio between the values calculated in each half finally gives an estimation of how the mode is distributed. Fig. 4.10 presents the results obtained for amorphous GeTe at different thicknesses and for a gap of 200 nm.

For each parametric variation, the ratio has been always computed between the left and the right side. In consequence, a value higher than one refers to a situation

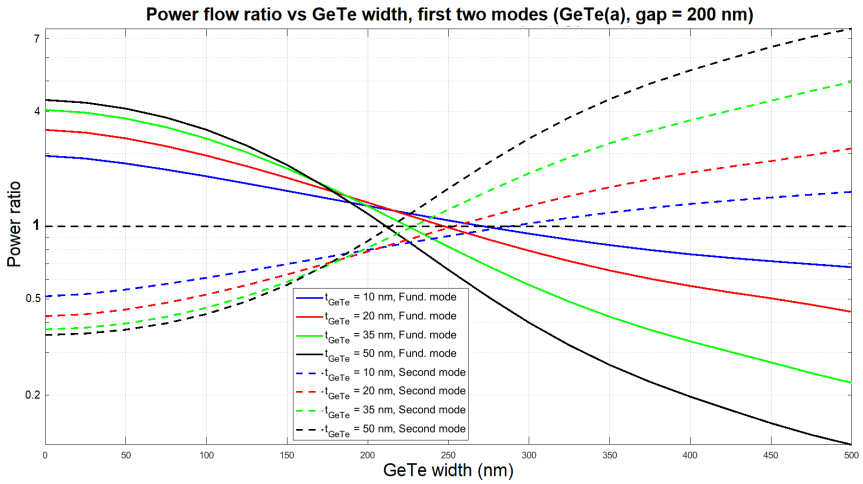

Figure 4.10: Ratio between the power flow in the left and right side of the geometry, for different thicknesses of amorphous GeTe and a gap of 200 nm (log scale).

in which the mode is more confined in the Si waveguide, and, vice versa, a lower value means that the mode propagates more in the hybrid one. The picture shows that for small GeTe widths, the fundamental mode (solid lines) is located more in the left half, while the second one (dashed lines) is more on the right. Then, for increasing widths (and so, along the coupler) they exchange and at the end they present an opposite configuration. The cross point is attained for a ratio almost equal to one just in correspondence of the optimal widths used in the 2D coupler, meaning that the results are consistent.
This modes exchange is, for all intents, the necessary condition to obtain the power exchange between the waveguides. Therefore, the initial width must be lower than the one for which the crossing happens, while the final one must be higher. The choice of these parameters is then driven by the principle for which the more separated the modes are at the edges of the adiabatic coupler, the better the device works. In consequence, observing the figure, the most desirable situation would be with the largest difference possible between the initial and final widths. Nevertheless, the first one would be limited by the fabrication constraints to around 150 nm, while the second cannot exceed the width of the core.
As a last remark concerning the thickness, it can be noticed that the modes are better separated with a thicker PCM. However, this would also produce higher losses, therefore the optimal situation can be only extracted by the 3D model.
On the other side, the result obtained in the same case, but with crystalline GeTe is shown in Fig. 4.11.

Comparing this picture with the previous one, a similar trend is followed by both

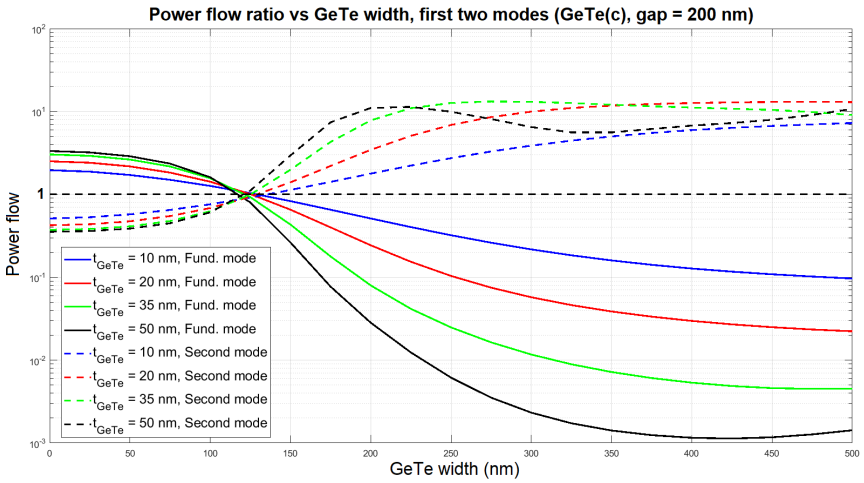

Figure 4.11: Ratio between the power flow in the left and right side of the geometry, for different thicknesses of crystalline GeTe (gap = 200 nm, log scale).

modes with respect to PCM width and thickness. However, because of the much large scale on the Y axis, a better separation is expected, especially at the end of the structure. The crossing point is shifted towards smaller widths, confirming the results of the optimal width extraction summed up in Table 4.1.
The fundamental difference with respect to the previous discussion is that in this case no coupling should happen. Therefore, the modes exchange between the waveguides must be avoided. In consequence, also the initial width of the adiabatic coupler should lie beyond the crossing point, in order to maintain the modes in the waveguide from which they started propagating. Observing the picture, this means that the lower bound for this parameter is around 150 nm, a value that perfectly fits both the fabrication constraints and the results of the previous analysis on the amorphous case. The only potential issue is that little margin is left from the crossing point and, in consequence, at input of the device a limited coupling could be obtained also when the switch is supposed to be OFF.

In conclusion, thanks to this 2D evaluation of the adiabatic coupler, the range of optimal values for the initial and final widths of the component have been extracted. In particular, the first one must lie between 150 and 200 nm, while the second one should be as large as possible, so around the same width of the Si core.
Up to this point, the analysis has been performed with both GeTe and GST, obtaining analogous results. However, the 3D model has been created only employing GeTe, since the introduced losses are expected to be much higher in the case of GST, especially in the largest sections of the device. A future continuation of the project will potentially analyze also this second alternative.

4.3 Adiabatic coupler design: 3D analysis

Once completed the 2D analysis, with the extraction of all the optimal values for the different sections of the adiabatic coupler, the conclusive step of the design process consisted in the creation of the 3D model. At this point all the ingredients to finalize the geometry of the device had been obtained and, therefore, the only obstacle to overcome was the difficulty to face with such a new and complex simulation environment.
The main challenge imposed by the 3D structure was the definition of the excitation of the device, for which the Beam Envelopes Interface allows the definition of input and output ports. Indeed, while the lateral sides of the geometry along the waveguide could be treated in the same way as for the 2D model (i.e. applying the Impedance Boundary Conditions), the definition of the boundary conditions to be set for the ports was not so straightforward. In consequence, some preliminary models have been created to perform additional tests in this regards.
Therefore, starting from the implementation of simpler geometries, the final structure of the adiabatic coupler has been built by successively refining the model used in the previous steps.
All the 3D simulations presented in the following sections have been performed only employing GeTe, as stated at the end of previous section.

4.3.1 Silicon waveguide and hybrid directional coupler

The first step towards the creation of the 3D model was the implementation of some test geometries, to understand all the additional features provided by the Beam Envelopes Interface of the Wave Optics Module. In particular, the major challenge was the creation of the input and output ports, respectively for the excitation of the modes and to observe their evolution at the end of the structure. Fig. 4.12 shows the two most relevant examples among the preliminary geometries implemented for this preliminary study.

In particular, Fig. 4.12(a) presents the result of the propagation of the fundamental mode in a single Si waveguide oriented along the x axis, with excitation from a single input port. The norm of the electric field is plotted on a horizontal slice disposed in the middle of the waveguide, deformed vertically to better show the intensity variation of the mode. It can be observed that the latter is well peaked in the middle of the geometry, and propagates along the waveguide without undergoing modifications. This means that, as expected, a structure only made of silicon is ideally lossless. If additional input (and associated output) ports are included, multiple modes can be excited, and the intensity of the electric field is modified according to their superposition.
On the other hand, Fig 4.2.2(b) presents the power transfer in a hybrid directional

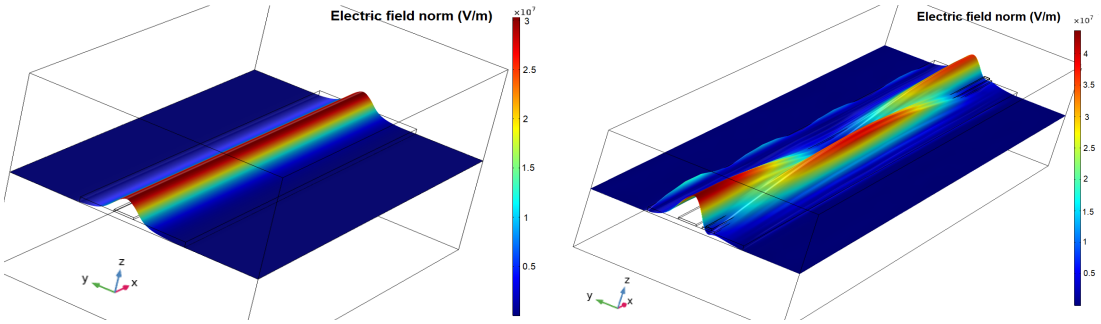

(a) *Si rib waveguide, fundamental mode* **(b)** *Directional coupler, power transfer*

Figure 4.12: Results of the simulation of the 3D model of a single silicon rib waveguide (left) and a hybrid directional coupler, which employs a 50-nm-thick layer of GeTe with its associated optimal width extracted in Sec. 4.2.2 (right).

coupler, the direct 3D extension of the 2D model presented in 4.2.3. In particular, looking from the front of the structure, the left rib waveguide is made of only Si, with the conventional 600 nm core width, while the right one includes a 50-nm-thick layer of GeTe on top, whose width is the optimal one of 422 nm, extracted in 4.2.2. The gap is set to 200 nm. This time, two input and two output ports have been disposed, for the excitation of both the symmetric and antisymmetric modes of the system. Always considering a slice disposed as in the previous model, it can be observed that the guided power is correctly and completely transferred from one waveguide to the other. Since the coupler is 25 μm long, around twice as the expected coupling length for this configuration of 12.2 μm (computed in 4.2.3), a second power transfer happens, and the latter returns in the Si waveguide from which it started. Similar results have been obtained with some variations of the geometrical parameters. In this case the signal at the end of the structure is slightly attenuated with respect to the input one, due to the presence of the lossy PCM. Therefore, some attenuation is expected also in the subsequent analysis.

4.3.2 Adiabatic Coupler

First implementation

After having tested the different features of the 3D simulation environment, the model for the adiabatic coupler has been created. Its first implementation was obtained by modifying the structure of the directional coupler presented in Fig. 4.12(b) to have a variable PCM width. The resulting geometry is the one shown in Fig. 4.1(b), in which all the parameters have been selected accordingly to the results of the 2D analysis of the component. In particular, the optimal width for

the Si core of the hybrid waveguide has been extracted from Tab. 4.1, while the initial and final widths of the PCM have been obtained from the discussion in Sec. 4.2.4.
The aim of this model was to observe, on one side, the behaviour of the component for both PCM states, to prove that the signal can be manipulated thanks to its actuation, and, on the other, to estimate the coupling length of the device. The simulation has been performed mainly varying two parameters, the PCM thickness (with the associated variation of optimal Si core width) and the middle gap between the waveguides. Again, two input and two output ports have been used, for the excitation of the first two modes of the system. The results for both states of a 20-nm-thick layer of GeTe and a gap of 300 nm are shown in Fig. 4.13. This time, the plot shows a top view of the electric field norm along a slice disposed in the middle of the waveguide as done in Sec. 4.3.1, but without the vertical deformation.

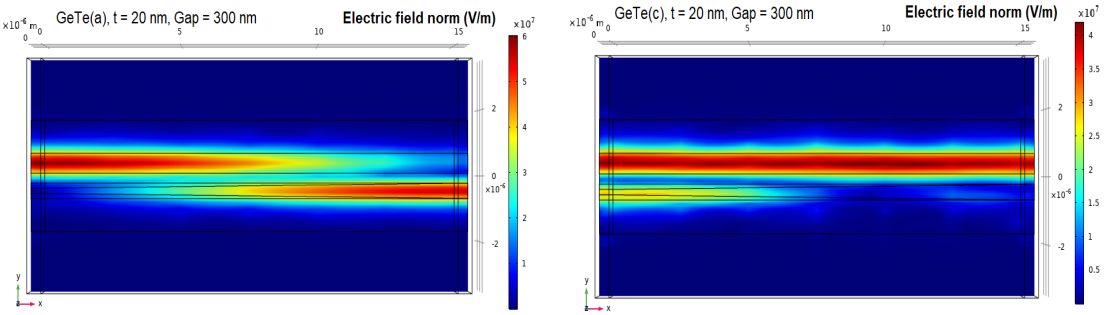

(a) *Amorphous GeTe: coupling ON* **(b)** *Crystalline GeTe: coupling OFF*

Figure 4.13: Top view results of the first 3D model of the adiabatic coupler, for 20 nm of amorphous (left) and crystalline (right) GeTe and a gap of 300 nm.

It can be observed that the simulated device works as expected. In particular, Fig. 4.13(a) presents the outcome in the case of amorphous GeTe, a condition that allows the power transfer between the waveguides with a coupling length of around 15 μm, even smaller than the one estimated in Tab. 4.2 for this configuration. The electric field is slightly attenuated at the output of the structure, with a peak value in the middle of the hybrid waveguide of around 5.5 x10^7 V/m, against an initial value of around 6 x10^7 V/m.
After the actuation, in Fig. 4.13(b) the coupling condition is not fulfilled anymore, and the signal remains located inside the Si waveguide. In this case, no particular attenuation is present, since no power flows inside the lossy PCM. However, a partial and unintended coupling happens at the input of the structure. This effect potentially represents an issue, which could lead to the loss of the transferred portion of the signal. The evaluation of this aspect has been attempted in the successive models.

After having shown the working principle of the device, the geometry has been slightly modified elongating its final portion while maintaining the width of the elements constant, with the idea of evaluating the behaviour of the field after the already simulated region. Indeed, as discussed in Sec. 2.2.3 and 4.2.4, the adiabatic coupler presents a variable width in its second branch to fulfill the coupling condition only in its central section, and not at the edges, in which the effective index does not match the one of the first branch. Therefore, in this last case the waveguides should be, in principle, not coupled. Following this consideration, with GeTe in amorphous state, after the power is transferred it should remain in the hybrid waveguide, while with a crystalline PCM it should be confined in the Si one without being altered. The results of this evaluation are shown in Fig. 4.14.

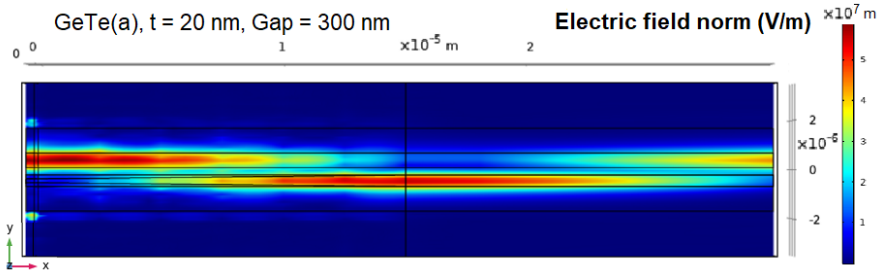

(a) *Amorphous GeTe: coupling ON*

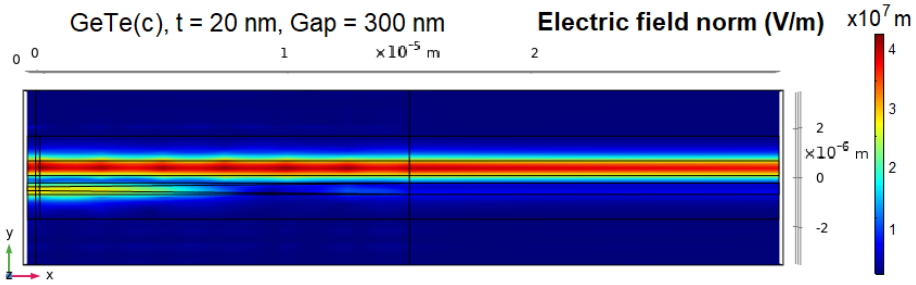

(b) *Crystalline GeTe: coupling OFF*

Figure 4.14: Top view results of the first 3D model of the adiabatic coupler, for 20 nm of amorphous (left) and crystalline (right) GeTe, a gap of 300 nm and an elongated final portion.

Observing Fig. 4.14(a), it can be noticed that a portion of the signal is transferred back again in the Si waveguide. This behaviour obviously does not comply with the specifications of an ideal adiabatic coupler, but the effect is only partial. More importantly, this second coupling requires a longer region to be completed: even at the end of the additional portion of 15 μm the power only starts to be transferred, meaning that the waveguides are only partially coupled in this section. A practical solution to avoid this effect consists in deviating the hybrid waveguide,

consequently increasing the gap to values of few microns, sufficiently large to eliminate the residual coupling. On the other hand, considering a crystalline PCM as in Fig. 4.14(b), it can be noticed that no coupling happens in the additional region, in which the signal only undergoes a negligible attenuation. The latter would be anyway avoided distancing the waveguides as proposed above.

Second implementation

After the conclusion of the initial analysis, the model has been improved by adding some features of a more real device. Indeed, as previously discussed, the waveguides must be close at a fixed gap of few hundreds of nm only in the region presented in Fig. 4.13 to allow the selective coupling, otherwise they should be far apart. Therefore, the second implemented geometry included a bend portion for the hybrid waveguide at the input of the structure, while the Si one has been simply elongated in the same direction. The additional bend portion was generated through a combination of MATLAB and L-Edit, and later imported into Comsol. Its function also consists in allowing a gradual approach of the hybrid waveguide to the coupling region, in order to reduce potential reflections due to the discontinuity. The result is shown in Fig. 4.15.

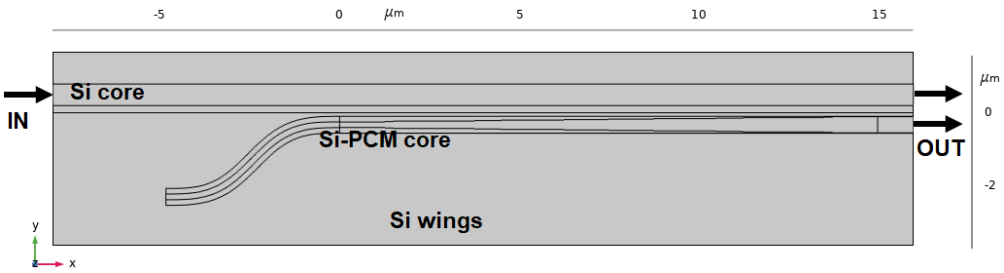

Figure 4.15: Top view of the geometry of the second 3D model for the adiabatic coupler (air and SiO_2 layers are missing to better observe the core regions).

Since the additional bend portion is shorter than the corresponding straight one of the Si waveguide, the input can be injected in the system only from the latter, which can be initially considered independently. This condition enables the simulation of a more real situation, in which the signal only comes from one waveguide, and then it is selectively coupled to the second one. In consequence, in this case a single input port has been included, for the excitation of the fundamental mode of the single Si rib waveguide. Two output ports have been then considered to observe the evolution of this mode in both waveguides.
The simulation has been performed again for both PCM states, and for multiple

thicknesses and gaps, respectively in the range 10 - 50 nm and 200 - 400 nm. The results for a 20 nm layer and a gap of 300 nm are shown in Fig. 4.16.

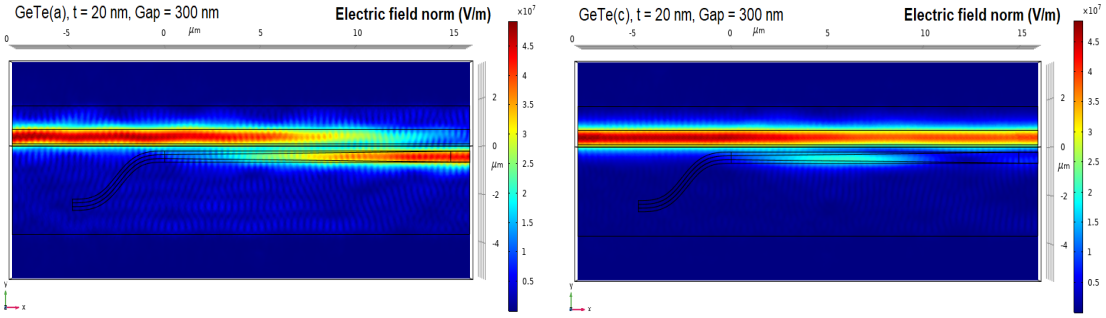

(a) *Amorphous GeTe: coupling ON* **(b)** *Crystalline GeTe: coupling OFF*

Figure 4.16: Top view results of the second 3D model of the adiabatic coupler, for 20 nm of amorphous (left) and crystalline (right) GeTe and a gap of 300 nm.

In both pictures, it can be observed that the additional bend portion does not affect the signal propagation, and effectively reduces the reflections due to the presence of the second waveguide. On the other hand, the signal correctly evolves as predicted, transferring to the hybrid waveguide with amorphous GeTe (Fig. 4.16(a)) or remaining in the Si one after actuation (Fig. 4.16(b)). It can be also noticed that in both cases a certain attenuation of the field is present, respectively due to the propagation in the lossy PCM, and to the same unintended coupling observed in the first model.
The analysis of the performed parametric sweep allowed to estimate the dependence of these effects on both the PCM thickness and the gap. In particular, with a thicker PCM higher losses are introduced in its amorphous state, while in the crystalline one the parasitic coupling is reduced. On the other side, a larger gap makes the waveguides more independent, therefore causing an increase of both the coupling length and the attenuation of the signal with amorphous GeTe, while reducing the parasitic coupling in the crystalline state. To be more clear, employing a thicker PCM and a wider gap, better results have been obtained for crystalline GeTe, with a less and less attenuated signal in the Si waveguide, and vice versa for the amorphous state. A tradeoff was necessary to obtain the best compromise between the two trends.
A more precise study of these dependence has been performed by dividing in half the geometry, and extracting in both halves the power flow (as explained in Appendix A). The idea was, similarly to what had been done in Sec. 4.2.4, to compute the ratio between the values obtained in the two regions, evaluating in which case the signal is more confined in one or the other waveguide. The power flow ratio for both PCM states is shown in Fig. 4.17.

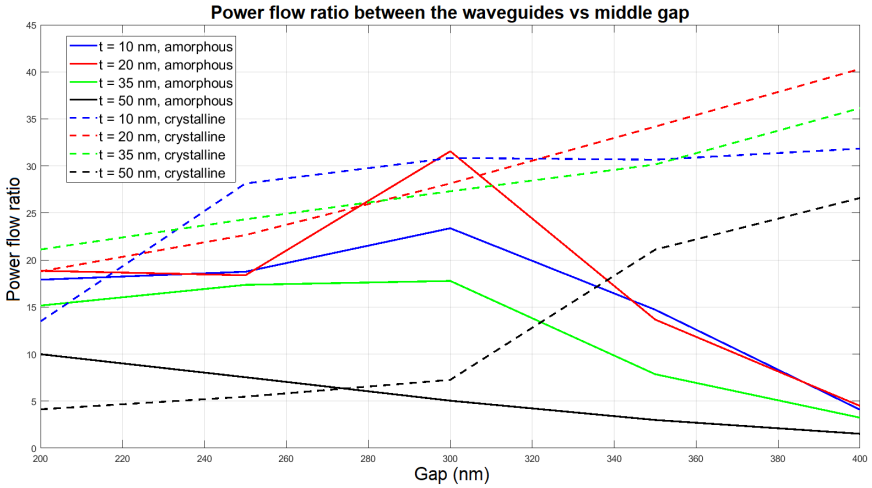

Figure 4.17: Power flow ratio at the output of the adiabatic coupler for both amorphous and crystalline GeTe.

It can be observed that each curve presents values higher than one. This is due to the fact that the ratio has been always computed choosing as numerator the power flow extracted in the portion in which the signal was expected to be higher, i.e. in the hybrid waveguide for amorphous GeTe, and the Si one for the crystalline state. In this way, the best geometrical configuration can be selected as the one for which the ratio is maximized in both states. Observing the figure, it can be noticed that the optimal configuration for the system is obtained with a thickness of 20 nm and a gap of 300 nm. Indeed, for this geometrical combination a ratio around 30 is obtained for both PCM states, meaning that the signal is in both cases highly confined in the correct waveguide.

Third implementation

After having extracted the optimal geometrical parameters of the adiabatic coupler, i.e. a GeTe thickness of 20 nm and a gap of 300 nm, a conclusive, more complete 3D model has been created improving the waveguides structure at the output of the system. Indeed, as anticipated above, after the coupling region they must be drifted apart, to avoid any unnecessary interaction between them. The additional portions have been again generated combining MATLAB and L-Edit, resulting in the geometry shown in Fig. 4.18.

As for the previous model, only one input is present for the excitation of the fundamental mode of the single Si waveguide, while in output both waveguides are considered, this time separated by a large gap of few microns.
The aim of this third model was, on one side, to evaluate the evolution of the signal

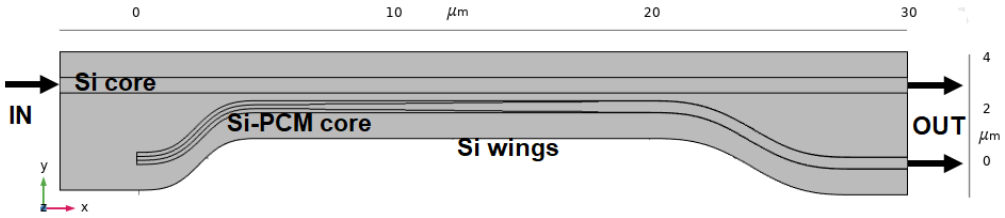

Figure 4.18: Top view of the geometry of the third 3D model for the adiabatic coupler (air and SiO_2 layers are missing to better observe the core regions).

in a complete structure, and, on the other, to perform a conclusive analysis of the dependence of the results on the operating wavelength. Indeed, as mentioned in Sec. 2.2.3, the main advantage of the adiabatic coupler with respect to the directional one is that the latter presents a limited bandwidth, while the former is, in principle, more stable with respect to wavelength variations. A parametric sweep has been therefore performed in the range between 1500 and 1600 nm, centered in the target value of 1550 nm. The results for the optimal wavelength and for both PCM states are presented in Fig. 4.19.

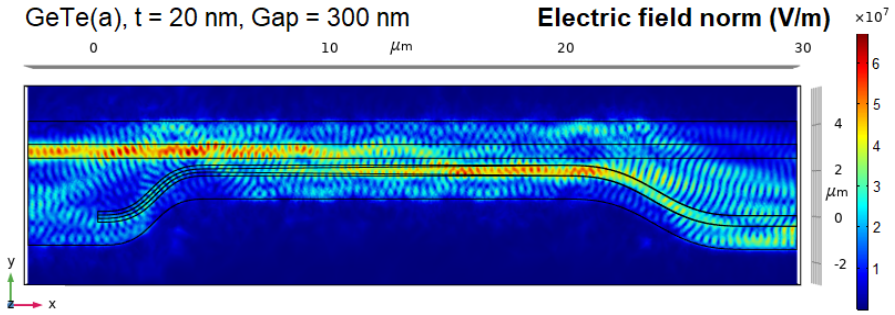

(a) *Amorphous GeTe: coupling ON*

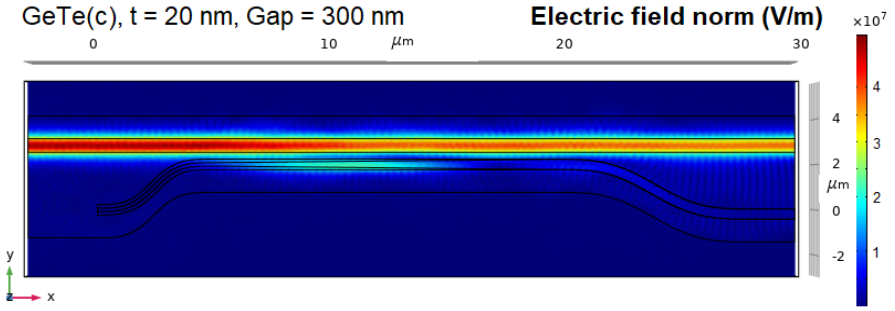

(b) *Crystalline GeTe: coupling OFF*

Figure 4.19: Top view results of the third 3D model of the adiabatic coupler, for 20 nm of amorphous (top) and crystalline (down) GeTe and a gap of 300 nm.

It can be clearly observed that, despite a good outcome shown in Fig. 4.19(b) with a crystalline PCM, in which the signal correctly remains in the Si waveguide without undergoing modifications after the coupling region, a non correct behaviour has been obtained with amorphous GeTe. As shown in Fig. 4.19(a), the coupling happens as expected, since the signal is transferred to the hybrid waveguide, being almost null in the Si one at the output. However, the field distribution seems highly scattered, and its continuous character, correctly obtained in the previous simulations, is lost. This outcome can attributed either to some artifacts of the simulation, not perfectly completed in the case of this imported external geometry, or to a too narrow curvature of the final bend portion, which can lead to losses and scattering while deviating the signal.
Many different simulations have been run trying to correct this issue, modifying the input/output ports, refining the mesh, or changing some parameters of the geometry, in particular reducing the curvature of the bend portions. Unfortunately, none of them provided good results in the case of an ON coupling, for which a much similar outcome has been always obtained. In conclusion, mainly due to the approach of the end of the project, the issue was not resolved, and the conclusive wavelength analysis could not be completed. A future continuation of the project will surely have to refine this last model, looking for a more accurate solution.

4.4 Phase Shifters

The process for the design of the phase shifters has been carried on in parallel with that of the adiabatic coupler, exploiting the same simulation models used in that previous analysis. The idea was, in this case, to optimize the geometrical parameters of different PCM portions deposited on top of a conventional Si rib waveguide (like the one proposed in Sec. 4.2.1) to obtain elements that, depending on the state of the PCM, can cause a controlled phase delay in the propagating EM wave. The final goal was, thanks to multiple phase shifters, to implement an active MZI (see Sec. 2.2.4). A schematic of the top view of a single phase shifter, for two possible different implementations, is shown in Fig. 4.20.

In particular, Fig. 4.20(a) presents a simpler rectangular geometry, in which the width of the PCM remains constant, while Fig. 4.20(b) illustrates a more complex structure with a larger element in the central section, and a gradual variations towards its narrower edges. In the first case, the advantage would be a more reliable fabrication. However, to ensure a proper phase shift, the element must be large enough already from its initial section, presenting a more abrupt variation of the structure to the incoming wave. The potential result would be a larger reflection at the interface, with the consequent loss of a portion of the signal. On the other hand, the higher complexity of the second implementation could

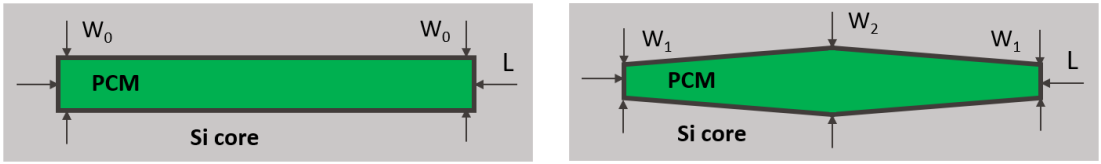

(a) *Rectangular geometry, constant PCM width* **(b)** *Polygonal geometry, variable PCM width*

Figure 4.20: Schematic of the top view of two alternative implementations of the phase shifters, with a PCM layer deposited on top of the Si core.

allow a more gradual transition for the propagating wave, reducing the reflection. Nevertheless, the optimal configuration would require an ideal zero initial width for a fully progressive transition, but the already mentioned constraints imposed by the selected fabrication process, and in particular by the minimum resolution of DUV lithography (studied in Sec. 3.4 and 3.5), set the minimum width to around 150 nm, so that a certain reflection would be anyway present. Both implementations have been analyzed and compared, looking for the configuration that, at equal produced phase shift, presents smaller dimensions and reduced losses.

4.4.1 Geometrical design

The main principle on which the proposed phase shifters rely is a variation of the propagation constant of the EM wave inside the waveguide due to a change in the PCM state, which modifies the effective index of the guided modes. Indeed, the relation between these quantities (respectively β and n_{EFF}) can be written as

$$\beta = \frac{2\pi \cdot n_{EFF}}{\lambda_0} \tag{4.4}$$

in which λ_0 is the operating wavelength, in this case equal to 1550 nm. By computing the difference between the constant associated to a crystalline and to an amorphous PCM (β_C and β_A respectively), the phase shift due to actuation can be obtained. Indeed, the electric field in the waveguide can be expressed as in Eq. 2.1, with a fixed distribution in the perpendicular section, and proportional to $exp(-j\beta z)$, the propagation term along the WG axis. Considering a PCM element of length L starting in position z = 0, the phase of the wave on the other edge is therefore expressed as $\phi = \beta L$, and the phase shift after actuation is computed as

$$\Delta\phi = |\phi_C - \phi_A| = |\beta_C L - \beta_A L| = \Delta\beta \cdot L \tag{4.5}$$

The objective of this analysis was to obtain the optimal combination of PCM length and width (the latter affecting the modes effective index) whose product

can lead to significant values of phase shift, for instance equal to π, $\pi/2$, $\pi/4$ and so on.
The design procedure started with the modification of the model used in Sec. 4.2.2 to simulate a hybrid Si-PCM rib waveguide. For this analysis, the width and thickness of the Si core have been fixed to 600 nm and 60 nm respectively, while a parametric sweep has been performed on the dimensions of the top PCM layer. The objective was, for each combination of thickness ranging between 10 - 50 nm, and width going from 100 nm to 600 nm, to extract for both states of the PCMs the effective index of the fundamental mode, whose distribution along the surface is totally analogous to the one presented in Fig. 4.4. Although the smallest width should be limited to 150 nm, the simulation has been anyway performed for values down to 100 nm, including a wider range in case the device processing resulted in elements slightly narrower than designed.
Once the target effective index has been collected for each geometrical combination, its value has been employed to extract the propagation constant of the mode, with Eq. 4.4. The result for some relevant PCM thicknesses (10, 20, 35 and 50 nm) and for both states of the two PCMs are shown in Fig. 4.21.

First, it can be observed that a similar behaviour is presented for both PCMs, with a monotonously increasing propagation constant for larger widths, regardless of the state or of the thickness. Then, concerning these last two parameters, higher values of beta are always obtained in the crystalline state, and with a thicker deposited layer. However, a bizarre trend is followed by the curves related to the thickest elements in the case of GST: indeed, in the width range between 150 nm and 300 nm, instead of a monotonous behaviour, the curves start decreasing, before an abrupt increase towards more reliable values. This issue has been attributed to some artifacts of the simulation, which has been relaunched multiple times with different setups, providing always similar results. As a consequence, the design procedure has been completed focusing mainly on GeTe.
Before proceeding with the extraction of the optimal geometrical parameters, an additional manipulation of the obtained results was necessary to evaluate the effect of a variable width in the same phase shifter. Indeed, for the first implementation in Fig. 4.20(a), a constant width W_0 allows to immediately obtain (from the curves) the related propagation constant, which remains the same along the whole length of the element. However, for the second geometry of Fig. 4.20(b), this association is not straightforward, since a variable section of the waveguide causes a gradual modification of the mode effective index. Therefore, the mean value of effective index has been calculated for each combination of W_1 and W_2 as

$$\beta_{MEAN} = \frac{1}{W_2 - W_1} \cdot \int_{W_1}^{W_2} \beta(w) dw \tag{4.6}$$

to estimate the overall effect of a variable PCM width on the signal.

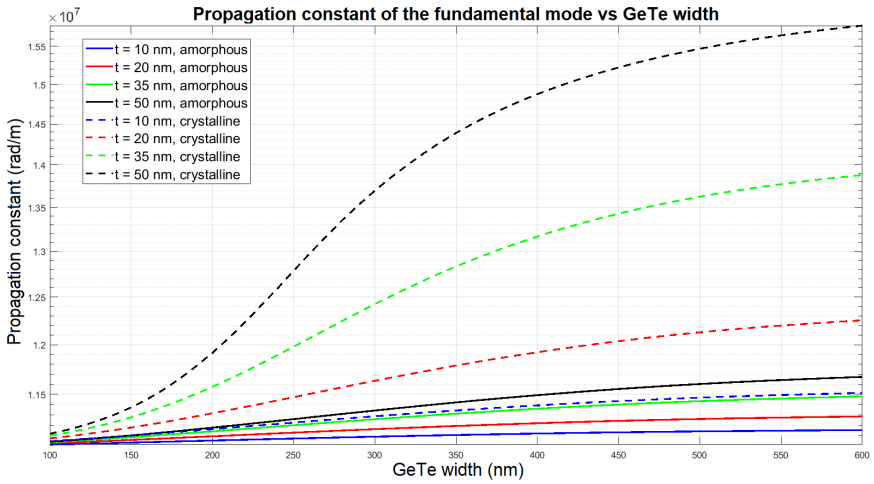

(a) *Propagation constant, GeTe*

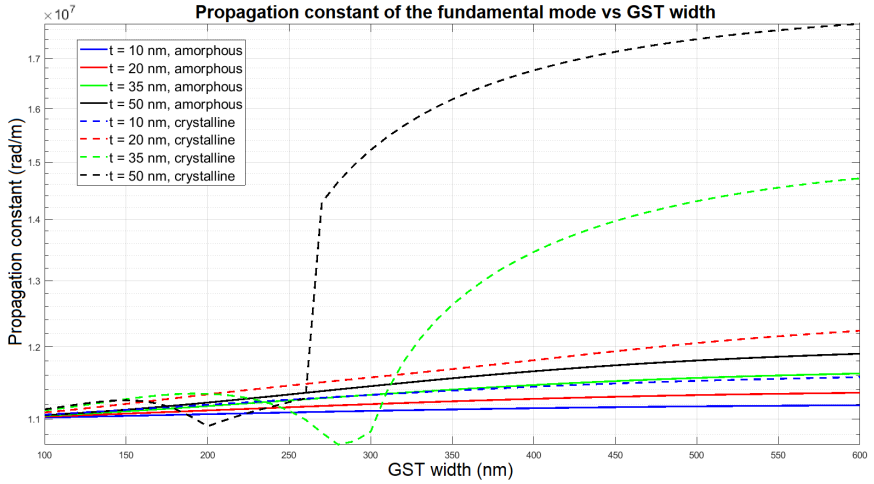

(b) *Propagation constant, GST*

Figure 4.21: Propagation constant of the fundamental mode for varying GeTe (left) and GST (right) width at different thicknesses and for both states.

At this point, the conclusive extraction of the optimal geometrical parameters was ready to be performed. In order to obtain the results in an efficient way, avoiding a huge analysis over many different lengths, the computation has been carried out starting from the target phase shifts, fixing them as the result of the product presented in Eq. 4.5. Considering a generic phase shift PS, for each combination of initial and final widths of the PCM element (and so for each associated value of

$\Delta\beta$) the optimal length has been computed as

$$\Delta\phi = \Delta\beta \cdot L_{OPT} \quad \Longrightarrow \quad L_{OPT} = \frac{\Delta\phi}{\Delta\beta} \tag{4.7}$$

The procedure has been performed for all the analyzed thicknesses, and all the phase shifts written in the form $\pi/2^n$, with n going from 0 to 4, to obtain a full set of elements for the manipulation of propagating signal. In principle, the optimal length for any other phase shift could be obtained with the same computation. The results for a $\pi/2$ shift and for various GeTe thicknesses are presented in Fig. 4.22.

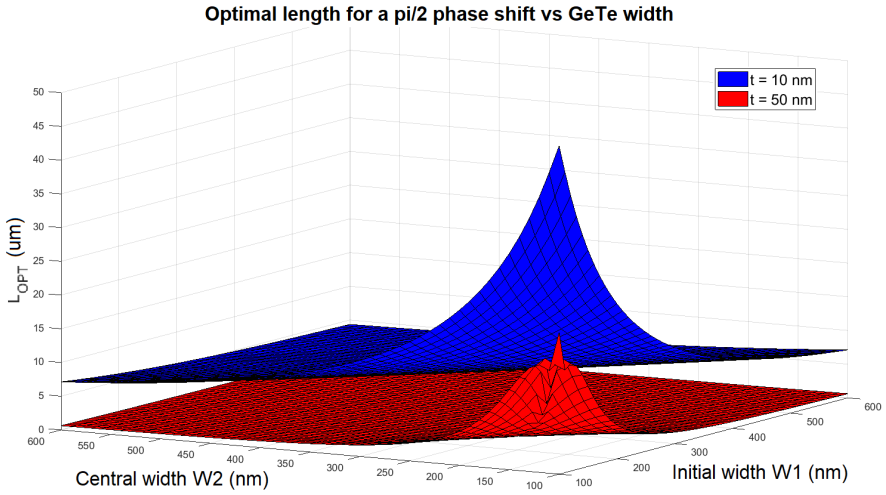

Figure 4.22: L optimal for a pi/2 phase shift, for GeTe at different thicknesses.

In the graph, the widths of the initial and central sections of the device (W_1 and W_2) are respectively disposed on the x and y axes, while the optimal length associated to each combination is plotted along z. In this way, both the proposed implementations for the phase shifter have been analyzed at once. Indeed, along the diagonal of the obtained surfaces, W_1 equals W_2, meaning that the element presents a constant width as in the rectangular structure, while all the other points refers to the polygonal one. It can be observed that, for each thickness, a longer length is required for narrower devices, meaning that the effect due to actuation is less pronounced than for a larger one (since in Eq. 4.7 L_{OPT} is inversely proportional to the propagation constant difference). Then, for the same width, a shorter length is obtained for a thicker PCM, which causes a larger modification in β. To give a quantitative example, for a 10-nm-thick layer the optimal length ranges from around 49 μm to 4 μm, while the related values for a thickness of 50 nm are 21 μm and 0.4 μm.
Similar trends have been obtained for each analyzed phase shift, for all thicknesses

and both materials, due to the direct proportionality in Eq. 4.7 of the optimal length with respect to the shift.
In conclusion, the most compact solution possible can be obtained employing a thicker and wider PCM, since the more material is present, the more pronounced its effect over the signal is. In particular, always considering the same phase shift of $\pi/2$, with GeTe the length of the element could be reduced down to 0.4 μm for a thickness of 50 nm and a width of 600 nm, as large as that of the Si core. The analogous length employing GST would be of around 0.3 μm. In both cases, the obtained values could allow the creation of highly compact and integrable optical components.

4.4.2 Losses estimation

Even if the optimization procedure could be concluded at this point, all the analysis has been performed so far without considering the produced losses. Indeed, as previously mentioned for other simulations, and also as expected from literature, when PCMs are involved the losses they introduce in the system can become dominant with respect to the ones due to surface scattering (see Sec. 2.2.1 and 2.3). Therefore, the study for the phase shifters had to be completed by estimating the losses produced in each geometrical configuration.
As already performed in Sec. 4.2.3, the loss per unit length can be obtained from the imaginary part of the effective index of the analyzed mode using Eq. B.3. Fig. 4.23 shows the results for both PCMs for all the thicknesses previously studied.

It can be noticed that for both materials the trend followed is the same, with increasing losses both for larger width and thickness. The behaviour is also similar with respect to actuation, with higher values in the crystalline state. In particular, for GeTe losses are between 10^2 and 10^3 dB/cm in the amorphous state, while after actuation they increases to a range between 10^3 and, for the higher thicknesses, 10^5 dB/cm. On the other hand, for GST the range is almost the same for the amorphous case, while it is quite larger after actuation, up to around $6 \cdot 10^5$ dB/cm. Therefore, in this case a higher attenuation of the signal is expected.
Once the losses per unit length have been computed, the total expected losses for each geometrical combination could be obtained simply multiplying those values for the optimal length previously extracted. Therefore, the resulting expression for this quantity becomes (with p.u.l. = per unit length)

$$Loss_{TOT} = Loss(p.u.l) \cdot L_{OPT} = Loss(p.u.l.) \cdot \frac{\Delta\phi}{\Delta\beta} \tag{4.8}$$

with a direct proportionality with respect to the phase shift and inverse proportionality with respect to the difference in mode propagation constant. The results

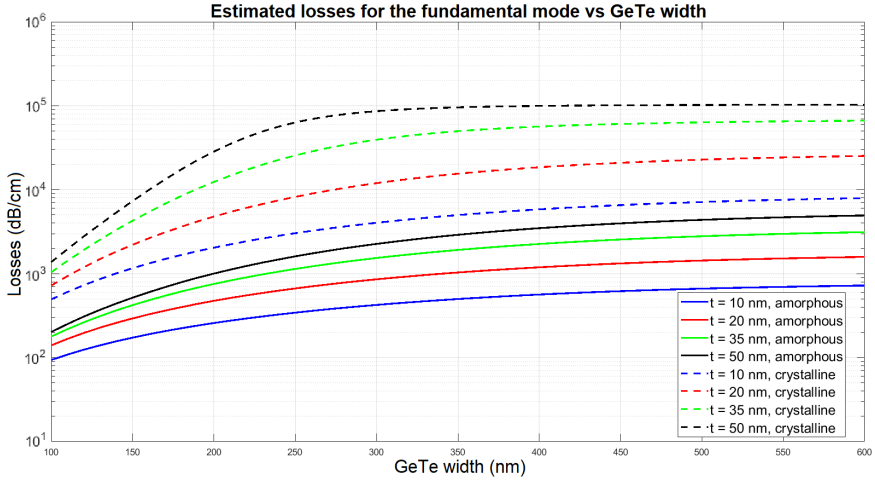

(a) *Losses per unit length, GeTe*

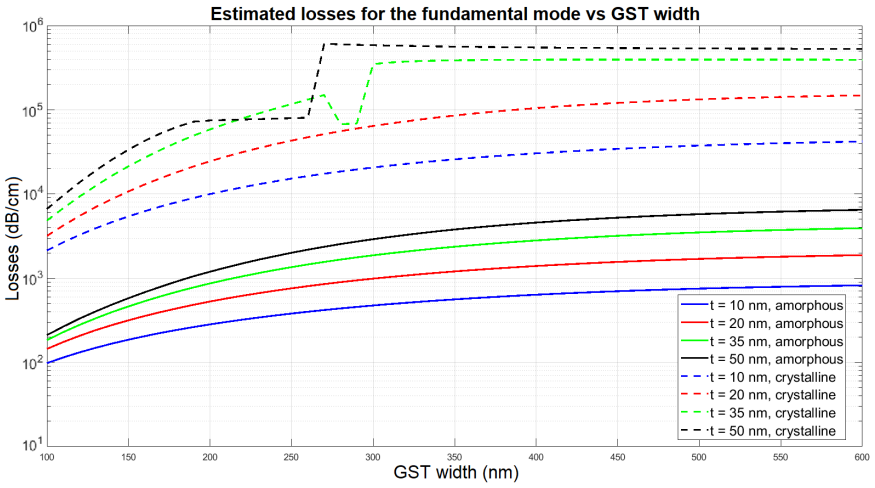

(b) *Losses per unit length, GST*

Figure 4.23: Estimated losses per unit length for the fundamental mode for varying GeTe (left) and GST (right) width and thickness and for both states.

of this computation for Two different GeTe thicknesses, and for a phase shift of pi/2 are shown in Fig. 4.24.

It can be observed that the followed trend is opposite with respect to the one presented in Fig. 4.22 concerning the optimal length. Indeed, in this case lower losses are obtained for narrower widths and for smaller thicknesses, due to the fact that the less PCM is present, the more reduced its effect on the attenuation of the signal is. Actually, the behaviour is not completely monotonous, since for larger values of W_1 and W_2 the optimal length is so small that the product in Eq. 4.8

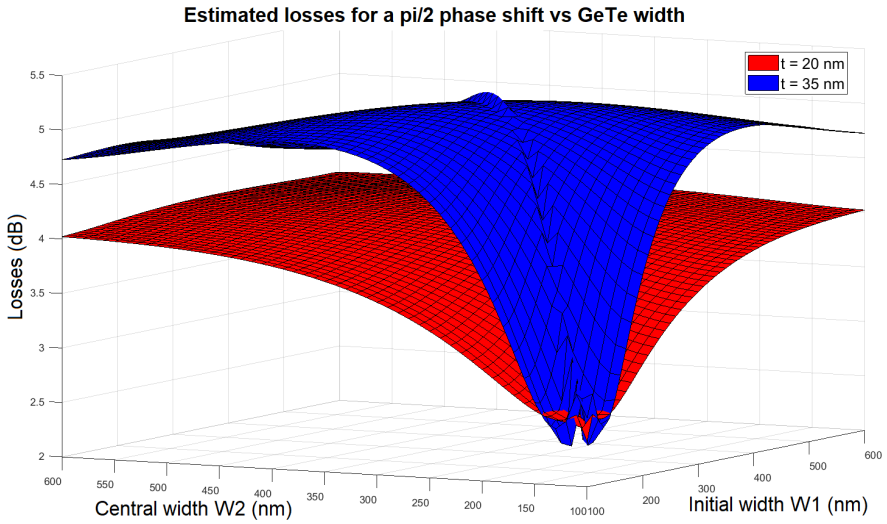

Figure 4.24: Estimated total losses for a pi/2 phase shift vs GeTe width, obtained at different PCM thicknesses.

starts decreasing. In particular, for a thickness of 20 nm the total losses range from 2.4 dB to 4.1 dB, respectively for widths around 100 nm and 600 nm, with an almost monotonous trend. For a thickness of 35 nm, the analogous values of losses are 2.6 dB and 4.4 dB, with a peak of 5.2 dB for intermediate widths. This behaviour is due to the fact that the optimal length for the largest widths is so small that the product in Eq. 4.8 decreases even if the expected losses per unit length monotonically increases.
In conclusion, a lower attenuation of the signal can be obtained reducing as much as possible the amount of deposited PCMs, therefore employing smaller dimensions for the phase shifters both in terms of width and thickness (while a longer length is expected). Since the estimated losses are in any case in the order of some dB, this parameter becomes highly dominant in the system, producing a more significant effect on the signal with respect to the expected scattering losses (see Sec. 2.2.1). Therefore, the final design choice must be performed with the idea of limiting as much as possible the loss produced by the additional PCM layer.

4.4.3 Conclusive parameters extraction

After the estimation of both optimal length and total losses associated to each geometry of the phase shifter, all the ingredients for the final choice of the most suitable parameters combinations were present. This conclusive extraction has been performed with the aim of designing the most compact and low-loss components possible. However, considering the dependence on the width of the elements,

opposite trends have been obtained for these two quantities: smaller optimal lengths are required for larger widths, but this would increase the related estimated attenuation of the signal. Therefore, a tradeoff solution becomes necessary.
In order to have an estimation of the quality of this compromise between length and losses, an interesting figure of merit (FOM) to be computed is the product between these quantities. Obviously, since the latter should be both reduced in the ideal case, the FOM should in principle be minimized as much as possible. The results for different thicknesses of GeTe and a phase shift of $\pi/2$ are presented in Fig. 4.25.

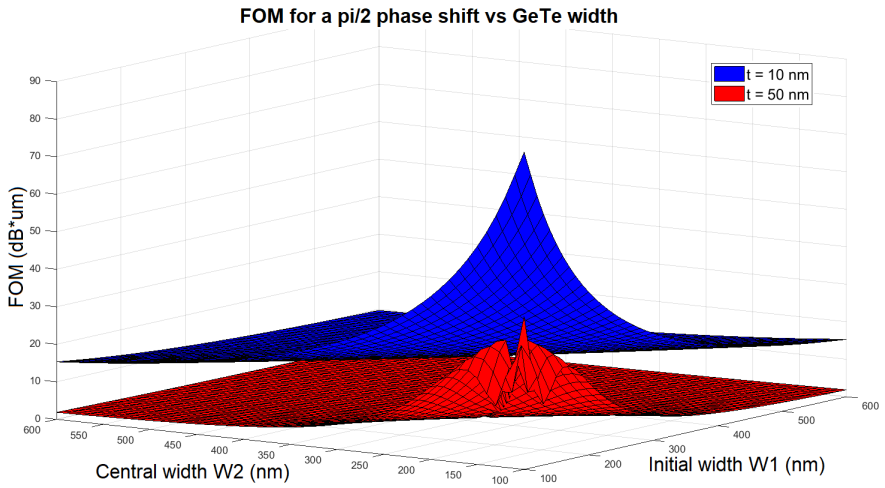

Figure 4.25: FOM for a pi/2 phase shift vs GeTe width at different thicknesses.

It can be observed that the FOM assumes higher values for narrower PCM widths and for smaller thicknesses. Therefore, from this estimation the best tradeoff would be obtained with a thicker and wider element. However, this conclusion is only partial: indeed, the FOM has been simply obtained by multiplying losses and optimal length, with a result that equally depends on them. Nevertheless, as discussed above, the quite high losses introduced by the PCM would represent by far the main contribution to the signal attenuation in the system, potentially reaching detrimental effects for higher dimensions of the elements. As a consequence, their influence on the tradeoff is much stronger than that of the optimal length, whose higher values could allow anyway a good integration.
The final choice of the design parameters for the phase shifters has been, therefore, mainly driven by the minimization of the attenuation of the signal caused by the deposited PCM, optimizing the device length only in a second step. Therefore, following the trend presented in Fig. 4.24, the best solution was to select the narrowest width possible of 150 nm, always complying with the constraints imposed by fabrication. Among the alternative implementations proposed in Fig. 4.20, this

limitation cancelled the advantages associated to the one with variable widths, and in consequence the rectangular geometry was chosen.
On the other hand, losses could be limited by reducing the PCM thickness. Considering a $\pi/2$ phase shift and the selected constant width of 150 nm, for a 50-nm-thick layer of GeTe the associated losses are around 4.3 dB, while for 10 nm they are reduced to 2.72 dB. However, among the range of smaller thicknesses, 20 nm was the one which presented the best combination of losses and optimal length: indeed, while the former are only slightly increased to 2.93 dB, the latter is highly reduced from around 23.4 μm for a 10 nm layer to 13.3 μm.
A totally analogous estimation could be performed with GST, but the corresponding values of length and losses for a 20 nm layer are respectively 12 μm, only marginally reduced, and 12.85 dB, clearly too high to be employed in the circuit.
In conclusion, GeTe has been selected as the material that, if employed to create a phase shifter, could allow a more limited attenuation of the signal. The optimal geometrical parameters obtained as the best tradeoff to limit the produced losses while providing a highly integrable structure are, for a phase shift of $\pi/2$, resumed in Fig. 4.26.

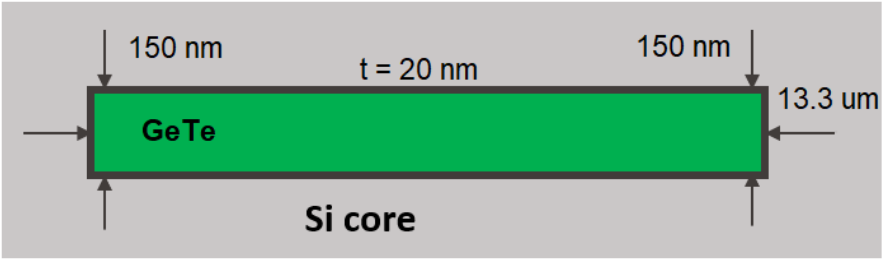

Figure 4.26: Optimal geometry of a phase shifter, for a $\pi/2$ phase shift.

In order to obtain a different phase shift, the only parameter to be modified is the length of the element, obtained employing Eq. 4.7.

Chapter 5

Proposed mask layouts of reconfigurable optics

After having completed the design of both the analyzed reconfigurable optical components, i.e. the adiabatic coupler and the phase shifter, with the extraction of their optimal parameters, the successive step towards the fabrication of real devices consisted in the creation of a dedicated photolithography mask, to perform the patterning of both the Si waveguides and the PCM top layer.
In particular, the layout of the various features to be opened on the mask has been generated through MATLAB. On one side, some codes already employed in other projects of the group has been reused, mainly to obtain generic and standard elements, as the optical interconnections between different devices, or the grating couplers to receive the input signal from external fibers. On the other hand, new routines have been implemented for the creation of more peculiar features, as the portions of the previously simulated and designed optical components.
The implemented geometries have been then imported into L-Edit, a specific software commonly used to work on mask layouts, in this case employed to connect the single structures created in MATLAB to obtain complete optical circuits.
An important aspect to be underlined is that the components generation through MATLAB has been fully parametrized. In this way, new elements can be obtained by simply modifying the input parameters of the codes, enabling a faster and more practical layout generation.
In this chapter, some of the most relevant layouts are presented. First, two main alternative implementations of 2x2 switch matrices have been generated exploiting the properties of the adiabatic couplers defined in Sec. 4.3.2. Then, different structures of MZI have been obtained employing as active elements different phase shifters among the ones designed in Sec. 4.4.

5.1 Switch matrix

The first set of proposed layouts concerns the implementation of optical switches (see Sec. 2.2.5), active optical components commonly employed either to modulate the propagating signal in terms of phase or intensity, or to deviate its path. The last option, in particular, has been targeted in this study, for the creation of reconfigurable and non-volatile components which exploit the properties of the analyzed PCMs.
The main idea behind this procedure was to propose a highly integrable alternative to currently employed switch matrices. The latter are optical components in which different signals coming from multiple, parallel waveguides can be processed simultaneously, either continuing along the same path or being selectively redirected towards perpendicular routes, respectively depending on the ON/OFF state of the switch disposed at the crossing. Fig. 5.1 shows the geometry of the optical switch proposed in the context of this project.

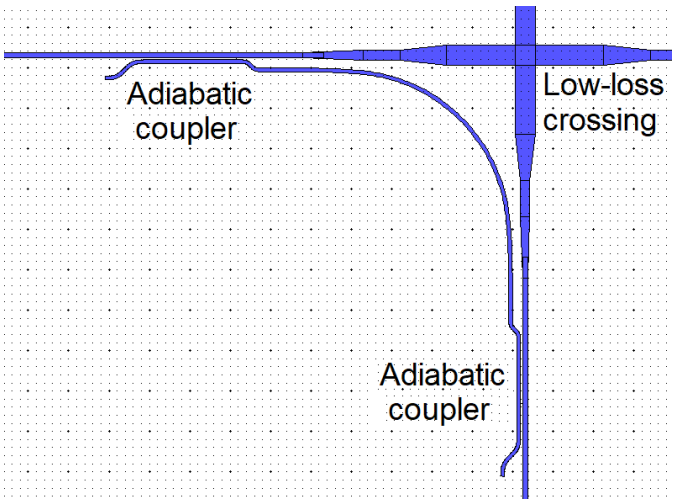

Figure 5.1: Top view of the structure of the proposed optical switch.

As presented in the picture, the component is obtained by including an additional bend waveguide close to the low-loss crossing between the straight optical paths. The PCM is deposited on top of this additional element. The blue color of the features refers to a Si PTE mask, used to pattern the core of the employed rib waveguides. The curvature of each bend portion has been maintained always between 20 and 25 μm. Indeed, it has been proven that, especially for rib waveguides, a smooth curvature is required to avoid a substantial attenuation of the signal [54]. Moreover, in the 90° bend between the horizontal and vertical lines, the transition between the straight and the curved portions is favoured by so-called *spline* bends, in which the curvature gradually varies between 0 and 25 μm. These measures should, in

principle, allow to have negligible losses due to propagation.
While the crossing has been reused from layouts employed in other projects of the group, the rest of the structure has been newly designed, exploiting the results of the simulation process previously performed on the adiabatic coupler. The latter is, indeed, obtained in the portions in which the waveguides approach, creating structures totally analogous to the one presented in Fig. 4.18. This element is the one that determines the ON/OFF state of the switch, depending on, respectively, the amorphous or crystalline state of the PCM, which enables the selective coupling between the waveguides.
The layout procedure consisted in adding to this core portion of the structure all the required optical paths to direct the signal, and electrical contacts for the PCM actuation. The complete unit cell of the switch matrix is shown in Fig. 5.2

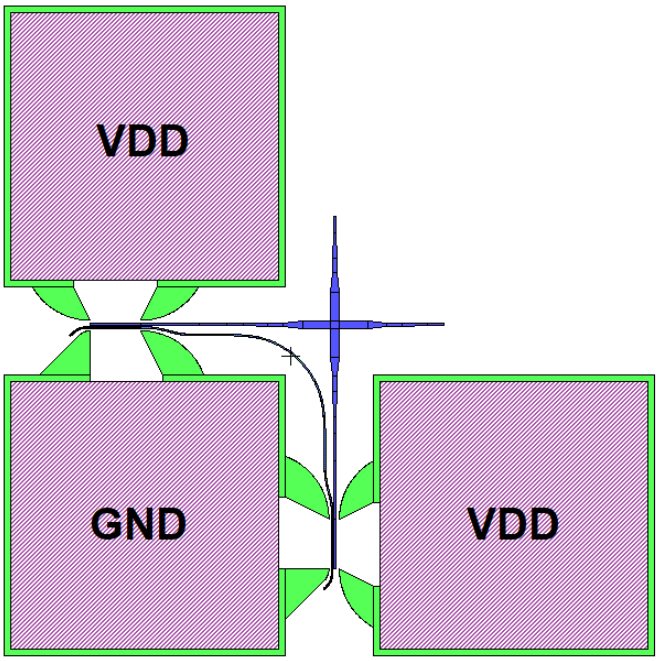

Figure 5.2: Unit cell of the proposed switch matrix.

It can be observed that three metal pads are necessary to cause the state transition for both adiabatic couplers. The central one, maintained at low voltage (GND = ground) is shared between them, while two dedicated pads at high voltage act on only one of them. The reason why their dimensions have been fixed to 100 μm x 100 μm, is that this initial implementation is meant for a characterization process in which the electric signal is provided by external probes, requiring a large area for the contacts. Fully integrated solutions could employ smaller pads.
The green sections refer to the Si FTE mask, employed to completely remove the

silicon portion, Therefore, these portions are used either to isolate the elements, as in the case of the contacts, or to guide the electric signal between the latter, focusing its effect in the region of the couplers.
Starting from this unit cell, the matrix can be obtained by disposing in sequence many of these structures. Two main configurations have been proposed: the first one, shown in Fig. 5.3(a), is simply generated by displacing the cells as they are, while in the second one, presented in Fig. 5.3(b), the metallic contacts are shared between adjacent cells. The main idea at the basis of these configurations is a row-column address mechanism, to enable an efficient actuation of even multiple cells at once.

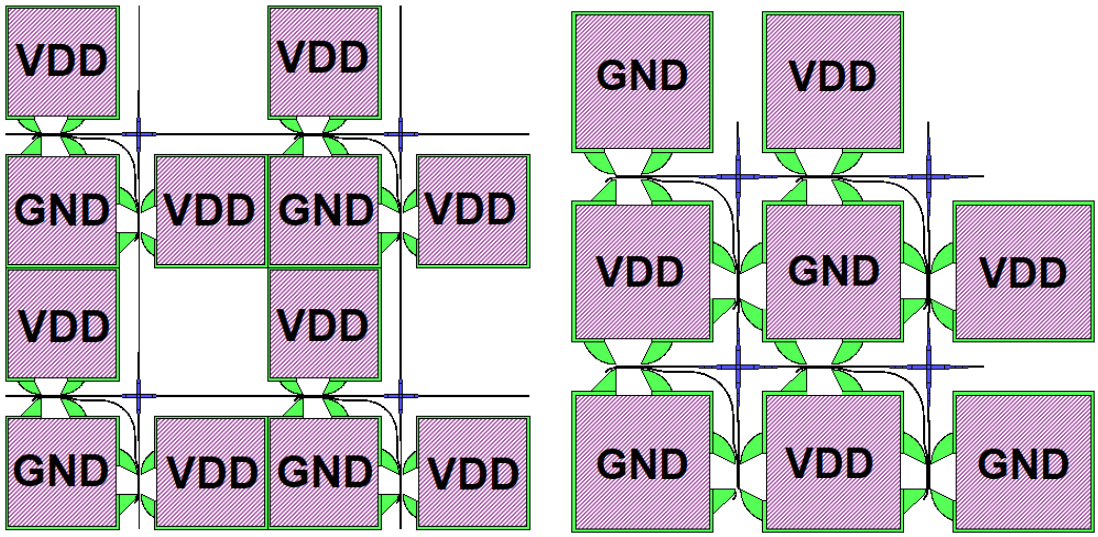

(a) *First implementation* **(b)** *Second implementation*

Figure 5.3: Alternative configurations of 2x2 optical switch matrices.

As seen from the pictures, in the first implementation all the three pads associated to a cell are dedicated to it, while in the second one each pad is can be used to actuate multiple elements of the surrounding components. As a consequence, considering a generic NxN switch matrix, in the first case a total of 3xNxN contacts would be required, while in the second one the amount could be reduced to only NxN, since each of the three pads is shared between three adjacent cells. This last option would obviously reduce the area occupied by the contacts, increasing the scalability of the structure.
The final step to obtain a definitive layout for this kind of component is to add all the optical interconnections between the elements of the the matrix and the inputs/outputs of the circuit. An example of the complete geometry is presented in Fig. 5.4.

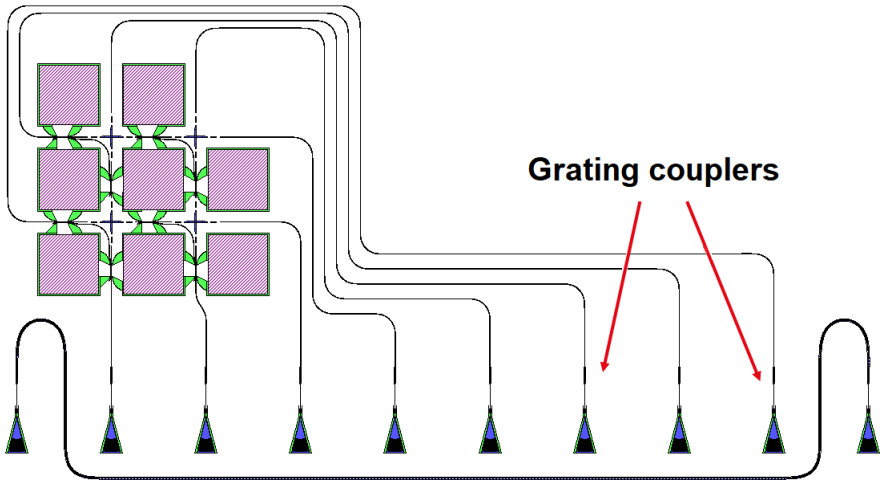

Figure 5.4: Test structure for the 2x2 switch matrix, with shared contacts.

The layout of the optical paths and of the I/O ports, i.e. the grating couplers at the bottom of the structure, have been reused from already implemented designs, and adapted to this particular geometry. Each interconnection is constituted by a Si rib waveguide, and the curvature radius in the bend portions is fixed to 50 μm, for a smooth transition. The optical path directly connecting two grating couplers is added to perform reference measurements, with the aim of estimating the properties of the coupling between the external fibers and the gratings. Indeed, this procedure usually introduces losses, a component that must be isolated from the ones produced by the other components.
An exhaustive analysis on this configuration would have required a performances estimation in terms of both footprint and expected attenuation of the signal. The idea would have consisted in an evaluation of the scalability of the system, and a consequent comparison with currently employed switch matrices found in literature. However, the problems occurred for the conclusive model of the adiabatic coupler, as presented in Sec. 4.3.2, have prevented the extraction of parameters as IL, ER or the bandwidth of the single element, therefore also preventing the extension of these values to larger systems.

5.2 Phase shifter for MZI

The second set of proposed layouts concerns the creation of different MZI (see Sec. 2.2.4), devices in which the signal is divided in two halves by an initial splitter, manipulated in one or both branches, and at the end recombined. The interference pattern generated at the output is then directed towards other portions of the

circuit. In the context of this project, the modulation of the signal happens in terms of a phase delay, obtained exploiting the previously designed phase shifters. The latter, disposed along the branches of the device, act on the signal by changing the propagation constant of the fundamental mode in the hybrid waveguide, depending on the amorphous or crystalline state of the PCM deposited on top.
The main idea to obtain a detailed manipulation of the signal was to add in sequence multiple phase shifters, each one designed to produce a fixed and different phase shift. In order to do so, the optimal geometrical parameters of the single elements has been selected using the procedure detailed in Sec. 4.4. The layout of a single phase shifter, in this case designed for a π shift, is shown in Fig. 5.5.

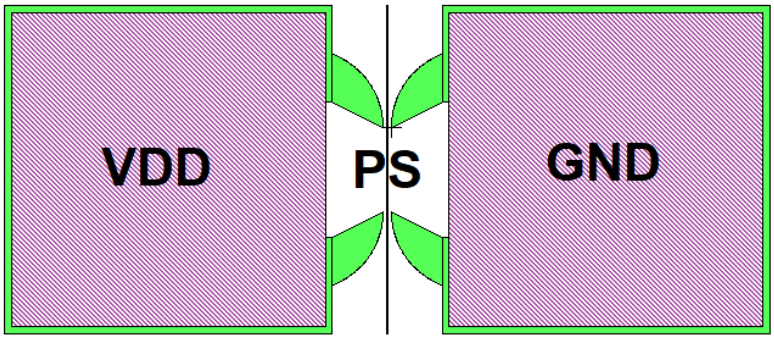

Figure 5.5: Layout of a single phase shifter.

For each element two dedicated metal contacts are required, again with a fixed area of 100 x 100 μm^2, necessary to perform the characterization of the device.
By adding in sequence multiple phase shifters, different implementations of the MZI are possible. In each case, the set of modulating elements must be sufficient to produce in output a complete interference pattern, i.e. to generate selective phase shifts ranging from 0 to 2π. In particular, in this analysis the selected phase delays are of the type $\pi/2^n$, with n going from 0 to 4, meaning that all the combinations between π and $\pi/16$ are possible. However, in principle each phase shift can be designed with the procedure previously discussed.
The first proposed implementation of a MZI is a conventional configuration in which the 2π phase delay is produced on a single branch, while the other remains a simple Si rib waveguide. The layout of the sequence of phase shifters to be disposed on the first branch is presented in Fig. 5.6.

As seen from the picture, an additional phase shift of $\pi/16$ is disposed at the end, so as to reach the overall 2π delay between the two portions of the signal. It can be also noticed that, following the results of the preliminary design procedure, the length of the elements disposed on top of the middle waveguide is reduced together with the generated phase delay.
Actually, the metallic contacts does not have to be placed exactly as illustrated in

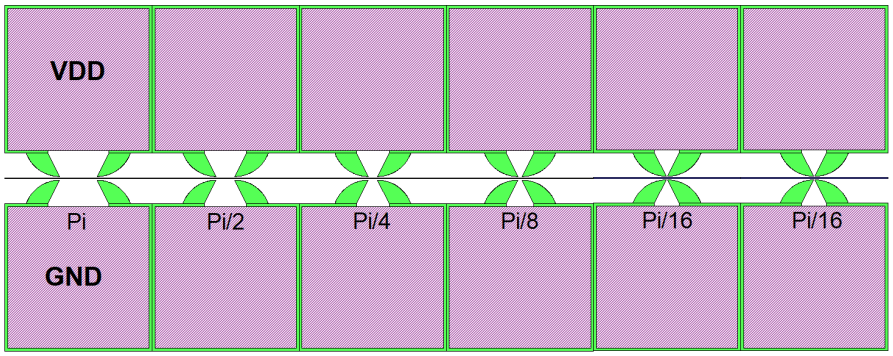

Figure 5.6: Layout of multiple phase shifters, ranging from π to $\pi/16$, to be disposed on a conventional MZI with all elements on a single branch.

the picture. Indeed, a more compact solution could be obtained by displacing the pads in other portions of the layout (for instance in empty regions created by the interconnections) and creating metallic paths from those contacts to the associated phase shifters. Since the metallic lines are narrower than the contacts, the latter could be disposed right one after the other. This consideration can be applied to all the following layouts.
Although this configuration is commonly employed in devices which rely on other modulation mechanisms, the estimated losses in the case of PCMs are too high. Indeed, always according to what discussed earlier, in the worst case, which corresponds to all elements in their lossy crystalline state, the signal attenuation can reach value up to around 11.7, clearly dominant with respect to all other contributions due to propagation.
In consequence, alternative implementations of the MZI have been proposed, starting from a configuration called *push-pull*. In this case, the phase shifters are disposed on both branches, producing in each one a delay up to π, and the overall 2π phase shift is therefore obtained either by delaying one or the other halves of the signal. The principle on which this configuration relies is that what matters to generate the output interference patter is the *relative* phase delays between the components of the signal, with the consequence that it is not necessary to impose the delay only to one of them. The resulting layout for this kind of structure is shown in Fig. 5.7.

It can be observed that, despite the larger area occupied by the additional line of metallic contacts, the structure is shorter in length, since the element to produce a π shift is no more necessary. Even though the latter was the longer element, associated to the highest value of loss, the attenuation of the signal is not reduced with respect to the previous configuration. Indeed, the addition of all the phase shifters on the second branch leads to the same, maximum attenuation of 11.7 dB

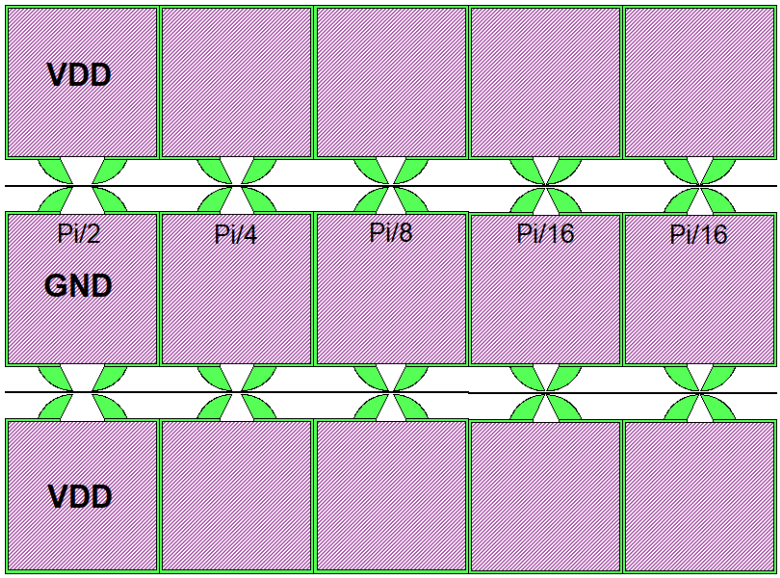

Figure 5.7: Layout of the phase shifters of a push-pull configuration.

for all crystalline elements. However, an important advantage from the fabrication point of view of this configuration is that, since the same phase shifters are disposed on both lines, any potential error in the PCM processing would be compensated, and the same behaviour would be obtained in both of them.
A third configuration to finally reduce the amount of losses introduced in the system is again a push-pull structure, but with an asymmetric optical path to link the phase shifters to the input. In this way, the path followed by the portions of the signal is not the same, with the consequence of an intrinsic passive phase delay between them. Analyzing the expression of the output interference patter, which depends on the intensity of the propagating field, it can be demonstrated that the optimal intrinsic delay is equal to $\pi/2$ [55], therefore, recalling Eq. 4.4 and Eq. 4.7, the required additional length of the optical path of one of the two branches is computed as

$$L = \frac{\Delta\phi}{\beta} = \frac{\pi/2 \cdot \lambda_0}{2\pi \cdot n_{EFF}} = \frac{\lambda_0}{4 \cdot n_{EFF}} = 227nm \tag{5.1}$$

employing the conventional wavelength of 1550 nm and the effective index of the fundamental mode of the Si rib waveguide of 2.71 (see Sec. 4.2.1).
Adopting this configuration, the initial couple of phase shifters for a $\pi/2$ shift is no more required, and therefore only the other four couples related to smaller elements remain. In this way, the losses introduced in the system can effectively be reduced. Indeed, considering again the worst case with all elements in crystalline state, the total attenuation of the signal only arrives at 5.9 dB, almost half than before, and

comparable to the effect due to the input coupling (which is around 5 dB).
Again, the layout procedure was completed by adding all the optical interconnections to link the region of the MZI where the signal is modulated to the I/O ports of the circuit. Fig. 5.8 presents the complete structure in the case of a symmetric push-pull configuration.

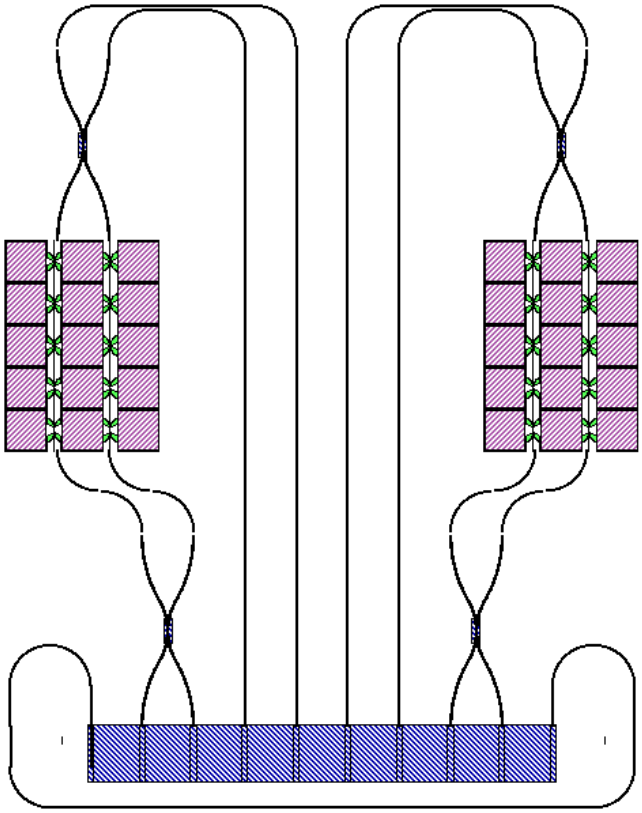

Figure 5.8: Layout of the complete structure of two MZI, push-pull configuration.

It can be observed that this time, the same amount of grating couplers used for the switch matrices can be employed to integrate two different MZI, between which some parametric variations can be applied to test different geometries.
Also for this kind of optical component, a conclusive comparison with other implementations commonly used in PICs would have given an idea of its performances. However, an important missing parameter is the required voltage to be applied to actuate the transition. Again, this analysis has been delayed to a futur continuation of the project.

Chapter 6

Conclusive remarks

This project has analyzed the integration of phase change materials in Silicon Photonic Circuits, with the aim of creating reconfigurable optical components. The non-volatility provided by these semiconductor alloys enables a low-power operation for the system, due to the fact that no actuation is needed to maintain a certain state after it is obtained.
The main purpose of the work here presented was the creation of a fully integrated process flow to pattern the involved PCMs based on, instead of the commonly employed E-beam, DUV lithography, a technique that allows a fast and efficient wafer processing, enabling a large-scale production of optical devices.
The analysis has been performed on two commonly employed PCMs, GeTe and GST, both from the fabrication and from the design and simulation point of view. The first step consisted in the implementation of a fully integrated fabrication process flow, which included both the patterning of the silicon substrate and that of the PCMs, deposited on top. A detailed characterization procedure has then allowed the extraction of both their optical parameters, and of the properties of the thin films produced after their sputtering. In particular, the extraction of the deposition rate of both materials has been followed by a surface analysis of the obtained layers, which confirmed the amorphous-as-deposited character of the sputtered materials, as expected from many previous studies in the field. The deposited films do not present residual stress, and ellipsometric measurements, albeit partial, has confirmed that the PCM optical parameters are comparable with values found in literature.
One of the fundamental results obtained in the context of this project, however, has been provided by the short fabrication loop experiments performed to test the PCM patterning, the most critical step of their integration through DUV lithography. Indeed, successive fabrication tests has proven that this kind of materials can be effectively processed with this technique, even though the resolution remains limited to around 150 nm. Good results have been obtained with both lift-off

and etching, the methods selected to pattern the PCMs. In particular, the former can provide high quality films, without the risk of damaging the silicon structure underneath. However, the process is quite slow, few days are necessary to obtain the final result. On the other hand, etching can process the samples in few minutes, enabling a faster production, but the surface of the obtained features is not as smooth as for lift-off. Anyway, both methods can be employed to pattern elements of few hundreds of nanometers.
In parallel with these procedures, various Si-PCMs hybrid optical components has been designed and simulated. First, the optimization of the geometrical parameters of an adiabatic coupler has been performed in successive steps, starting from the analysis of single waveguides in 2D simulations, and combining these first results to obtain the final 3D structure. The outcome of this procedure is a highly compact geometry, with a total width of few microns, and a length between 10 and 20 μm. Then, similar models have been used to design hybrid phase shifters. Also in this case, the final result is a compact structure, with lengths ranging between few microns and around 15 μm. Despite the highly integrable obtained geometries, the expected losses for these components, introduced in the system by PCMs, are quite high, in the order of even few dB for the largest structures.
The outcome of this procedure has been then employed in the generation of various layouts of complete optical devices. In particular, 2x2 switch matrices have been implemented including multiple designed adiabatic couplers, while the phase shifters have enabled the creation of alternative structures to build a MZI.

To summarize the content of this dissertation, the work performed in the context of this project has proven that PCMs can be integrated in silicon PIC employing DUV lithography for a large scale production. Either lift-off or etching can be used to pattern these materials, to obtain features with dimensions in the order of few hundreds of nanometers. On the other side, the design of various optical reconfigurable components has provided highly integrable geometries in the order of few microns, even though the introduced losses can reach significant values. Finally, multiple layouts for a dedicated lithography mask have been generated.
In conclusion, the completed work constitutes a solid basis for a future continuation of the project, which will start from the outcome of these preliminary tests and layouts to generate and analyze complete optical devices. In particular, after the generation of the required lithography reticle, the complete process flow will be performed on SOI, including also the necessary steps to add the metallic contacts for actuation. A conclusive characterization will allow to estimate the real behaviour of the produced devices, evaluating their scalability for operations in larger optical systems. In case the losses of the system were too high, an efficient alternative would be to try a different approach, using the same procedures employed in this work to either design new geometries [56] or integrating different materials [57].

Appendix A

Guided power in a WG

The power guided in a waveguide, associated to a mode of order n (P_n), can be obtained starting from the Poynting Theorem, which states that, for a waveguide disposed along the z axis

$$P_n = \frac{1}{2} \iint_S (\mathbf{E} \times \mathbf{H}^*)\mathbf{z} dx dy \tag{A.1}$$

where **E** is the electric field and **H** is the magnetic field. By considering a TE mode, and employing Maxwell's equations for the relations between electric and magnetic field, it can be demonstrated that

$$P_n = \frac{\beta}{2\mu_0\omega} \iint_S |E|^2 dx dy \tag{A.2}$$

in which β is the propagation constant of the mode under exam, μ_0 is the vacuum permeability, ω is the frequency and S is the whole surface in which the power is computed. The total power flux is therefore obtained integrating on both x and y between -∞ and +∞.
In conclusion, besides some corrections due to the constants in front of the integral, the power flux transported by a certain mode, in any arbitrary section perpendicular to the waveguide can be computed by integrating along that section the square of the modulus of the electric field.

Appendix B

Losses estimation from the mode's effective index

The losses for perfect waveguides, which present smooth walls, so a null contribution of other sources of field attenuation, can be estimated from the imaginary part of the effective index of the analyzed mode. Since the field propagation of the waveguide can be expressed through the exponential term exp(j β z), with a complex propagation constant ($\beta = \beta_r + j\beta_i$) the latter becomes

$$e^{j\beta z} = e^{j\beta_r z} \cdot e^{-\beta_i z} \tag{B.1}$$

The second term of the product becomes a real, decreasing exponential that, therefore, instead of contributing to propagation, causes a continuous attenuation of the field. For power, which, as shown in Appendix A, is related to the square of the field, the attenuation coefficient (called α) depends on $2 \cdot \beta_i$. Since the propagation constant is linked to the effective index of the mode through Eq. 4.4, the same relation holds for their imaginary part. It can be then concluded that the imaginary part of the effective index is relater to losses in the system.
Usually, the attenuation coefficient is expressed in dB/m using the formula

$$\alpha_{dB} \cdot L = 10 \log_{10}(e^{-2beta_i L}) = -20\beta_i L \cdot \log_{10}(e) \tag{B.2}$$

and, therefore, it can be finally expressed as

$$\alpha_{dB} = -20 \log_{10}(e) \cdot \beta_i = -20 \log_{10}(e) \cdot \frac{2\pi \cdot n_{eff,i}}{\lambda_0} = 54.58 \cdot \frac{n_{eff,i}}{\lambda_0} \tag{B.3}$$

Bibliography

[1] R. Kirchain and L. Kimerling. «A roadmap for nanophotonics». In: *Nature Photonics* 1 (June 2007), pp. 303–305 (cit. on p. 1).

[2] Ralph K. Cavin, Paolo Lugli, and Victor V. Zhirnov. «Science and Engineering Beyond Moore's Law». In: *Proceedings of the IEEE* 100.Special Centennial Issue (2012), pp. 1720–1749. DOI: 10.1109/JPROC.2012.2190155 (cit. on p. 1).

[3] R.H. Havemann and J.A. Hutchby. «High-performance interconnects: an integration overview». In: *Proceedings of the IEEE* 89.5 (2001), pp. 586–601. DOI: 10.1109/5.929646 (cit. on p. 1).

[4] C.-H. Jan et al. «A 45 nm Low Power System-On-Chip Technology with Dual Gate (Logic and I/O) High-k/Metal Gate Strained Silicon Transistors». In: *Proc. Int. Electron Devices Meeting* (2008), pp. 637–640 (cit. on p. 1).

[5] Gary K. Fedder, Roger T. Howe, Tsu-Jae King Liu, and Emmanuel P. Quevy. «Technologies for Cofabricating MEMS and Electronics». In: *Proceedings of the IEEE* 96.2 (2008), pp. 306–322. DOI: 10.1109/JPROC.2007.911064 (cit. on p. 1).

[6] D.A.B. Miller. «Physical Reasons for Optical Interconnection». In: *Int. J. Optoelectron* 11 (1997), pp. 155–168. URL: https://ci.nii.ac.jp/naid/20001632441/en/ (cit. on p. 2).

[7] Zhou Fang and Ce Zhou Zhao. «Recent progress in silicon photonics: a review». In: *International Scholarly Research Notices* 2012 (2012) (cit. on p. 2).

[8] Papichaya Chaisakul et al. «23 GHz Ge/SiGe multiple quantum well electro-absorption modulator». In: *Optics Express* 20.3 (2012), pp. 3219–3224 (cit. on p. 2).

[9] Christian Koos et al. «All-optical high-speed signal processing with silicon–organic hybrid slot waveguides». In: *Nature photonics* 3.4 (2009), pp. 216–219 (cit. on p. 2).

[10] Ming Liu et al. «A graphene-based broadband optical modulator». In: *Nature* 474.7349 (2011), pp. 64–67 (cit. on p. 2).

[11] Kevin J Miller, Richard F Haglund, and Sharon M Weiss. «Optical phase change materials in integrated silicon photonic devices». In: *Optical Materials Express* 8.8 (2018), pp. 2415–2429 (cit. on p. 2).

[12] E Mounier and JL Malinge. «Silicon photonics 2018 report». In: *Yole Développement, Jan* (2018) (cit. on p. 3).

[13] Graham T Reed and CE Jason Png. «Silicon optical modulators». In: *Materials Today* 8.1 (2005), pp. 40–50 (cit. on p. 3).

[14] Matthias Wuttig, Harish Bhaskaran, and Thomas Taubner. «Phase-change materials for non-volatile photonic applications». In: *Nature Photonics* 11.8 (2017), pp. 465–476 (cit. on pp. 3, 19, 20, 34, 57).

[15] Peipeng Xu, Jiajiu Zheng, Jonathan K Doylend, and Arka Majumdar. «Low-loss and broadband nonvolatile phase-change directional coupler switches». In: *ACS Photonics* 6.2 (2019), pp. 553–557 (cit. on pp. 4, 5, 28, 32).

[16] Hanyu Zhang et al. «Miniature multilevel optical memristive switch using phase change material». In: *ACS Photonics* 6.9 (2019), pp. 2205–2212 (cit. on pp. 4, 5, 21, 28).

[17] Pengfei Guo, Andrew M Sarangan, and Imad Agha. «A review of germanium-antimony-telluride phase change materials for non-volatile memories and optical modulators». In: *Applied sciences* 9.3 (2019), p. 530 (cit. on pp. 5, 21–23, 29, 32).

[18] Miquel Rudé et al. «Optical switching at 1.55 μ m in silicon racetrack resonators using phase change materials». In: *Applied Physics Letters* 103.14 (2013), p. 141119 (cit. on pp. 5, 21).

[19] Kentaro Kato, Masashi Kuwahara, Hitoshi Kawashima, Tohru Tsuruoka, and Hiroyuki Tsuda. «Current-driven phase-change optical gate switch using indium–tin-oxide heater». In: *Applied Physics Express* 10.7 (2017), p. 072201 (cit. on pp. 5, 21).

[20] Nikhil Dhingra, Junchao Song, Geetika J Saxena, Enakshi K Sharma, and BMA Rahman. «Design of a compact low-loss phase shifter based on optical phase change material». In: *IEEE Photonics Technology Letters* 31.21 (2019), pp. 1757–1760 (cit. on p. 6).

[21] Ahmad Hariri et al. «Double-port double-throw (DPDT) switch matrix based on phase change material (PCM)». In: *2018 48th European Microwave Conference (EuMC)*. IEEE. 2018, pp. 479–482 (cit. on p. 6).

[22] Winnie N Ye and Yule Xiong. «Review of silicon photonics: history and recent advances». In: *Journal of Modern Optics* 60.16 (2013), pp. 1299–1320 (cit. on p. 8).

[23] *Optical Fiber Attenuation*. URL: https://www.fiberoptics4sale.com/blogs/archive-posts/95052294-optical-fiber-attenuation. (accessed: 04.09.2021) (cit. on p. 9).

[24] Lukas Chrostowski and Michael Hochberg. *Silicon photonics design: from devices to systems*. Cambridge University Press, 2015 (cit. on pp. 9, 11, 12).

[25] Lars Thylén and Lech Wosinski. «Integrated photonics in the 21st century». In: *Photonics Research* 2.2 (2014), pp. 75–81 (cit. on p. 12).

[26] Mengxi Ji et al. «Enhanced parametric frequency conversion in a compact silicon-graphene microring resonator». In: *Optics express* 23.14 (2015), pp. 18679–18685 (cit. on p. 12).

[27] Lukas Chrostowski and Michael Hochberg. *Silicon photonics design: from devices to systems*. Cambridge University Press, 2015 (cit. on pp. 14, 16, 17).

[28] Abu Sahmah Mohd Supa'at. «Design and fabrication of a polymer based directional coupler thermooptic switch». In: *Universiti Teknologi Malaysia: PhD Thesis* (2004) (cit. on p. 15).

[29] Akihiro Takagi, Kaname Jinguji, and Masao Kawachi. «Wavelength characteristics of (2* 2) optical channel-type directional couplers with symmetric or nonsymmetric coupling structures». In: *Journal of lightwave technology* 10.6 (1992), pp. 735–746 (cit. on p. 16).

[30] Yuchan Luo, Yu Yu, Mengyuan Ye, Chunlei Sun, and Xinliang Zhang. «Integrated dual-mode 3 dB power coupler based on tapered directional coupler». In: *Scientific reports* 6.1 (2016), pp. 1–7 (cit. on p. 16).

[31] Po Dong et al. «Low V pp, ultralow-energy, compact, high-speed silicon electro-optic modulator». In: *Optics express* 17.25 (2009), pp. 22484–22490 (cit. on p. 17).

[32] Jifeng Liu et al. «Waveguide-integrated, ultralow-energy GeSi electro-absorption modulators». In: *Nature Photonics* 2.7 (2008), pp. 433–437 (cit. on p. 17).

[33] Volker J Sorger, Norberto D Lanzillotti-Kimura, Ren-Min Ma, and Xiang Zhang. «Ultra-compact silicon nanophotonic modulator with broadband response». In: *Nanophotonics* 1.1 (2012), pp. 17–22 (cit. on p. 17).

[34] Younghyun Kim, Jae-Hoon Han, Daehwan Ahn, and Sanghyeon Kim. «Heterogeneously Integrated Optical Phase Shifters for Next-Generation Modulators and Switches on a Silicon Photonics Platform: A Review». In: *Micromachines* 12.6 (2021), p. 625 (cit. on p. 18).

[35] Tae Joon Seok, Kyungmok Kwon, Johannes Henriksson, Jianheng Luo, and Ming C Wu. «240× 240 wafer-scale silicon photonic switches». In: *Optical Fiber Communication Conference*. Optical Society of America. 2019, Th1E–5 (cit. on p. 19).

[36] Tae Joon Seok, Niels Quack, Sangyoon Han, Richard S Muller, and Ming C Wu. «Large-scale broadband digital silicon photonic switches with vertical adiabatic couplers». In: *Optica* 3.1 (2016), pp. 64–70 (cit. on p. 19).

[37] Keijiro Suzuki et al. «Low-insertion-loss and power-efficient 32× 32 silicon photonics switch with extremely high-Δ silica PLC connector». In: *Journal of Lightwave Technology* 37.1 (2018), pp. 116–122 (cit. on p. 19).

[38] Patrick Dumais et al. «Silicon photonic switch subsystem with 900 monolithically integrated calibration photodiodes and 64-fiber package». In: *Journal of Lightwave Technology* 36.2 (2017), pp. 233–238 (cit. on p. 19).

[39] Matthias Stegmaier, Carlos Rıos, Harish Bhaskaran, C David Wright, and Wolfram HP Pernice. «Nonvolatile all-optical 1× 2 switch for chipscale photonic networks». In: *Advanced Optical Materials* 5.1 (2017), p. 1600346 (cit. on p. 21).

[40] Henning Dieker and Matthias Wuttig. «Influence of deposition parameters on the properties of sputtered Ge2Sb2Te5 films». In: *Thin Solid Films* 478.1-2 (2005), pp. 248–251 (cit. on p. 22).

[41] P Němec et al. «Amorphous and crystallized Ge–Sb–Te thin films deposited by pulsed laser: Local structure using Raman scattering spectroscopy». In: *Materials Chemistry and Physics* 136.2-3 (2012), pp. 935–941 (cit. on p. 22).

[42] T Wagner, J Orava, J Prikryl, T Kohoutek, M Bartos, and M Frumar. «Medium-term thermal stability of amorphous Ge2Sb2Te5 flash-evaporated thin films with regards to change in structure and optical properties». In: *Thin solid films* 517.16 (2009), pp. 4694–4697 (cit. on p. 22).

[43] YA El-Gendy. «Refractive index, oscillator parameters and optical band gap of e-beam evaporated Ga10Ge10Te80 films». In: *Journal of Physics D: Applied Physics* 42.11 (2009), p. 115408 (cit. on p. 22).

[44] Ran-Young Kim, Ho-Gi Kim, and Soon-Gil Yoon. «Structural properties of Ge 2 Sb 2 Te 5 thin films by metal organic chemical vapor deposition for phase change memory applications». In: *Applied Physics Letters* 89.10 (2006), p. 102107 (cit. on p. 22).

[45] Taeyong Eom et al. «Conformal formation of (GeTe2)(1–x)(Sb2Te3) x layers by atomic layer deposition for nanoscale phase change memories». In: *Chemistry of Materials* 24.11 (2012), pp. 2099–2110 (cit. on p. 22).

[46] H. Sattari, A. Toros, T. Graziosi, and N. Quack. «Bistable silicon photonic MEMS switches». In: *MOEMS and Miniaturized Systems XVIII*. Ed. by Wibool Piyawattanametha, Yong-Hwa Park, and Hans Zappe. Vol. 10931. International Society for Optics and Photonics. SPIE, 2019, pp. 97–104. URL: https://doi.org/10.1117/12.2507192 (cit. on p. 27).

[47] Henning Dieker and Matthias Wuttig. «Influence of deposition parameters on the properties of sputtered Ge2Sb2Te5 films». In: *Thin Solid Films* 478.1-2 (2005), pp. 248–251 (cit. on p. 28).

[48] Grégory Abadias et al. «Stress in thin films and coatings: Current status, challenges, and prospects». In: *Journal of Vacuum Science & Technology A: Vacuum, Surfaces, and Films* 36.2 (2018), p. 020801 (cit. on pp. 31, 32).

[49] E Gemo, SV Kesava, C Ruiz De Galarreta, L Trimby, S Garcıa-Cuevas Carrillo, M Riede, A Baldycheva, A Alexeev, and CD Wright. «Simple technique for determining the refractive index of phase-change materials using near-infrared reflectometry». In: *Optical Materials Express* 10.7 (2020), pp. 1675–1686 (cit. on p. 33).

[50] Jasmin Spettel. «Ellipsometry - Phase Change Materials». Unpublished. 2020 (cit. on p. 34).

[51] Zhou Jiao et al. «Inductively coupled plasma etching for phase-change material with superlattice-like structure in phase change memory device». In: *Applied surface science* 280 (2013), pp. 862–867 (cit. on p. 44).

[52] Yangyang Xia et al. «Etching characteristics of phase change material GeTe in inductively coupled BCl3/Ar plasma for phase change memory». In: *Microelectronic Engineering* 161 (2016), pp. 69–73 (cit. on p. 44).

[53] I Comsol. *Wave Optics Module User's Guide version 5.4 a*. 2018 (cit. on p. 52).

[54] Wim Bogaerts and Shankar Kumar Selvaraja. «Compact single-mode silicon hybrid rib/strip waveguide with adiabatic bends». In: *IEEE Photonics Journal* 3.3 (2011), pp. 422–432 (cit. on p. 86).

[55] Giuseppe Pecere. «Spectral Amplitude and Phase Characterization of Optical Devices by RF scan». In: (2010) (cit. on p. 92).

[56] Matthew Delaney, Ioannis Zeimpekis, Daniel Lawson, Dan Hewak, and Otto Muskens. «Sb2S3 and Sb3Se3 as Next Generation Low Loss Phase Change Materials for Photonic Applications». In: *Novel Optical Materials and Applications*. Optical Society of America. 2020, NoTh2C–3 (cit. on p. 95).

[57] Nikhil Dhingra, Junchao Song, Geetika J Saxena, Enakshi K Sharma, and BMA Rahman. «Design of a compact low-loss phase shifter based on optical phase change material». In: *IEEE Photonics Technology Letters* 31.21 (2019), pp. 1757–1760 (cit. on p. 95).